2016

SURFO Technical Report No. 16-01

SURFO

Papers from the

SUMMER UNDERGRADUATE RESEARCH FELLOWSHIP PROGRAM IN OCEANOGRAPHY

at

THE UNIVERSITY OF RHODE ISLAND GRADUATE SCHOOL OF OCEANOGRAPHY

Narragansett, Rhode Island

June – August 2016

This program was supported by The National Science Foundation REU Program (OCE-1460819)

GSO Technical Report No. 16-01

TABLE OF CONTENTS

2016 PROGRAM PARTICIPANTS
SUMMER UNDERGRADUATE RESEARCH FELLOWSHIP IN OCEANOGRAPHY

FELLOWS

Nicole Flecchia, University of Rhode Island (Geology and Geological Oceanography)
Matthew Gentry, University of Massachusetts Amherst (Chemistry and Physics)
Jakob Gessay, Coastal Carolina University (Marine Science)
Scott Goldberg, Northwestern University (Biological Sciences)
Austin Grubb, Susquehanna University (Biology and Spanish)
Annelise Hill, Reed College (Environmental Studies and Chemistry)
Alexandra Norwood, Arizona State University (Geology and Anthropology)
Ariel Pezner, University of California Los Angeles (Environmental Science)
Adena Schonfeld, University of Miami (Marine Science and Biology)
Whitney Schultz, Colorado School of Mines (Geophysical Engineering)
Christopher Vatral, Eastern Nazarene College (Chemistry)
Jennifer Warmack, Humboldt State University (Oceanography)
Elizabeth Wright-Fairbanks, Middlebury College (Biology)

ADVISORS

Amanda Babson
Jeremy Collie
Stephen Licht
Rainer Lohman
Susanne Menden-Deuer
Melissa Omand
Jan Rines
Rebecca Robinson
Lewis Rothstein
Tatiana Rynearson
Theodore Smayda
Matt Wei
Ying Zhang

PROGRAM ASSISTANTS

Stephen Tadros, URI Graduate Student Liaison (Master of Oceanography)
Kim Carey, Program Coordinator

PREFACE

This report presents the papers written by the 13 participants in the ten weeks of the 2016 Summer Undergraduate Research Fellowships in Oceanography (SURFO) program at the Graduate School of Oceanography (GSO), University of Rhode Island (URI). The papers are introduced in alphabetical order of the participants. This 2016 summer represented the 32nd year in which the program has been coordinated and extended through the several disciplines in oceanography and ocean engineering at URI's Narragansett Bay Campus. The activities continue excellence beyond the official duration of the program with presentations anticipated at national and regional conferences: three projects planned for the ASLO 2017 Aquatic Sciences Meeting in Honolulu (HI), one at a regional fisheries meeting, and one at the Northeast Algal Society meeting. One manuscript combining 2015 and 2016 participants will soon be submitted to a peer-reviewed publication. Others will be part of publications in the near future.

The 2016 SURFO participants are grateful to the National Science Foundation REU program for their support through grant OCE-1460819.

The SURFO program sincerely thanks advisors and graduate student mentors at URI who contributed to the program's success including those who gave SURFO seminar presentations and/or participated in various educational activities. In addition, our thanks go to Kim Carey for her timely assistance covering administrative, financial, and recruitment tasks. Finally, we acknowledge Stephen Tadros, a Master in Oceanography student, who served as the program student liaison.

Lucie Maranda October 2016
Kathleen A. Donohue
David C. Smith
SURFO Site Directors

Surface Circulation on the New England Coastal Shelf

Nicole M. Flecchia and Lewis M. Rothstein
Graduate School of Oceanography, University of Rhode Island, Narragansett, RI 02882
Corresponding author: nicole_flecchia@my.uri.edu

Abstract
The waters of Rhode Island Sound (RIS) become anomalously warm and saline after a Gulf Stream warm core ring appears on the shelf break just offshore of RIS. Parcels of water from the warm core ring mix with coastal shelf water through cross-isobath exchange, as indicated by observed net onshore exchanges of salt and nitrate, before transporting those water properties into the RIS. In order to understand the dynamical impact of this anomalous water intrusion one must first establish the climatological seasonal cycle of coastal shelf circulation. This provides the background variability against which the anomaly imposes its dynamics. This study focuses only on surface wind forcing as the main driving force of the coastal circulation, although the model we have selected to represent these physics includes buoyancy (heat and freshwater), tidal and river forcings as well. Surface wind velocity is strongest in the winter and weakest in the spring, whereas surface circulation is strongest in the fall and weakest in the spring. The annual mean surface wind velocity is 5 m/s in the east-southeast direction and the annual mean surface circulation has a maximum velocity of 0.25 m/s. Directionality of the surface winds and circulation indicate the southern New England coastal shelf circulation is in both Ekman balance and geostrophic balance.

Anomalous Gulf Stream intrusions on the southern New England coastal shelf appear in the form of meanders and warm core rings. These anomalous intrusions are usually surface-intensified but can be identified in the region of the pycnocline in the summer, when there is high stratification, and near-bottom in the fall and spring due to a decrease in stratification [*Churchill et al*., 2003; *Ullman et al*., 2014]. Surface-intensified and pycnocline intrusions extend shoreward onto the shelf along the seasonal pycnocline and stay within the top 40 m of the water column [*Churchill et al*., 2003]. Near-bottom intrusions encompass most of the water column and have a downward increasing salinity [*Churchill et al*., 2003]. There is strong evidence of the onshore movement of slope water due to interaction of the intrusions with the shelf break front, which allows for cross-isobath exchange indicated by the net onshore transfer of salt and nutrients [*Ullman et al*., 2014]. Based on these and similar observations, we believe that the circulation of the southern New England coastal shelf is altered by the presence of anomalous Gulf Stream intrusions. Before this can be modeled, the seasonal circulation of the southern New England coastal shelf first needs to be established and analyzed.

The coastal shelf of southern New England consists of Georges Bank (GB) and the Middle Atlantic Bight (MAB), which includes Rhode Island Sound (RIS), Block Island Sound and the New York Bight (Figure 1). Water in this region originates in the polar region of the Scotian Shelf and then moves through the Gulf of Maine before reaching Georges Bank and the MAB [*Luo et al*., 2013]. This makes the water on the coastal shelf off of southern New England colder and fresher near the coast, and warmer and more saline near the open ocean [*Luo et al*., 2013]. The GB consists of anticyclonic circulation that has seasonal variations governed by tidal

forcings and seasonal heat flux cycles [*Naimie et al*., 2013]. The MAB consists of near-surface flow that is onshore and near-bottom flow that is offshore; the change in directionality occurs around the 50-m isobath [*Lentz*, 2008]. However, there is an overall mean-depth averaged flow that is alongshelf, toward the equator, and increases linearly with water depth [*Lentz*, 2008]. Circulation in RIS, Block Island Sound and the New York Bight follows the same general alongshelf and equatorward pattern as the MAB circulation [*Blumberg and Galperin*, 1990; *Luo et al*., 2013; *Sun et al*., 2016]. However, different regions of the MAB have different local circulation patterns. The RIS has cyclonic circulation that is locally wind-driven and is also remotely affected by the North Atlantic Oscillation [*Luo et al*., 2013]. There is an anticyclonic eddy-like current off Montauk Point in Block Island Sound [*Sun et al*., 2016]. The New York Bight is greatly affected by wind stress to the point where strong winds can reverse the direction of flow [*Blumberg and Galperin*, 1990].

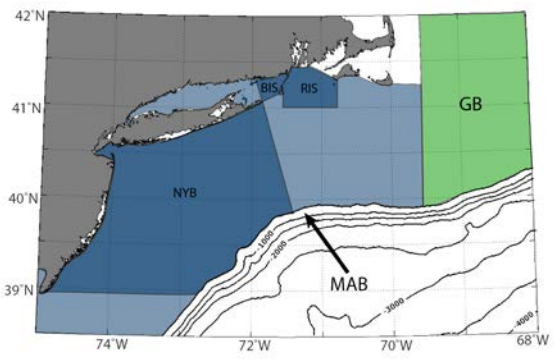

Figure 1. Southern New England coastal shelf with bathymetry contours (m): Georges Bank (GB), Middle Atlantic Bight (MAB), Rhode Island Sound (RIS), Block Island Sound (BIS), and New York Bight (NYB).

In this paper, we present model results for the mean and seasonal circulation of the southern New England coastal shelf. We first review the model used for this experiment in section 2. We then discuss the methods for interpreting the forcing datasets and model results in section 3. In section 4 we compare the model to known observations of the MAB and the RIS circulation. Section 5a is a review of the seasonal variability of circulation along the coastal shelf of southern New England, section 5b is a review of the annual mean circulation in this region, and section 6 is a discussion of these results.

Design of Numerical Experiment

The data used in this experiment were previously published by *Zhang et al.* [2016]. The numerical model is the Regional Ocean Modeling System (ROMS). This is a free-surface, hydrostatic, terrain-following, primitive equations ocean model comprised of algorithms and nonlinear kernels [*Shchepetkin and McWilliams*, 2005]. The model domain extends from the Scotian Shelf to Cape Hatteras to cover GB and the MAB. This region is configured to resolve the Gulf Stream [*Zhang et al*., 2016]. The model uses topography derived from the 1 arc-minute ETOPO1 Global Relief Model of the Earth's surface, bathymetry that ranges from 10 to 5000 m within the model range and a water column with 30 terrain-following levels that have the highest resolution at the surface and lowest resolution at depth [*Zhang et al*., 2016]. The open boundary forcing is provided by the Hybrid Coordinate Ocean Model with the Navy Coupled Ocean Data Assimilation scheme (HYCOM/NCODA, http://hycom.org/dataserver/glb-analysis). Free surface and depth-averaged values are given using the method from *Flather* [1976], external subtidal values taken from HYCOM/NCODA and tidal components M_2, N_2, S_2, O_1, and K_1 [*Zhang et al*., 2016]. Local surface forcing is denoted from the National Oceanic and Atmospheric Administration (NOAA) National Centers for Environmental Prediction North America Regional Reanalysis (NCEP/NARR), and the United

States Geological Survey (USGS, http://www.usgs.gov/water/) stream gauge climatological datasets were used as a basis for fresh water outflow [*Zhang et al*., 2016].

For the purposes of this experiment, only two years of climatological data are being utilized from the larger 12-year forcing dataset used by *Zhang et al.* [2016], and the method for this will be discussed in section 3. The climatological data consist of surface momentum flux, heat fluxes, tides and river mass flux. For the purposes of this study, only surface momentum flux, which consists of surface winds in the zonal and meridional directions, will be analyzed in terms of the resulting circulation. This is because changes in wind strength have been known to affect the direction of flow in RIS as well as other regions within MAB [*Luo et al*., 2013; *Blumberg and Galperin*, 1990]. The output data have also been provided by *Zhang et al.* [2016], and include the model outputs of circulation based on surface momentum flux. All data will be presented in the context of the region of study, the coastal shelf of southern New England.

Data Analysis

The original forcings dataset consisted of 12-year files: 2 years of climatological data and ten years of time series data from January 2004 to December 2013 [*Zhang et al*., 2016]. The climatological data were obtained from the 12-year files and used to create new 2-year files. From these files seasonal and annual means of surface wind velocity in the zonal and meridional directions were generated. Vector plots for each season, represented by February (winter), May (spring), August (summer) and November (fall), as well as the annual mean were generated to illustrate wind velocity on the southern New England coastal shelf. The equation

$$U_{(u_n,v_n)} = \sqrt{u_n^{\,2} + v_n^{\,2}} \qquad (1)$$

is used to calculate the magnitude of each vector, where U is the average magnitude of zonal and meridional wind at point (u_n, v_n), u is the zonal wind component and v is the meridional wind component. The equation

$$V_{(u_n,v_n)} = \tan^{-1}\left(\frac{v_n}{u_n}\right) \qquad (2)$$

is used to calculate the direction of each vector, where V is the average direction of zonal and meridional wind at point (u_n, v_n) on a unit circle (in degrees), u is the zonal wind component and v is the meridional wind component.

The circulation, in relation to the zonal and meridional winds, was remapped to the model's grid. The data were then plotted as a pseudocolor checkerboard plot with flat shading on a Universal Transverse Mercator projection with a Global Self-consistent, Hierarchal, High-resolution Geography Database coastline, which illustrates the velocity of the circulation. Equations (1) and (2) were then used to calculate the magnitude and direction of flow for the circulation, respectively. The results were superimposed over the pseudocolor checkerboard plot in the form of vectors. This process was done to illustrate seasonal mean circulation, with seasons represented by the same months as the seasonal means of wind velocity, as well as the annual mean circulation.

Model Evaluation

We compare the model results to known observations of the MAB circulation to evaluate the model and prove that it can accurately portray the essential features of the MAB coastal shelf circulation. The model outer shelf circulation is compared to *Lentz* [2008] in which mean-depth averaged currents along the MAB were studied (Figure 2). The model results are obtained by averaging the surface circulation of the model results for one year. The circulation of the model results is consistent with the observations. Both illustrate the circulation as alongshelf in the direction of the equator. There are differences in velocity when comparing the model and the

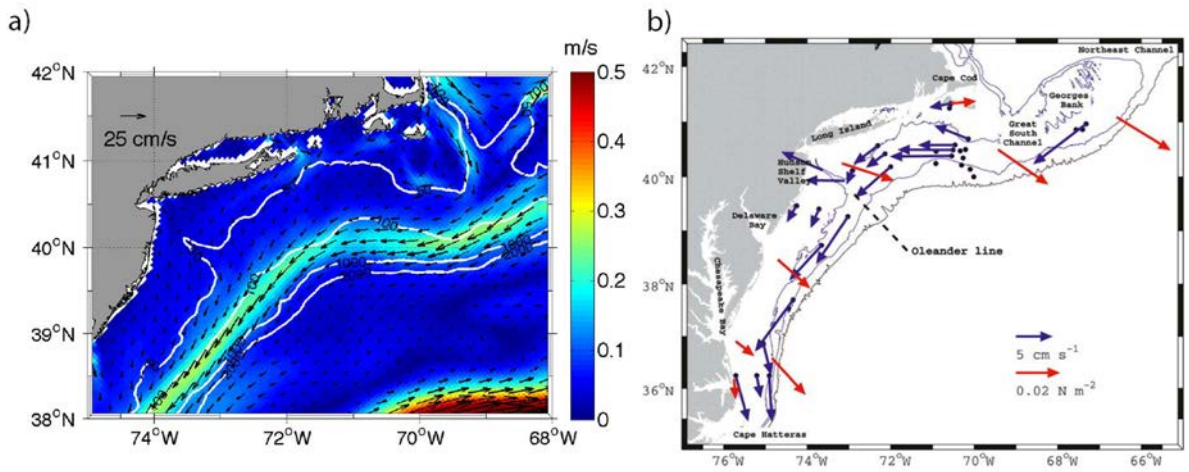

Figure 2. Comparison of southern New England coastal shelf circulation between (a) model and (b) observations form *Lentz* [2008].

observations; however the model adequately represents outer MAB shelf circulation for our future purposes, i.e. to study the anomalous impact of Gulf Stream intrusions.

The model results of the inner shelf region of RIS are compared to observations of the residual circulation in RIS from *Kincaid et al.* [2003] (not shown here). When averaging the summer and winter values of volume of water transported (m^3/s), the annual mean direction of volume transport becomes east to west along the mouth of Narragansett Bay and then northeast to southwest along the Rhode Island coast out of RIS. The model annual mean RIS circulation is consistent with these observations. There are discrepancies between the model and observations with regard to the direction of circulation as well as the magnitude of flow. Still, the overall circulation patterns of the model are sufficient to represent RIS circulation.

Results

Seasonal Mean Wind Velocity and Circulation

Seasonal means of surface wind velocity are illustrated using vectors that represent magnitude and direction (Figure 3). Winds in the winter have the strongest velocity of ~7 m/s in the southeast direction. Spring winds are the weakest and have velocities of ~4 m/s, whereas summer winds have a velocity of 4.5 m/s; both in the northeast direction. Winds in the fall have a velocity of about 4.3 m/s in the southeast direction. The seasonal mean circulation is illustrated using PCOLOR to represent velocity of flow and vectors to represent the direction of flow (Figure 4). Circulation is strong in the winter, reaching a maximum velocity along the shelf break of 0.35 m/s. Weak circulation occurs in the spring and summer, with maximum alongshelf velocities of 0.25 m/s and 0.28 m/s, respectively. The strongest circulation is in the fall reaching a maximum velocity of 0.4 m/s on the shelf break.

Annual Mean Wind Velocity and Circulation

Annual mean winds are in the southeast direction with a maximum speed of ~4.5 m/s (Figure 5). The value of annual mean winds is consistent with averaging the values of the seasonal averages of wind velocity, with a 7.6% difference between the two. The annual mean circulation is in the southeast direction along the coast and shelf break (Figure 6). Circulation on the coastal shelf and on the continental rise to the south of the shelf break is weak, having an average velocity of 0.1 m/s. The velocity on the shelf break itself is stronger, reaching a maximum velocity of 0.25 m/s.

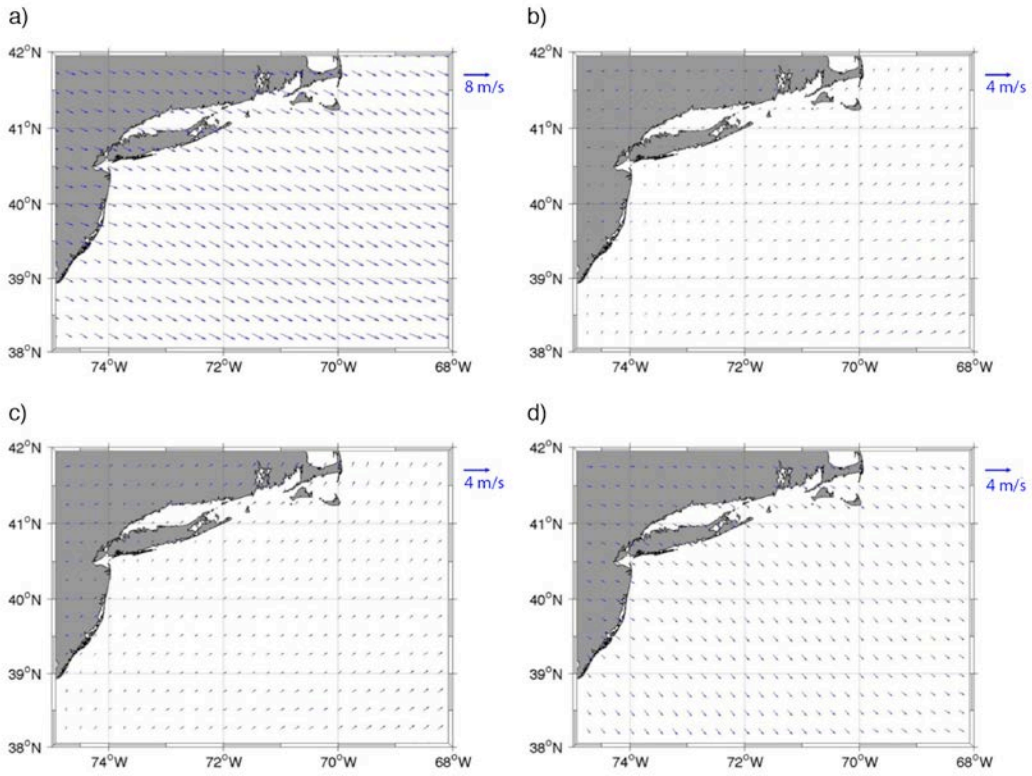

Figure 3. Seasonal mean surface wind velocity (m/s) for winter/February (a), spring/May (b), summer/August (c) and fall/November (d).

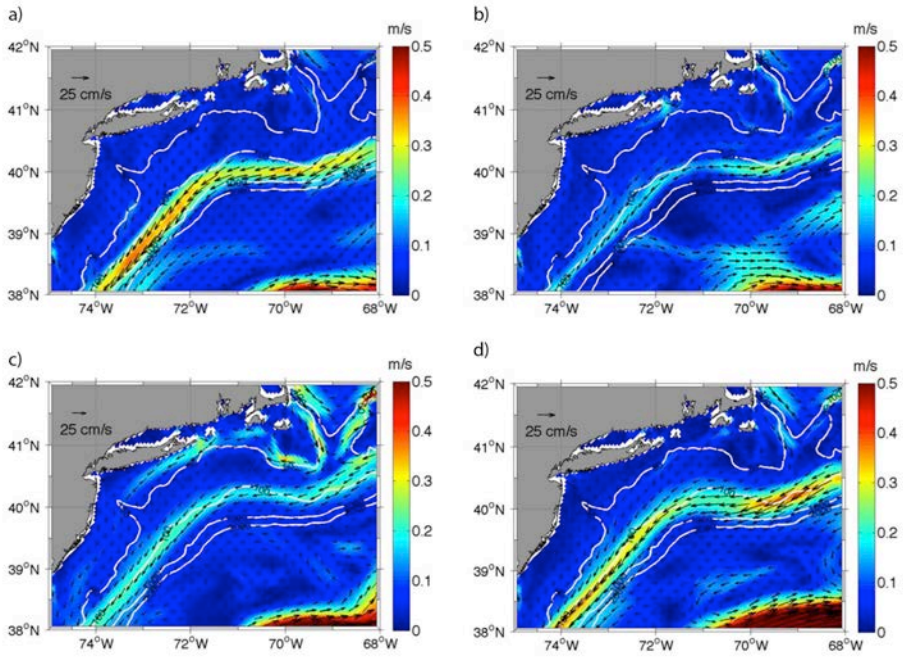

Figure 4. Seasonal mean circulation (m/s) for winter/February (a), spring/May (b), summer/August (c) and fall/November (d).

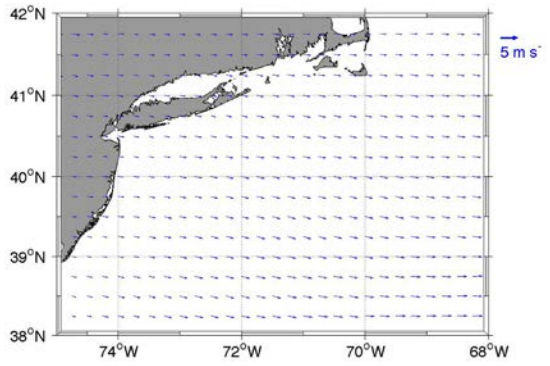

Figure 5. Annual mean surface wind velocity (m/s).

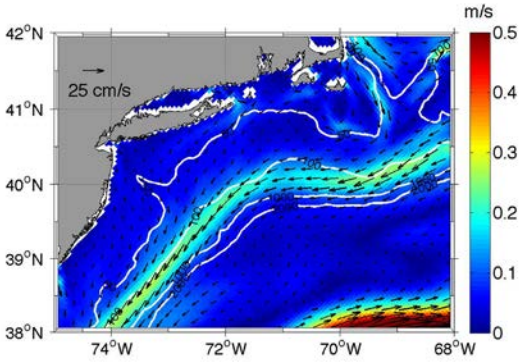

Figure 6. Annual mean circulation (m/s).

Discussion

The seasonal mean wind velocities and seasonal averages of circulation show some relationship, but it is not obvious when comparing Figures 3 and 4. While the strongest surface wind velocity occurs in the winter, the strongest circulation occurs in the fall; the weakest surface wind velocity is in the spring while the weakest circulation is in the spring. Based on these observations, a definitive correlation cannot be made between surface wind velocity and circulation.

While the annual mean wind direction is east-southeast, the annual mean circulation is flowing south-southwest as seen in Figures 5 and 6. Based on the directionality of both the winds and circulation, this system appears to be in Ekman balance. As stated in *Ekman* [1905], surface currents typically deviate 45˚ to the right of the wind direction in the northern hemisphere due to the Coriolis force and friction from surface winds being in equilibrium. However, when circulation is occurring close to a continent it causes the current to flow parallel to the coast as seen on the southern New England coastal shelf [*Ekman*, 1905]. The proximity of the current to the coast causes the current to flow along the coast with a velocity dependent on the wind velocity [*Ekman*, 1905]. As a result, while the direction of flow primarily corresponds to the annual mean wind direction, seasonal variations in circulation that coincide with the seasonal variations in wind velocity and direction will also occur as seen in Figures 3 and 4 [*Ekman*, 1905].

However, Ekman balance cannot be the sole balance of the alongshelf circulation in this region because when the wind strength decreases the alongshlef circulation gets stronger. We believe that there must be a geostrophic balance in play for the alongshelf flow in the MAB. This balance is defined as the Coriolis force and meridional pressure gradient being in equilibrium. The Coriolis force is present due to the Earth's rotation, causing moving objects in the northern hemisphere to move to the right as one looks in the direction of that movement [*Persson*, 1998]. The pressure gradient along the MAB, which has to be positive in order for alongshelf circulation to occur, is set up by zonal winds, the Gulf Stream, fresh water input from rivers and the Coastal Labrador Sea Water (CLSW) transport [*Xu and Oey*, 2011]. Zonal winds create a negative pressure gradient, and consequently have minimal influence on the MAB alongshelf pressure gradient [*Xu and Oey*, 2011]. The Gulf Stream creates a positive pressure gradient, but its distance from the coastal shelf causes it to only have an effect on the seasonal variability of the alongshelf pressure gradient due to its latitudinal shifts and anomalous intrusions on the shelf break [*Xu and Oey*, 2011]. Fresh water input from rivers and the CLSW

transport both create strong positive pressure gradients and therefore have strong influences on the alongshelf pressure gradient of the MAB [*Xu and Oey*, 2011].

Even though fresh water input and CLSW transport have the strongest influence on the MAB alongshelf pressure gradient, all four components must be present to create the pressure gradient on the MAB. In the equation modified from *Xu and Oey* [2011]

$$ASP \times 10^8 = RIV + (7 \times CSLW + 1.3) \times H_v(CSLW - CSLW_{critical}) - WINDS - GS \quad (3)$$

the relationship between all four components is illustrated, where *ASPG* is the alongshelf pressure gradient, *RIV* is fresh water river input, *CLSW* is the nondimensional CLSW transport, H_v is the Heaviside function, $CLSW_{critical}$ is the nondimensional critical CLSW transport, *WINDS* is the zonal winds and *GS* is the Gulf Stream. Without the four components working together in this manner, the alongshelf pressure gradient generating the alongshelf flow would not exist, and the system would not be in geostrophic balance.

Conclusions

This study documented the seasonal and annual mean winds and circulation of the southern New England coastal shelf. Research of this region will continue through the study of how anomalous intrusions of the Gulf Stream impact the circulation of the southern New England coastal shelf in the region of the intrusion and regions removed from the intrusion.

Acknowledgments. Shuwen Zhang (Rutgers University) kindly shared her model and data with us. Dr. Qianian Liu (University of Maine) helped with the installation and set of ROMS. This research was funded by the Rhode Island Science and Technology Advisory Council through grant #0004835.

References

Blumberg, A. F., & Galperin, B. (1990). On the Summer Circulation in New York Bight and Contiguous Estuarine Waters. In R. T. Cheng (Ed.), *Residual Currents and Long-term Transport* (pp. 451–468). Springer New York. Retrieved from http://link.springer.com/chapter/10.1007/978-1-4613-9061-9_31

Churchill, J. H., Manning, J. P., & Beardsley, R. C. (2003). Slope water intrusions onto Georges Bank. *J. Geophys. Res*, *108*, 8012.

Ekman, V. W. (1905). On the Influence of Earth's Rotation on Ocean-Currents. Archive of Mathematics, Astronomy and Physics, 11, 1-52.

Ferrari, R., & Plumb, R. A. (2003). Residual circulation in the ocean. Citeseer. http://citeseerx.ist.psu.edu/viewdoc/download?doi=10.1.1.518.57&rep=rep1&type=pdf

Flather, R. A. (1976). Results from a storm surge prediction model of the north-west European continental shelf for April, November and December, 1973 [Monograph]. Retrieved July 27, 2016, from http://eprints.soton.ac.uk/14307/

Kincaid, C., Pockalny, R. A., & Huzzey, L. M. (2003). Spatial and temporal variability in flow at the mouth of Narragansett Bay. *Journal of Geophysical Research: Oceans*, *108*(C7), 3218. http://doi.org/10.1029/2002JC001395

Lentz, S. J. (2008). Observations and a Model of the Mean Circulation over the Middle Atlantic Bight Continental Shelf. *Journal of Physical Oceanography*, *38*(6), 1203–1221. http://doi.org/10.1175/2007JPO3768.1

Luo, Y., Rothstein, L., Liu, Q., & Zhang, S. (2013). Climatic variability of the circulation in the Rhode Island Sound: A modeling study. *Journal of Geophysical Research: Oceans*, *118*(9), 4072–4091. http://doi.org/10.1002/jgrc.20285

Naimie, C. E., Limeburner, R., Hannah, C. G., & Beardsley, R. C. (2001). On the geographic and seasonal patterns of the

near-surface circulation on Georges Bank — from real and simulated drifters. *Deep Sea Research Part II: Topical Studies in Oceanography*, *48*(1–3), 501–518. http://doi.org/10.1016/S0967-0645(00)00087-4

Persson, A. (1998). How do we understand the Coriolis force? *Bulletin of the American Meteorological Society*, *79*(7), 1373–1385.

Shchepetkin, A. F., & McWilliams, J. C. (2005). The regional oceanic modeling system (ROMS): a split-explicit, free-surface, topography-following-coordinate oceanic model. *Ocean Modelling*, *9*(4), 347–404. http://doi.org/10.1016/j.ocemod.2004.08.002

Sun, Y., Chen, C., Beardsley, R. C., Ullman, D., Butman, B., & Lin, H. (2016). Surface circulation in Block Island Sound and adjacent coastal and shelf regions: A FVCOM-CODAR comparison. *Progress in Oceanography*, *143*, 26–45. http://doi.org/10.1016/j.pocean.2016.02.005

Ullman, D. S., Codiga, D. L., Pfeiffer-Herbert, A., & Kincaid, C. R. (2014). An anomalous near-bottom cross-shelf intrusion of slope water on the southern New England continental shelf. *J. Geophys. Res. Oceans*, *119*, 2.

Xu, F.-H., & Oey, L.-Y. (2011). The Origin of Along-Shelf Pressure Gradient in the Middle Atlantic Bight. *Journal of Physical Oceanography*, *41*(9), 1720–1740. http://doi.org/10.1175/2011JPO4589.1

Zhang, S., Luo, Y., Rothstein, L. M., & Gao, K. (2016). A numerical investigation of the interannual-to-interpentadal variability of the along-shelf transport in the Middle Atlantic Bight. *Continental Shelf Research*, *122*, 14–28. http://doi.org/10.1016/j.csr.2016.03.022

Key Points:

- Zonal winds drive Middle Atlantic Bight (MAB) alongshelf circulation, adjusting on-shelf pressure gradients.
- Buoyancy fluxes, mainly due to salinity, also contributes to both alongshore and on-shelf pressure gradients.
- The MAB is in both Ekman and Geostrophic balance.

Key Index Words:
Coastal shelf circulation; Seasonal variability; ROMS

Integration of Gene Expression Data in Genome-Scale Metabolic Modeling

Matthew R. Gentry[1,2], Julie Cuddigan[3], Keith Dufault-Thompson[3] and Ying Zhang[3]
[1]Graduate School of Oceanography, University of Rhode Island, Narragansett, RI 02882
[2] Departments of Physics and Chemistry, University of Massachusetts Amherst, MA, 01003
[3]College of the Environment and Life Sciences, University of Rhode Island, Kingston, RI 02881
Corresponding author: mgentry@umass.edu

Abstract
Metabolic models are networks of interconnected biochemical reactions designed to simulate the growth of an organism. Traditional simulations account only for reaction stoichiometry, and do not provide a way of accounting for the influence of gene regulations under various environmental factors such as changing oxygen concentrations. We have implemented two methods in Python™ for integrating gene expression data into simulations that will allow them to better represent the metabolism under given conditions. The first method uses the statistical significance of changes in gene expression between conditions to mark reactions as either 'on' or 'off'. The second method continuously scales the maximum flux allowed through reactions in the model based on expression levels. A comparison of these methods to standard modeling procedures, done using a model of *Shewanella piezotolerans* WP3, shows increased precision in characterizing the metabolism of this deep-sea bacterium. This is exemplified in a reduction in the variability of reactions. The continuous method shows more reduction in variability than the 'on/off' method. The 'on/off' method shows more changes to specific metabolic pathways such as gluconeogenesis, the production of acetyl coenzyme A, and the citric acid cycle. These two methods for including gene expression data help us understand the adaptations of WP3 to the deep ocean by allowing us to simulate bacterial activity under the variable oxygen conditions found at depth.

This manuscript intentionally left blank

This manuscript intentionally left blank

This manuscript intentionally left blank

This manuscript intentionally left blank

This manuscript intentionally left blank

This manuscript intentionally left blank

This manuscript intentionally left blank

This manuscript intentionally left blank

This manuscript intentionally left blank

This manuscript intentionally left blank

This manuscript intentionally left blank

This manuscript intentionally left blank

Estimating biomass and analyzing bloom seasonality of the diatoms, *Skeletonema costatum* (s.l.), *Detonula confervacea*, and *Thalassiosira nordenskioeldii* in Narragansett Bay

Jakob S. Gessay[1,2] and Theodore J. Smayda[1]
[1]Graduate School of Oceanography, University of Rhode Island, Narragansett, RI 02882
[2]Department of Marine Science, Coastal Carolina University, Conway, SC 29528
Corresponding author: jsgessay@coastal.edu

Abstract
To better understand biomass and bloom seasonality in Narragansett Bay, we compiled and analyzed extant data sets for the commonly found diatom species, *Skeletonema costatum* (s.l.) and its competing winter-spring bloom species, *Detonula confervacea* and *Thalassiosira nordenskioeldii*. Using cell volume as a biomass measure for *S. costatum* (s.l.), the strongest correlation was with cellular carbon; no correlation was found with nitrogen or chlorophyll. It has been suggested that temperature plays a critical role in dictating cell volume of diatoms, which influences biomass; however, the data show no indication of a strong temperature influence. Bloom seasonality was analyzed on a pentade timescale for winter-spring and summer-fall blooms. For both blooms, *S. costatum* (s.l.) has historically been the dominant species numerically. Cell concentrations were converted to carbon concentrations yielding results indicating that *S. costatum* (s.l.), despite its large cell concentration, does not always produce the highest carbon concentrations. *T. nordenskioeldii* frequently surpassed *S. costatum* (s.l.) in carbon concentrations. *S. costatum* (s.l.) and *T. nordenskioeldii* both exhibit long-term trends of extensive growth followed by periods of decreased abundance, making it difficult to clearly define trends. *D. confervacea* gradually decreased in cell concentration and carbon concentration. The data show that bloom seasonality may be shifting from a predominant winter-spring to a summer-fall bloom on a pentade timescale in Narragansett Bay.

Cellular carbon estimates.

Carbon is an essential element for the functionality of every living organism, and therefore of utmost importance to understand how it moves through a biological system from its original assimilation to its release. Being able to quantify how much carbon biomass is available in primary producers to be consumed by grazers has serious implications for the overall understanding of the carrying capacity of the system. Phytoplankton obtain carbon from the water in the form of carbon dioxide and turn it into organic carbon through photosynthesis. Large-scale measuring of the organic cellular carbon for each species of phytoplankton is an impossible task, which is why researchers must estimate cellular carbon from a given parameter, cell volume.

Previous work suggests that the best way to estimate cellular carbon in phytoplankton is by correlating it with a more easily measured parameter: cell volume. However, morphological differences between types of phytoplankton can contribute to error when estimating carbon content. A diatom has a fundamentally different shape from that of a dinoflagellate, and the amount of carbon needed for a diatom to function may be more or less than a dinoflagellate. This discrepancy

is precisely what researchers found when developing equations to estimate carbon content for all types of phytoplankton in general (Strathman 1967), and the carbon content specifically in diatoms (Strathman 1967, Montagnes and Franklin 2001, Menden-Deuer and Lessard 2000). A key finding of Strathman (1967) was that for a given cell volume, diatoms would always have a lesser cellular carbon content than other phytoplankton.

Although the trend between cell volume and cellular carbon for all diatoms is strong in many cases, there are reasons to question whether or not certain species of diatom do not follow the trend as well as others. Just as estimates of carbon for all diatoms diverged from the estimates for all phytoplankton, could it be that key species of diatoms do not fit the prescribed relationship for all diatoms? Diatoms are a diverse group of phytoplankton with a large size distribution amongst species, their size distribution has a range of nine orders of magnitude (Litchman et al. 2008); this could affect the relative amount of carbon needed for a cell of a particular species to function.

Skeletonema costatum (s.l.) is one of the most abundant species in Narragansett Bay, Rhode Island, accounting for 60 percent of all diatom species in the bay (Smayda, pers. comm). Due to its great abundance, it is important to fully and accurately understand how *S. costatum* (s.l.) contributes to the overall biomass of the bay with respect to carbon. For this reason, the first aim of this study was to determine if the cell carbon-cell volume trend in *S. costatum* (s.l.) diverged from the trend in all diatoms, and if so, what mathematical relationship can define that trend.

Analysis of bloom seasonality.

In mid-temperate latitudes, phytoplankton blooms, depending on the time of the year experience limited growth due to lack of light or nutrients, or physical conditions such as changing temperatures. This creates a seasonality of the blooms in a given area, which can be comprised of specific species of phytoplankton. The seasonality of the blooms creates somewhat consistently expected conditions from one year to the next. Bloom seasonality, and the phytoplankton community structure of that bloom can affect the available biomass in a given system, especially if that system is changing.

The winter-spring (December of previous year - April) bloom in Narragansett Bay has historically contained three key species of diatoms, *Skeletonema costatum* (s.l.), *Detonula confervacea*, and *Thalassiosira nordenskioeldii* (Smayda 1973). Whereas *S. costatum* (s.l.) is a eurythermal species, tolerating both warm and cold waters allowing it to bloom throughout the year, *D. confervacea* and *T. nordenskioeldii* are strictly cold water species (Durbin 1978) and are the main constituents of the winter-spring bloom in Narragansett Bay but begin to disappear as the water becomes warmer.

As global climate begins to warm, thermal boundaries are being pushed increasingly northwards. Species have begun to migrate farther north in pursuit of conditions favorable to their physiological function (Beaugrand et al. 2009). It is hypothesized that phytoplankton are not the exception to the rule, and the historic latitudinal boundaries of their distribution are being altered due to increases in sea surface temperatures. Due to the cold-water requirements of two of the main winter-spring bloom species, *D. confervacea* and *T. nordenskioeldii*, the consistent seasonality of the winter-spring bloom in Narragansett Bay is hypothesized to have altered.

Traditionally, blooms are analyzed with respect to the abundance or concentration of cells of each species in the bloom. This gives a general idea of which species are in bloom and their relative cell abundances. However, if

an accurate measure of biomass is to be obtained, we argue that it is more accurate to convert cellular concentrations to carbon concentrations. Different species of phytoplankton, due to disparities in size or function, may require more or less carbon than the other species in the bloom. While knowing how many cells of each species are present has its value, when looking at biomass, it is better to know how each species contributes to the bloom with respect to carbon. Accordingly, the second aim of this project was to determine if the species that comprise the winter-spring bloom in Narragansett Bay have changed cellular concentrations over a 50-year time period, and to convert cellular concentrations to carbon concentrations to see how it affects carbon biomass representation.

Materials and Methods

Data acquisition and compilation

Unpublished historical data used for the first part of the project were obtained via personal communication with Theodore J. Smayda's lab and compiled into one dataset. Over the 50-year time period from 1959 to 2009 plankton samples were collected weekly off Fox Island in the lower west passage of Narragansett Bay. Samples were collected at the surface in 5-L Niskin bottles. Various physical conditions, including temperature, salinity, light penetration, and nutrients, were also recorded at the time of sampling. Unpreserved aliquots of the 5-L samples were taken to the TJS lab and analyzed for species composition and abundance (cells/mL). These measurements were taken using a -mL Sedgewick-Rafter counting chamber. The TJS lab provided the unpublished data for the three species, which are the focus of this study, *S. costatum* (s.l.), *D. confervacea*, and *T. nordenskioeldii*. In laboratory experiments samples of *S. costatum* (s.l.), *D. confervacea*, and *T. nordenskioeldii* were measured and average cell volume (μm^3) and average carbon content (pg C/cell) were determined for each species (Table 1). Additionally, published equations relating log-transformed cell volume to log-transformed carbon content were used for the sake of comparison (Table 2).

Table 1. Average cell volumes (μm^3) and the carbon content (pg C/cell) at that average volume for each species

Species	μm^3	pg C/cell
Skeletonema costatum (s.l.)	228	28
Detonula confervacea	778	59
Thalassiosira nordenskioeldii	5518	295

Table 2. Published carbon (C) estimate equations from volume (V) data

Researcher	Equation
Strathman (1967)	log C = 0.712(log V) – 0.314
Montagnes and Franklin (2001)	log C = 0.85(log V) – 0.42
Menden-Deuer and Lessard (2000)	log C = 0.811(log V) – 0.541

Statistical analysis

Cell volume (μm^3) and cellular carbon content (pg C/cell) in *S. costatum* (s.l.) were log transformed before being plotted as a scatterplot. The log of cell carbon was correlated to the log of cell volume, and a simple linear regression was carried out, yielding an equation. A range of controlled volumes, starting with 1.0 and increasing by 0.25 until reaching 3.0, was entered into our experimentally derived equation and three published equations (Strathman 1967, Montagnes and Franklin 2001, Menden-Deuer and Lessard 2000). The carbon outputs at each controlled volume from each equation were graphed as a scatterplot. In addition to the controlled volumes, the average cell volume for *S. costatum* (s.l.) was calculated and entered into the regression equation generated with our data. The cellular carbon output of the equation was removed from the log

transformation to yield the carbon content for the average *S. costatum* (s.l.) cell in picograms of carbon per cell.

The weekly sample cell concentrations (cells/mL) were averaged for each month of every year of the survey for each species. The winter-spring bloom was characterized as starting the December of the previous year and ending in April of the current year. For all years and for each species, the monthly cell concentration averages from December of the previous year to April were averaged to yield an average concentration for the winter-spring bloom of that year. In order to eliminate some potential noise in the data, the preferred timescale for analysis was pentad, or every five years. The yearly winter-spring bloom cell concentration averages were then averaged together in 5-year increments starting with the year 1960 until year 2009. The pentad cell concentration averages for each species were plotted as histograms.

In order to analyze the winter-spring bloom with respect to carbon, the cell concentrations (cells/mL) were converted to carbon concentrations (pg C/mL). The carbon conversion utilized the carbon value associated with the average cell volume of each species given in picograms of carbon per cell. Each pentade average for cell concentration was multiplied by the carbon content for the average cell volume of the respective species. This yielded carbon results in picograms of carbon per milliliter of seawater. The converted carbon concentrations (pg C/mL) for the pentade increments for each species were plotted as histograms. Total average carbon for all three species combined was calculated by adding together the average carbon concentration of all three species for each five-year increment and the total carbon values were then plotted as a histogram.

Results

The equation used to estimate cellular carbon from cell volume in *S. costatum* (s.l.) can be observed in Figure 1. Data that have been log transformed yield a stronger relationship, which allows for better estimates of cellular carbon. In general the observed log-transformed cell volumes lay within the range from ca. 1.6 to ca. 2.6 μm^3. While there is some variation in cellular carbon at a given volume, the general trend, represented by the simple linear regression, suggests that as cell volume increases, so too, does the amount of carbon within the cell. From the linear regression equation (Figure 1) the carbon content for the average cell volume in *S. costatum* (s.l.) was calculated. For *S. costatum* (s.l.) the average cell volume was 228 μm^3, and when log transformed and placed into the equation the carbon output was 1.44 picograms of carbon per cell. When removed from the log transformation, the carbon content in a *S. costatum* (s.l.) cell of average volume was calculated to be 28 picograms of carbon per cell (Table 1).

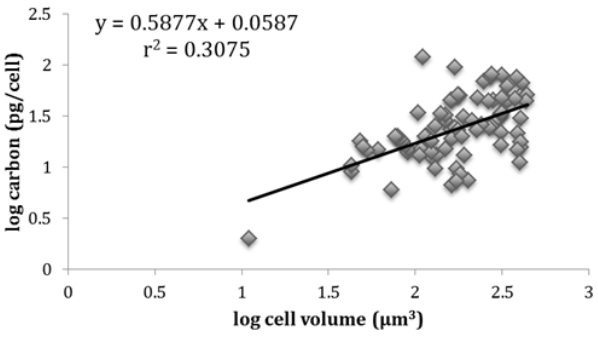

Figure 1. Relationship between log-transformed cell volume and log-transformed cellular carbon content.

When each equation is utilized to predict cellular carbon from cell volume, the amount of carbon increases with increasing volume (Figure 2). The equation for *S. costatum* (s.l.) generated in this study, overlaps with the equation published in Montagnes and Franklin (2001) at the narrow range of log volumes from 1.75 to 2 μm^3. Comparatively, for *S.*

costatum (s.l.) cells with small volumes, the equation by Montagnes and Franklin (2001) yields less carbon. For log-transformed cell volumes greater than 2, the Montagnes and Franklin (2001) equation yields more carbon, comparatively. The trends observed by Strathman (1967), and Menden-Deuer and Lessard (2000) are very similar and overlap over the wide range of log volumes from 1.5 to 2.75 μm^3. The trends observed in this study, Strathman (1967), and Menden-Deuer and Lessard overlap in the range of log-transformed volumes from 2.5 to 3 μm^3. For smaller cell volumes (<2.5 μm^3), the *S. costatum* (s.l.) trend in this study diverges from trend observed by Strathman (1967), and Menden-Deuer and Lessard (2000). The equation for this study yields higher cellular carbon values than the other equations for smaller cells.

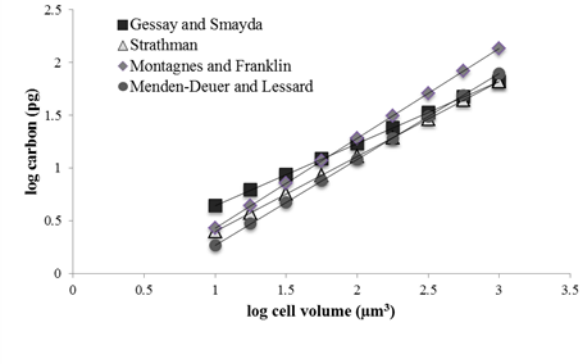

Figure 2. Comparison of linear cellular carbon estimate equations using known cell volumes.

The three winter-spring diatom bloom species in Narragansett Bay are present in very different relative cell abundances for all years (Figure 3). With time, there appears to be no apparent overall trend in *S. costatum* (s.l.) cell concentrations. There are years with greater cell concentrations (1960, 1965, 1980, 1995) followed by years with respectively lower cell concentrations (1970, 1985, 2000). *Detonula confervacea* cell concentrations decreased steadily from 1960 to 1980, until it begins to fluctuate in 1985 until 2000, when it almost completely disappeared. *Thalassiosira nordenskioeldii* cell concentrations were relatively steady between the years 1960 and 1985. However, starting in 1990 *T. nordenskioeldii* began to decrease until almost completely disappearing.

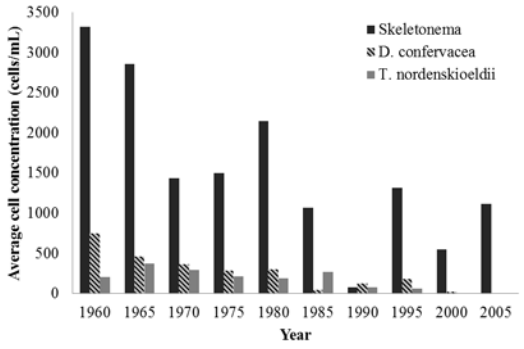

Figure 3. Winter-spring cell concentrations for each species for 5-year intervals.

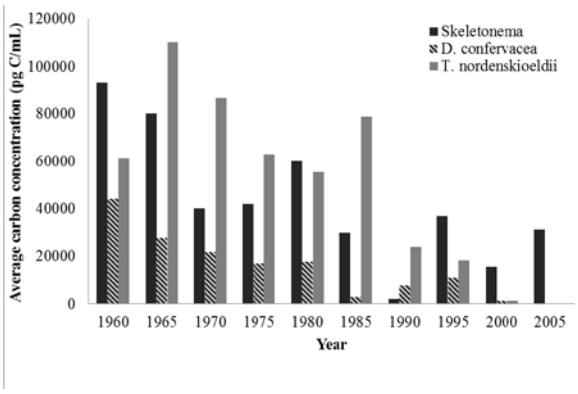

Figure 4. Winter-spring carbon concentrations for each species for 5-year intervals.

The cell concentration data from Figure 3 have been converted to carbon concentrations (Figure 4). The same overall trends described for each species in Figure 3 exist due to the fact that the conversion was made by multiplying the average cell concentration (cells/mL) by the amount of carbon (pg C/cell) found in a cell of average volume for each species. However, the magnitudes of the trends have been altered, since each species has a different average carbon content. *D. confervacea* had the lowest carbon concentration relative to the other two species

for every time interval with the exception of 1990. While *S. costatum* (s.l.) is numerically more abundant (Figure 3), with respect to carbon there are multiple time intervals where *T. nordenskioeldii* surpasses *S. costatum* (s.l.) in carbon concentration (1965, 1970, 1975, 1985, 1990).

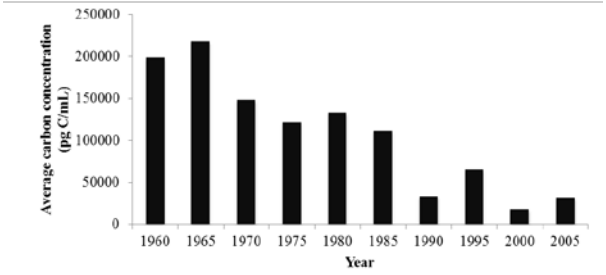

Figure 5. Average winter-spring carbon concentrations for all three species added together.

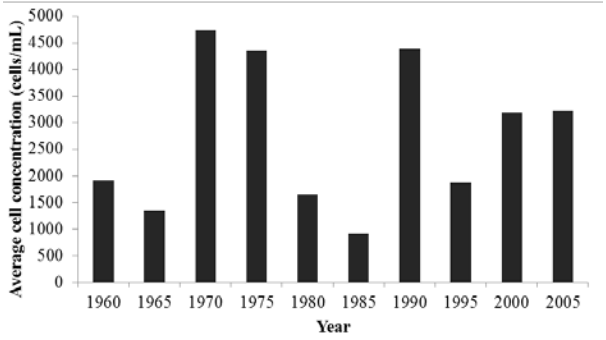

Figure 6. Summer-fall bloom Skeletonema cell concentration for 5-year intervals

The average carbon concentrations for all three species combined gradually decrease in winter-spring bloom carbon concentration with time (Figure 5). *Sketetonema costatum* (s.l.) cell concentrations in the summer-fall bloom (July-October) do not show a clear trend over time (Figure 6). Like in the winter-spring bloom, the summer-fall bloom *S. costatum* (s.l.) cell concentrations experience periods of greater concentrations (1970, 1975, 1990), followed by periods of lower concentrations (1980, 1995).

Discussion

It has been well established that estimates of cellular carbon for diatoms in general can be obtained from equations relating it to cell volume. While it is important and useful to be able to estimate carbon content in a general equation for any species of diatoms, it has limitations. It is important to understand how extremely abundant species contribute to the biomass in a system; assuming it follows the general diatom trend will not always yield accurate results. In Narragansett Bay, *Skeletonema costatum* (s.l.) is the most numerically important species of diatoms, and it is therefore important to understand if its carbon content diverges from the general diatom trend. From our data, we have derived an equation, which allows carbon content in *S. costatum* (s.l.) to be estimated from cell volume (Figure 1). This equation was compared to previous researchers' findings for all diatoms. Whereas some overlap of the trends is present, the carbon outcome generally depends on which equation was used. For cells with smaller log volumes (<1.75 μm^3) entered into the Montagnes and Franklin (2001) equation, the carbon content is underestimated; using the same equation, carbon content in larger cell volumes (>2 μm^3) are overestimated. The equations by Strathman (1967), and Menden-Deuer and Lessard (2000) both underestimate cellular carbon in cells with log volumes less than 2.5 μm^3. These overestimates and underestimates apparent in the general diatom equations support our hypothesis that carbon content in *S. costatum* (s.l.) does not follow the same trend as all diatoms when estimated using cell volume. Obtaining accurate biomass estimates for this key species in Narragansett Bay requires the species-specific relationship that we have discovered.

Phytoplankton blooms are generally analyzed with respect to species composition and measured in cell concentrations. Knowing what species are present in a bloom and how

abundant they are gives us valuable information about the system. However, this is only a starting point to understanding the biomass of the bloom. The winter-spring bloom in Narragansett Bay starts in December and ends in April, it contains three main species *S. costatum* (s.l.), *D. confervacea*, and *T. nordenskioeldii*. The five-year average cell concentrations of these species help us understand how the species structure of the bloom has changed with time. *Sketetonema costatum* (s.l.) was much more abundant relative to the other two species. It is unclear what ecological factors cause the periods of extreme abundance followed by periods of decreased abundance in *S. costatum* (s.l.); however, this pattern was observed in both the winter-spring and the summer-fall blooms. The gradual decrease in cell concentrations in *D. confervacea* and the eventual decrease in *T. nordenskioeldii* are thought to be due to increasing sea surface temperatures in the winter due to climate change. *Detonula confervacea* and *T. nordenskioeldii* require cold water to bloom; due to this cold water requirement, they are only found in Narragansett Bay during the winter-spring bloom. If the seawater during the winter-spring bloom becomes too warm, *D. confervacea* and *T. nordenskioeldii* will no longer be present. This behavior is observed in more recent years (Figure 3, years 2000, 2005) where cell concentrations were fewer than 100 cells per milliliter.

The decrease in cell concentrations is not only a detriment to the biodiversity of the bloom, but it affects the carbon biomass of the bloom considerably. We have shown that just because a species is numerically more abundant, that species may carry less importance when carbon biomass is concerned (Figure 4). In Narragansett Bay, *S. costatum* (s.l.) was the most numerically abundant species for every time interval, with the exception of 1990. However, when converted to carbon concentrations, *T. nordenskioeldii* often surpassed *S. costatum* (s.l.) in carbon concentration, although it was less abundant numerically. We argue that to fully understand biomass in Narragansett Bay, phytoplankton blooms must be converted to carbon concentrations. It is not always the case that the most numerous species contributes the most carbon the bloom biomass as we have demonstrated.

The winter-spring bloom in Narragansett Bay is ecologically important for benthic species. Zooplankton are not excessively abundant during the bloom and this causes a lot of the phytoplankton to sink and be preyed upon by filter feeding benthic invertebrate species. Insight into how the carbon biomass of the winter-spring bloom in Narragansett Bay has changed over time is given in Figure 5. When the five-year averages for each species are added together to yield a total carbon concentration for the winter-spring bloom, a clear general decrease in carbon concentration is observed with time. While our study is limited to just this observation, it is likely that this decrease in total carbon is due to the decrease in cell concentration of species *D. confervacea* and *T. nordenskioeldii*. These species prefer colder water than *S. costatum* (s.l.), and are therefore unable to thrive as climate warms. We have shown that *T. nordenskioeldi*i contributes more carbon than *S. costatum* (s.l.), although it is less numerous. The disappearance of these species is having a greater impact on the carbon biomass in the winter-spring bloom. Had only cell concentrations been considered, the large contribution of these species to the carbon biomass would not have been revealed.

Conclusions

When making estimates of cellular carbon from cell volume in the diatom *S. costatum* (s.l.), it is best to use a species-specific relationship. While it is important and insightful to understand cell concentrations of the winter-spring bloom in Narragansett Bay,

carbon conversions are necessary to fully understand the biomass characteristics of the bloom.

Acknowledgments. This research was supported by the National Science foundation (Grant #1460819). We would like to thank the Graduate School of Oceanography for hosting JKG for the duration of this project. Additionally we thank Chris Tedeschi for her support on this project.

References

Beaugrand, G., Luczak, C., and M. Edwards. 2009. Rapid biogeographical plankton shifts in the North Atlantic Ocean. Global Change Biology. 15:1790-1803.

Durbin, E. G. 1978. Aspects of the biology of resting spores of *Thalassiosira nordenskioeldii* and *Detonula confervacea*. Marine Biology. 45:31-37

Litchman, E., Klausmeier, C. A. and K. Yoshiyama. 2008. Contrasting size evolution in marine and freshwater diatoms. PNAS. 106:2665-2670

Menden-Deuer, S. and E. J. Lessard. 2000. Carbon to volume relationship for dinoflagellates, diatoms, and other protist plankton. Limnol. Oceanogr. 45: 569-579

Montagnes, D. J. S., and D.J. Franklin. 2001. Effect of temperature on diatom volume, growth rate, and carbon and nitrogen content: Reconsidering some paradigms. Limnol. Oceanogr. 46: 2008-2018.

Smayda, T. J. 1973. A survey of phytoplankton dynamics in the coastal waters from Cape Hatteras to Nantucket. Marine Publications series No. 2. University of Rhode Island. Kingston, Rhode Island, pp. 3-1-3-100.

Strathman, R. R. 1967. Estimating the organic carbon content of phytoplankton form cell volume or plasma volume. Limnol. Oceanogr. 12: 411-418.

Key Points:

- Estimations of cellular carbon from cell volume in *Skeletonema* should be made using a species-specific equation.
- It is better to analyze biomass in blooms with respect to carbon content opposed to cell abundance.
- Numerically more abundant species may contribute less carbon biomass to a bloom than less numerically abundant ones.

Key Index Words:
Biomass; *Skeletonema costatum*; carbon; bloom; seasonality.

Applications of Aerial Multi-spectral Imagery for Algal Bloom Monitoring in Rhode Island

Scott J. Goldberg[1,2], Jordan T. Kirby[2], and Stephen C. Licht[2]
[1]Program in Biological Sciences, Northwestern University, Evanston, IL 60208
[2]Department of Ocean Engineering, University of Rhode Island, Narragansett, RI, USA
Corresponding author: scottgoldberg2017@u.northwestern.edu

Abstract
Harmful algal blooms (HABs) may lead to the production of toxins that are dangerous to humans and animals. Current methods of monitoring these events are slow and imperfect. Many tests require taking nearshore water samples followed by laboratory analysis, often yielding data with low spatial resolution. By expanding upon current research to utilize autonomous vehicles to observe HABs, this weakness may be overcome. A small unmanned aircraft system (sUAS) utilized multispectral cameras to create a normalized difference vegetation index (NDVI), known to have a high correlation with algal biomass. The ultimate goal of this research is to compare discrete water samples, such as some collected by an autonomous kayak, to aerial photographs taken at the same time and place for a more holistic view of the HAB. These tests investigated the differences in results of two camera set ups. One was using a Tetracam Mini-MCA6, which can take images in five different spectra; the other was using four different MAPIR cameras taking images in visible light, red, green, and near IR spectra. Until recently, this work was not feasible as sUASs were not easily available for civilian usage. By expanding on existing sampling techniques and adding a new observation method, this work strives to greatly improve monitoring of HABs and thus aids management.

Algal blooms are caused when an excess of a limiting nutrient enters a body of water. This is most commonly associated with excess fertilizers from farms running off into a water system (Anderson et al., 2002). Some of these blooms are made up of cyanobacteria, which produce cyanotoxins. These cyanotoxins have been shown to be dangerous to animals through both contact and ingestion (Briand et al., 2003). These blooms are often call harmful algal blooms or HABs.

It is important to be able to monitor a HAB in order to determine how dangerous it is and where the toxic levels are highest. Generally, this consists of collecting water samples which are later taken to a lab to be analyzed. This often takes a few days, which leads to problems. Given that HABs are complex and dynamic systems, their distribution and intensity are likely to change over time. Limited sampling which may not include the entire body of water makes predication difficult. In other words, one only understands how part of the HAB was a few days ago, thus predicting any changes is unlikely to be accurate (Merwe and Price, 2015).

Alternative monitoring methods have been tried, but have run into their own complications. One such alternative is the use of helicopters or planes to take images of HABs to monitor algae concentrations, but the cost of fuel is a deterrent. Another method is using satellite imagery to take images of HABs. This can also be expensive and if the orbit does not line up perfectly, getting repeated images of a site may be difficult (Pozo et al., 2014).

The goal of this project is to investigate the possible use of autonomous vehicles to monitor HABs. This comes in two parts, the first of which involves an autonomous kayak to collect water samples from throughout the entire body of water, along with several sensors to assess water conditions. The kayak is paired with a second vehicle, the primary focus of this study, a small unmanned aircraft system, or sUAS, which takes images in the infrared and specific visible spectra of light to create a normalized difference vegetation index, NDVI. A NDVI is an index known to highly correlate with biomass in plants and cyanobacteria (Merwe and Price, 2015). This can provide three advantages for monitoring. One, combining the sampling data from the kayak and the images from the sUAS of the entire body of water, gives a much more complete view of the HAB than traditional methods. Two, NDVI images can be processed faster than samples can be analyzed. While sampling data are still important, these images can help provide management with quick first response data. Three, an sUAS does not disturb the bloom, as it makes no contact with the water surface and flies high enough that any force from the props is minimal by the time it gets to the surface.

Materials and Methods

The sUAS's

Initial tests were conducted using two different sUAS's. The first was a 3DR X8+ (3D Robotics, San Diego, CA, USA) with a payload of up to 800 g and an estimated maximum flight time of 15 minutes (https://3dr.com/wp-content/ uploads/ 2014/ 11/X8+-Operation-Manual-vA.pdf, 8/18/2016). The second sUAS used was a 3DR Iris+ (3D Robotics, San Diego, CA, USA) with a maximum payload of 400 g and an estimated maximum flight time of between 16 and 22 minutes (https://3dr.com/wp-content/uploads/2015/02/IRIS-Plus-Operation-Manual-vH-web.pdf, 8/18/2016).

The cameras

For the initial tests, two different camera rigs were used. One was the Tetracam Mini-MCA6 (Tetracam Inc., Chatsworth, CA, USA), from here on referred to as the MCA (Figure 1). This is a multispectral camera with five different channels (750, 700, 660, 620, and 550 nm) and an incident light sensor. Each channel is taken by a camera with a filter corresponding to its spectrum. When flown, the MCA was powered directly from the sUAS. All images are stored on compact flash cards (one card per channel) and processed in PixelWrench2 (Tetracam Inc., Chatsworth, CA, USA).

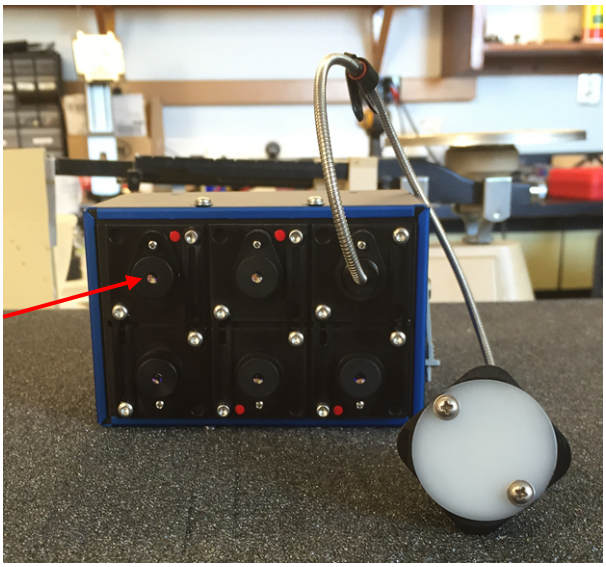

Figure 1. The Tetracam Mini-MCA6. The arrow is pointing to one of the five spectral cameras. The white circle is the light sensor, which was mounted to face the sky during missions.

The second camera rig was four different MAPIR Survey 1 cameras (Peau Productions Inc., San Diego, CA, USA), from here on referred to as the MAPIRs (Figure 2). Each camera used had a different spectrum (808, 650, 548 nm, and one that looks at the entire visible spectrum). When flown, the MAPIRs were powered directly from the sUAS. The images are stored on SD cards and later

processed in MATLAB (MathWorks, Natick, MA, USA).

Figure 2. The four Survey 1 MAPIRs mounted to a 3DR x8+. Each camera takes images in different spectra. From top left going clockwise: near infrared, visible light, green, and red.

Regardless of camera, the images were mosaicked using either Agisoft PhotoScan Professional Edition (Agisoft LLC, St. Petersburg, Russia), hereafter referred to as Agisoft, or DroneDeploy (Infatics Inc., San Francisco, CA, USA). The former is a structure from motion software designed for 3D reconstruction of scenes from single 2D images, whereas the latter is an online service designed for the mosaicking of images.

2.3 Flight Planning and Flying

The first step in flying over a body of water was planning the mission once a HAB was located by checking the Rhode Island Department of Health (RIDH) website for listed HABs. The RIDH Toxicology Department was then called in order to confirm the HAB. Next, the flight plan wass created using the program Mission Planner (ArduPilot, Online). The program works from an area to fly over and generates a mission based on the specifications of the camera used along with user inputted parameters, such as altitude, percent image overlap, and velocity. This mission was then written to the copter to ensure that, even if the mission control computer went down, the copter could automatically fly the mission on its own. When performing a joint mission with the kayak team, the survey area was determined by the area of the kayak's mission.

Once on site, the mission control was set up to allow the copter to send back telemetry data during the flight. Emergency landing points were chosen, although putting the sUAS in the water was a last-resort option. After the camera rig was mounted on the sUAS, the unit took off and was flown over a calibration plate (Teflon adhered to wood) for a photograph. The sUAS was then put into auto mode and flew the mission. At the end of the mission, the sUAS was flown back and the images were ready to be analyzed.

Processing the Images.

The initial methods for image processing are different depending on the camera rig. For the MCA, system images were aligned in Pixelwrench2, i.e., the program finds where image 1 from all the cameras overlap, and makes a new image by layering those images 1. The images were then given false coloring and turned into NDVI and GNDVI (green normalized difference vegetation index) images. These indices were made into one mosaic image using either Agisoft or DroneDeploy. For the MAPIRs, the images were run through a MATLAB program that creates either NDVI or GNDVI images. These images were then mosaicked using either Agisoft or DroneDeploy.

Data

Due to the nature of this project a HAB was required for sampling. Unfortunately, no HAB occurred once the hardware was ready.

Results

Despite having no data, the test flights conducted over land did identify a number of issues that any future endeavor will have to overcome. These issues all are related to processing the images.

For the MAPIRs, one of the major issues was aligning the images (Figure 3). Since the mount holding the cameras bends slightly, any programmatic attempt would have to account for translational differences in pictures (the lenses of the four cameras do not share the same location), and rotational differences (the cameras are not all pointed at the exact same angle). This has proven difficult, and attempts to fabricate a mount with stronger materials have helped, but not enough to prevent errors in the final NDVI and GNDVI images.

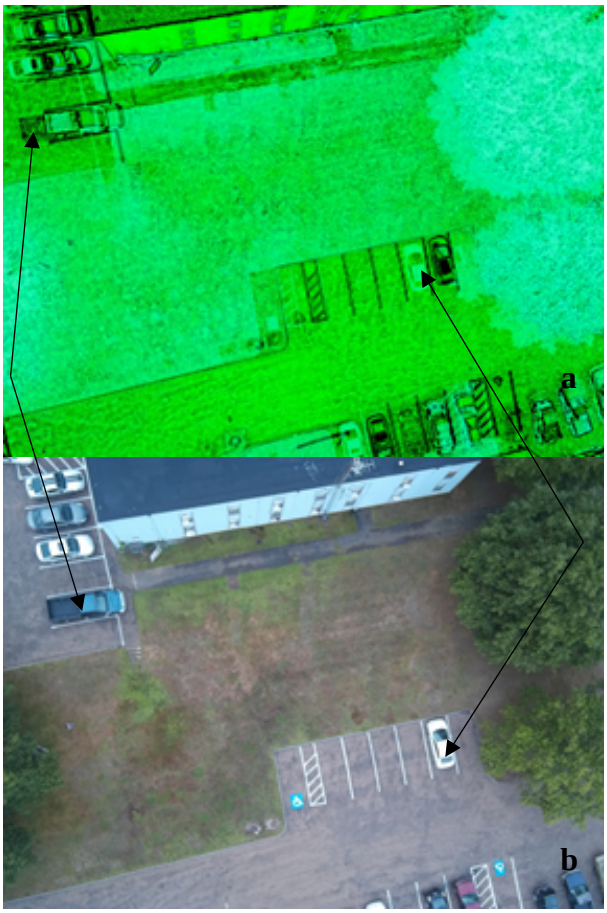

Figure 3. A comparison of a NDVI image (**a**) made using the MAPIRs in MATLAB and the visible light image (**b**) taken at the same time. Note how the white car in visible light (**b**) has a duplicate version in (**a**). There is a similar effect with the bed of the blue truck in the top left of each image. This stems from imperfect alignment of images used to make the NDVI.

Regardless of camera, both programs used for mosaicking have proven unreliable (Figure 4). Agisoft was originally designed to take images and make 3D models, thus has trouble creating flat images when the ground is not flat. DroneDeploy, on the other hand, does not generate quality results, often only mosaicking a small portion of the sample area, and not always to the highest quality. Agisoft has a minor advantage as its design allows for the user to fine tune certain aspects of the mosaic, whereas DroneDeploy simply takes the images and returns an output.

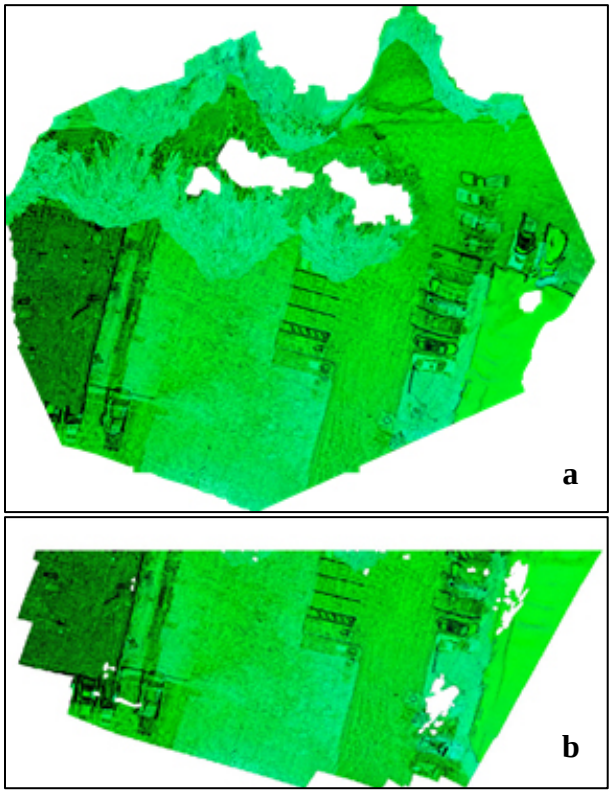

Figure 4. A comparison of an NDVI mosaic made using Agisoft (**a**) and one made using DroneDeploy (**b**). Each is imperfect. The Agisoft image is missing parts of the ground and everything around the edges is a bit warped. The DroneDeploy image is missing the top half of the image, and is still a bit warped elsewhere.

Discussion

This study of aerial imagery for the purpose of monitoring algal blooms identified serious issues related to image processing, and compiled a few possible corrections. The most obvious issues are the misalignment of the MAPIR images, and the imprecise mosaicking of the images. There are three possible options to help improve alignment of the MAPIR images. One would be to design a new mount that does not bend at all. At high altitudes, translational displacement becomes less pronounced, while rotational displacement becomes a bigger issue. If one could remove rotational displacement all together, the remaining form of displacement may not only be negligible, but much easier to write code to account for. This simply means that the mount design should be modified. An attempt to simply use stronger plastic did not solve the issue; however, by making the mount thicker or adding in more supports, bending might be negated.

Improving on mosaicking the images is far more difficult. While some of the issues with the software may be overcome by the fact that most images from tests will be over water, this ignores what will probably be the greatest challenge in mosaicking the images in the long run, water. Mosaicking programs like those mentioned above work by finding where images overlap based on GPS tags and finding overlapping features, ie: if the program sees that a car is in one image and the same car is in another image, it knows there is some overlap. If most of the pictures over a HAB are featureless water, the programs may have difficulty determining how much overlap the images have. A possible solution would be to fly high over markers on the water surface to use as reference points. This solution has the added benefit that the markers could also be used as calibration tiles.

The best option moving forward would be to use an NDVI camera. These cameras do not require picture alignment and many options are available for mosaicking and calibrating.

Acknowledgments. SJG was supported by a Summer Undergraduate Research Fellowship in Oceanography (SURFO) (National Science Foundation REU grant # OCE-1460819). We thank the Chris Roman Lab for the autonomous kayak, and the EPA for loaning us the Tetracam MINI-MCA6.

References

Anderson, D.M., Glibert, P.M., Burkholder J.M. 2002. Harmful Algal Blooms and Eutrophication: Nutrient Sources, Composition, and Consequences. Estuaries 25(4b):704-726.

Briand, J-F., Jacquet, S., Bernard, C., Humbert, J-F. 2003. Health Hazards for terrestrial vertebrates from toxic cyanobacteria in surface water ecosystems. Vet. Res. 34(4): 361-377.

Merwe, D.V., Price, K.P. 2015. Harmful Algal Bloom Characterization at Ultra-High Spatial and Temporal Resolution Using Small Unmanned Aircraft Systems. Toxins 7: 1065-1078.

Pozo, S.D., Rodríguez-Gonzálvez, P., Hernández-López, D. 2014. Vicarious Radiometric Calibration of a Multispectral Camera on Board an Unmanned Aerial System. Remote Sens. 6: 1918-1937.

Key Points:

- The use of sUAS's in algal bloom monitoring is complicated by difficulties with image processing

Key Index Words:
Harmful Algal Blooms; Multi-spectral Imagery; sUAS; autonomous vehicles

Light-induced morphological variation in diatoms

Austin R. Grubb[1, 2] and Jan E.B. Rines[1]
[1]Graduate School of Oceanography, University of Rhode Island, Narragansett, RI 02882-1197 USA. [2]Department of Biology, Susquehanna University, Selinsgrove, PA 17870
Corresponding author: grubb@susqu.edu

Abstract
Diatoms are a group of phytoplankton that form cell walls from silica, which allows them to develop complex morphologies. Intraspecific morphological variation is common and is caused by a variety of factors including response to environmental conditions. Recent advances in holography performed *in situ* demonstrate that orientation of diatom colonies in the water column may vary under different hydrographic conditions. The physical conditions that lead to horizontal particle orientation are most commonly observed near the pycnocline, where light levels are lower than near the surface. Chain-forming diatoms may regulate the length of their colonies, which alters their entrainment in flow and thus their physical orientation, thereby increasing the area for light absorption. We hypothesize that diatoms form longer colonies under low light conditions. *Chaetoceros* physiologically regulate their colony length, and complete, unbroken colonies are easy to distinguish by their specialized hair-like terminal setae, which are very distinct in *C. constrictus*. We cultured *C. constrictus* at high (~115-160 µmol photons m^2sec^{-1}) and low (~30-55 µmol photons m^2sec^{-1}) light intensities at cell/colony concentrations representative of those found in nature. Cell fluorescence was measured daily, and photomicrographs were analyzed for colony length. Differences in growth rates between different developmental stages were not significant, but growth rates obtained from cell counts were different from those generated from fluorescence readings. Growth rates were greater under high light conditions than low light conditions. Preliminary analyses of length frequency data suggest that longer colonies form in high light, however analyses are still in progress.

Phytoplankton are photosynthetic protists present in nearly all aqueous environments. They are responsible for about half of the earth's total net primary production (Field et al. 1998). Diatoms are a widespread and abundant group of phytoplankton that form their cell walls from silica. Although diatoms are single celled organisms, many employ diverse strategies including mucus pads (e.g. *Asterionellopsis*), mechanically interlocking spines/hooks (e.g. *Rhizosolenia* and *Cerataulina*), chitan threads (e.g. *Thalassiosira*), and fusion of silica (e.g. *Chaetoceros* and *Bacteriastrum*) in order to form colonies of cells, which may increase particle size by several orders of magnitude. The ecological role(s) of complex morphology has fascinated scientists for more than a century (Gran 1912; Sournia 1982), but insight has remained elusive.

Kociolek and Stoermer (2010) note that there is a host of factors that can affect diatom morphology, from developmental and genetic to environmental factors. However, although many environmental factors including temperature, salinity, silica concentration, seasonality, pH were reviewed, there was no discussion of light. It is well known that light impacts the growth rate of diatoms, but little investigation has been carried out to determine

what impact, if any, light has on diatom morphology.

Light intensity decreases with depth in the water column, therefore low light situations occur naturally in areas like the pycnocline, decreasing the potential for photosynthesis. In this region, it is not uncommon for horizontal flow or shear to entrain colonial diatoms, gently pulling them into a horizontal orientation. Indeed, recent *in situ* observations using holographic instruments have shown that diatom colonies are often oriented horizontally as opposed to randomly in the water column (Malkiel et al. 1999; McFarland et al. 2016; Nayak et al. 2016; Nayak et al. *in prep*). Horizontal orientation would expose more cell/colony area to incident light, increasing its photosynthetic potential. Under these circumstances, longer colonies would be more easily captured in a horizontal flow and would extend the area (or "footprint") of a single colony and reduce the area available for competitors. Longer colonies would be favored under these specific environmental conditions.

If longer colony length enhances entrainment in anisotropic shear flow, resulting in horizontal orientation and increased photosynthetic potential, diatoms might regulate their colony length to take ecological advantage of this phenomenon. In this study, we ask whether longer colonies are formed when growth is light limited. One challenge in conducting this type of experiment is determining whether the measured colony lengths are a function of growth in the experimental conditions, or of bias (i.e. breakage) resulting from the sub-sampling and handling necessary to make the measurements. Therefore, we selected an experimental diatom in which physiologically regulated colonies are visually recognizable, thus intact vs. broken colonies can be easily distinguished.

Chaetoceros are chain-forming diatoms with differentiated cells. They have specialized, elongated and hollow projections made of silica called setae that are formed as the cell divides (Rines and Hargraves 1988). Setae form first as protrusions in the corners of the cell after the girdle bands have recently separated. In intercalary cells, or cells that are not at either end of the colony, adjacent setae are fused near their bases, holding cells together into chains (Pickett-Heaps 1998a; Pickett-Heaps 1998b). This is not the case in terminal setae, which occur in terminal cells. They are not fused, and thus act as colony separation valves, allowing a colony to divide in two. The frequency of formation of terminal valves/setae thus regulates the number of cells per colony in this genus. The setae that form from the terminal valves are more distinct than those formed within the colony, especially in *C. constrictus*. This makes *Chaetoceros* ideal taxa to work with for our purposes since it allows us to differentiate between colonies broken due to handling or excessive turbulence and physiologically regulated colonies, in other words, complete, unbroken colonies whose morphology reflects growth in the experimental conditions.

Lab grown cultures are typically much denser than what is found in nature, even in a typical season (Rines 1985; Rines and Hargraves 1987; Rines *unpublished*). Observations from preliminary experiments have shown that diatoms form better morphologies in these lower densities. Likewise, in order to truly understand what affects diatom morphology, we want to replicate natural conditions as much as possible in our cultures.

We first conducted a small-scale (200-mL flasks) preliminary experiment, and used these results to guide a second, large-volume (10-L tanks) experiment. Here, we compare the effects of light on two different developmental stages in the diatom life cycle, before and after auxospore formation. In addition, we determined whether differences exist in data collection methods for generating growth

rates. Lastly, we determined if there are any morphological or growth rate differences in light treatments or high light and low light conditions. For our large-volume experiment, we compare morphologies and growth rates between two light treatments, high and low. We hypothesize that longer colonies form in low light conditions.

Materials and Methods

Experiments were conducted with *Chaetoceros constrictus* clone B6, isolated from Narragansett Bay on May 25, 2016. This clone underwent auxospore formation in culture, so that the initial culture then contained both pre-auxospore and post-auxospore colonies. A post-auxospore colony was re-isolated to initiate sub-clone B6b, which was used for the large-volume tank experiment. Diatoms were grown in f/4 medium with L-metals (Anderson 2005) made from 0.2-µm filtered seawater. Seawater for stock cultures and the preliminary experiment was collected on June 13, 2016 whereas seawater for the large-tank experiment was collected on July 14, 2016.

Small-scale flask experimental design

Two replicate cell counts in a Sedgewick-Rafter counting chamber using a 10x objective were made of an inoculum culture of clone B6 in exponential growth. We inoculated four 250-mL Erlenmeyer flasks containing 200 mL of medium with ~10 cells/mL after completing 1:10 dilution of the inoculum culture. Two of the flasks were covered with two layers of commercial window screening to simulate a light-limited environment. The cultures were grown on a 16:8 L:D cycle at 15ºC at 150-160 µmol photons m^2sec^{-1} without screening and 50-55 µmol photons m^2sec^{-1} with screening using a Biospherical Instruments QSL2101 PAR collector.

Each day, three replicate cell counts were completed for each flask and a Molecular Devices SpectraMax M5 plate reader and the accompanying software SoftMax Pro 5 were used to gather fluorescence data from each flask, with settings at excitation 455 nm, emission 680 nm, and cutoff 665 nm. We used a 12-well plate and utilized the leftmost and rightmost columns as blanks by always filling each well with 5 mL of sterile filtered seawater. Then each well in the center left column was filled with 5 mL of the first replicate of a treatment, and the wells of the center right column were filled with 5 mL each with the second replicate of the same treatment. This was repeated for the other experimental condition. This continued for four days total for the flasks without screening and for five days total for the flasks with screening. On their respective final days, samples from each flask were concentrated with a 15-µm mesh Nitex sieve and photographed at 4x using a Nikon Eclipse E800 light microscope equipped with a SPOT Insight 2Mp FW Color Mosaic Model 18.2 camera using SPOT Software version 4.6.

Large-volume tank experimental design

Experiments were conducted in four 10-L tanks with horizontal stir bars at two vertical oscillations $minute^{-1}$, which created a gentle turbulence, similar to the protocol from Sullivan et al. (2003). Previous work (Rines et al. *in prep*) has shown that large volumes, low concentrations and gentle turbulence which can be achieved with this setup enhance the formation of diatom colonies with a morphology characteristic of wild populations.

An inoculum culture of clone B6b was grown for four days, and its concentration determined by two replicate cell counts. We used the B6b post-auxospore clone because in the small-volume experiment we determined that the smaller pre-auxospore colonies were too challenging to quantify. We added 25 mL of inoculum culture to each tank to have a starting cell concentration of ~10 cells/mL. Two of the tanks were covered with two layers of commercial window screening to

simulate a light-limited environment. Cultures were grown at 15ºC and on a 12:12 L:D cycle. The light level of the non-light limited tanks was ~115 µmol photons m^2sec^{-1} and the light level for the screened, light limited tanks was ~33 µmol photons m^2sec^{-1}.

Each day, fluorescence data were collected using the same methodology described above. Samples were not collected on the first day because the tanks had been inoculated for less than 24 hours. Starting on the second day of the experiment, samples from each tank were concentrated and photographed using the sampling procedure previously described. This was repeated each day for three days for each tank, with the exception of Tank D not photographed on day two. Image processing software ImageJ 1.50i with Java 1.6.0_65 was used to analyze photomicrographs from each protocol. Three separate measurements were made on each complete physiological colony: the maximum length from the tips of either terminal seta, the length of the cell bodies between the two terminal valves, and the number of cells per colony.

Growth rates for both experiments were calculated to determine if any differences exist between the light treatments, data collection methods, and developmental stages using the formula:

$$k = \left[\frac{\log(N_1/N_0)}{t_1 - t_0}\right] \times \frac{1/\log e}{\ln 2}$$

where N_1 and N_0 are two data points (generated from cell counts or from the fluorescence readings) at two points, t_1 and t_0 respectively. The value of k is expressed in divisions per day (Stein 1979).

Statistical Analysis

In order to analyze the measurement data, Microsoft Excel for Mac (Version 15.23.2) data analysis histogram function was used. For comparing between growth rates calculated from cell count data and fluorescence data and light treatments, an ANOVA Two-Factor with Replication test was completed. Similarly, an ANOVA Two-Factor with Replication test was used to compare differences in growth rates based on developmental stages and light treatments using data from cell counts. To determine differences between only light treatments in the second experiment, an ANOVA Single-Factor test was completed.

Results

In both the small- and large-volume experiments, we were able to grow colonies with excellent morphologies, that is to say, morphologies similar to what is found in nature. For the small-volume experiment, we compared pre-auxospore colonies (Fig. 1a) to post-auxospore colonies (Fig. 1b) to determine what differences exist in their growth rates and morphologies.

When analyzing photomicrographs for morphological differences, we only used complete physiological colonies (Fig. 1), which were discernible from broken colonies (Fig. 2a) due to their distinct terminal setae (Fig. 2b). This also allowed us to distinguish between very long colonies and two colonies that had not drifted apart at the time they were photographed.

Small-scale flask experiment

There were no significant differences in the growth rates (calculated from cell counts) between developmental stages (i.e. pre- and post-auxospore cells and colonies) ($p=0.554$) (Table 1). There was a significant difference between the growth rates obtained from cell counts and those generated from fluorescence reading ($p=0.009$). In most cases, the fluorescence readings used as a proxy for chlorophyll readings generated lower growth rates than rates from cell counts. Growth rates were consistently greater under high light conditions than low light conditions (Table 1).

On the last day of the experiment, there were many more post-auxospore than pre-auxospore cells present. There were no large

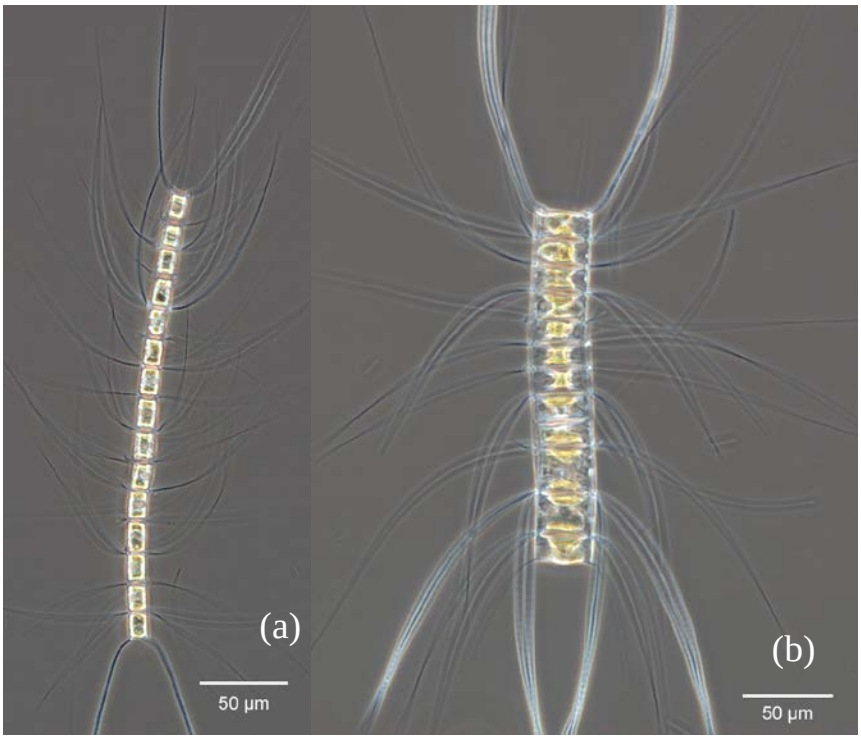

Figure 1. *Chaetoceros constrictus* a) pre-auxospore and b) post-auxospore colonies photographed at a 20x magnification.

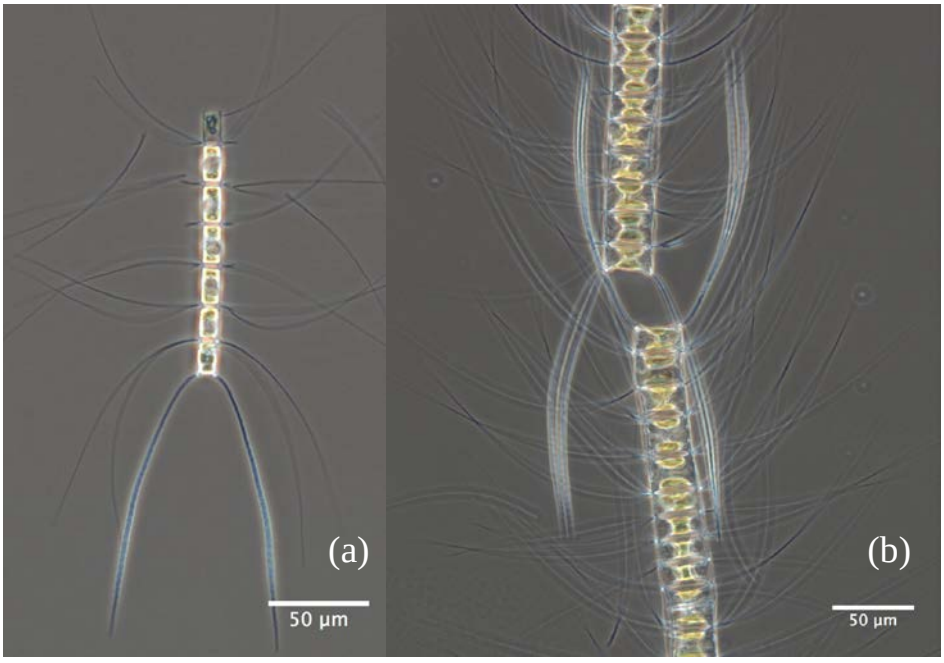

Figure 2. Broken colony of *Chaetoceros constrictus* (a) and two colonies that recently separated with distinct terminal setae (b).

Table 1. Growth rates from the small-volume experiment under high and low light conditions comparing developmental stages and data collection methods. Developmental stage refers to the point in the life cycle of the cells in the colonies (directly before or after auxospore formation). Units in divisions day^{-1}.

	Developmental Stage		Data Collection Method	
Light Condition	Before auxospore formation	After auxospore formation	Cell Counts	Fluorescence Readings
High	2.8	2.6	2.7	2.4
	3.0	3.7	3.2	3.3
Low	0.9	1.6	1.3	0.8
	1.9	1.6	1.6	0.8

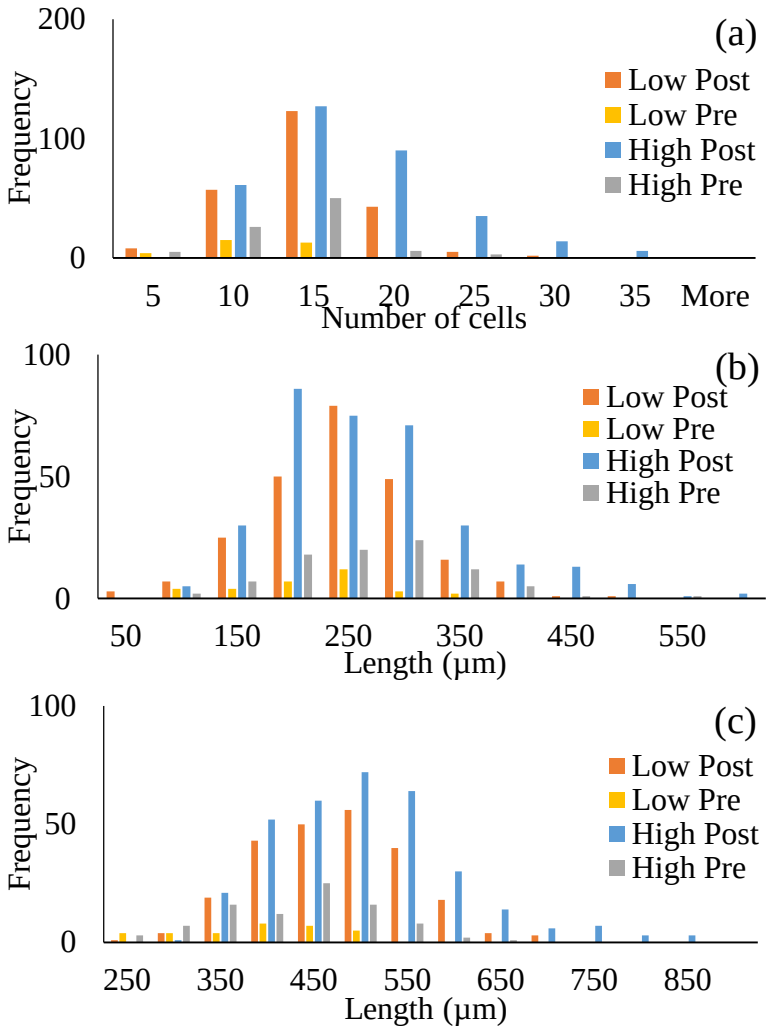

Figure 3. Colony length from the small volume experiment of pre- and post auxospore cells and colonies under high and low light conditions, as measured by a) the number of cells in each colony, b) the length of the colony from either terminal valve, and c) the length of the colony from the tips of both terminal setae.

differences in length between trends for the pre- and post-auxospore cells and colonies. Whereas the modes appear similar between light treatments, the size-frequency distributions are not identical (number of cells in each colony, the colony length from terminal valve to terminal valve, and the colony length from the tips of both terminal setae) suggesting that longer colonies were more prevalent under the high light regime, whereas short colonies were more prevalent under the low light regime (Fig. 3). Only one replicate of each treatment has been quantified at this time.

Large-volume experiment

For the large-volume tank experiment, the same pattern held between growth rates of post-auxospore cells under high and low light regimes; high-light growth rates were consistently greater than low-light growth rates ($p=0.019$) (Table 2).

Table 2. Growth rates from large-volume experiment under high and low light conditions. Units in divisions day^{-1}.

Replicate	High	Low
1	1.3	0.1
2	1.0	0.2

On the second day of this experiment, a pattern similar to what was seen in the small-volume experiment was observed. The longest colonies appeared under high-light conditions and the shortest under low light. On the fourth and final day, colonies in both light treatments were shorter by each measurement standard: the number of cells in each colony, the colony length from terminal valve to terminal valve, and the colony length from the tips of either terminal seta (Fig. 4). The reduction in colony size was most apparent when comparing the lengths of the cell bodies, as colonies became nearly half as long by the final day (Fig. 4b&e). On day four the terminal setae were longer in the high light treatments (Fig 4f). However, this is not based on all collected data, as data analysis is still in progress (Table 3). Because of this, a proper statistical analysis of the results has not taken place at this time.

Discussion

High light conditions consistently generated greater growth rates in the 200-mL small-volume experiments, which was expected because increased light allowed for more photosynthesis to take place. As determined by cell counts, there were no differences in growth rates between developmental stages. The lack of a significant difference between the growth rates of pre- and post-auxospore cells suggest that they have a similar physiology that regulates the rate of cell division. However, since these two life history phases differ in cell size, differences may also exist that relate to cell volume, which could be investigated further. There was always a difference in growth rates generated from cell counts and from fluorescence readings; this raises the possibility of a correction factor generated in future work to compensate for the differences. This would significantly reduce the time needed to collect data, however, since cells cultured under different light levels may contain different amounts of chlorophyll, any adjustment would need to be tailored for different light conditions.

Longer colonies were formed under high light conditions, which was not expected. Since there were no length differences between pre- and post-auxospore colonies, the cells most likely had a similar physiology under our experimental conditions. More work would be required to determine what differences exist or to explain why they retain a similar physiology. However, the analysis of the replicate set of data for the colony measurements is incomplete and therefore there is no statistical analysis completed to determine if the differences or lack thereof are significant.

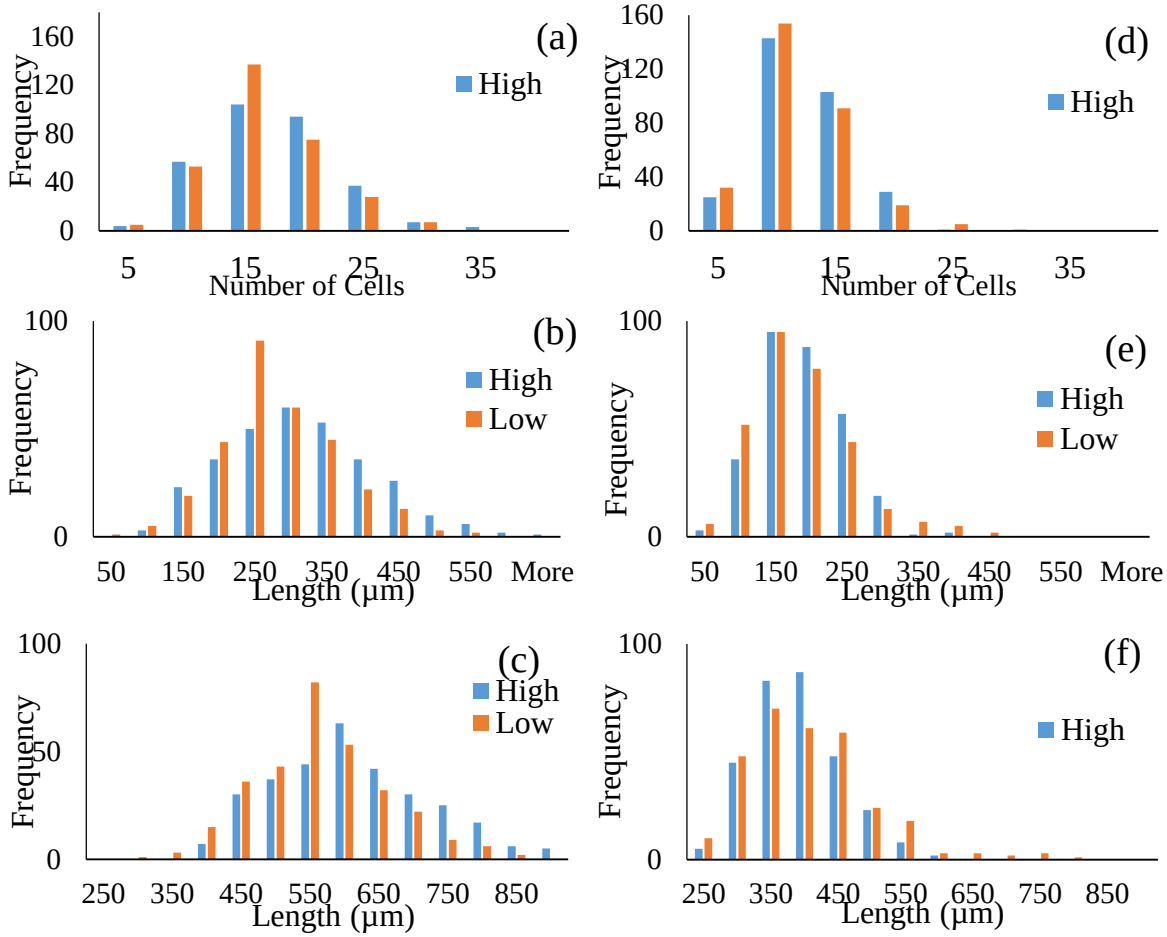

Figure 4. Colony lengths from the large-volume experiment of post-auxospore cells and colonies under high- and low-light conditions; measurements taken on day two were a) the number of cells in each colony, b) the length of the colony from either terminal valve, and c) the length of the colony from the tips of both terminal setae, and measurements taken on day four, d) the number of cells in each colony, e) the length of the colony from either terminal valve, and f) the length of the colony from the tips of both terminal setae.

Table 3. Data collected and analyzed are indicated with an "X," whereas data that have not been analyzed are left blank. Gray shaded cells indicate that no measurement data were collected.

	Data analyzed							
	Small-Volume Experiment				Large-Volume Experiment			
Light condition	High		Low		High		Low	
Day of experiment	1	2	1	2	Tank A	Tank B	Tank C	Tank D
1								
2					X		X	
3								
4	X				X		X	
5			X					

In the larger volume 10-L tank experiment, growth rates were also greater under high light conditions than low light conditions. In fact, the growth rates for the low light treatment were so low that cells would be expected to divide only once every 8 days – two times the duration of our experiment (Table 2). This very low growth rate could also indicate that very few (if any) cells divided at all, but rather, the amount chlorophyll per cell increased to compensate for the very low light conditions (Geider 1987). This means that the morphologies in the low-light treatments are likely representative of the morphologies of the inoculum culture, which was grown under high light for three to four days, and do not represent growth under the low light experimental condition.

As in the 200-mL flask experiment, longer colonies were also seen in the high light treatment in the large volume-(10L) experiment. Over time, colonies grew shorter in both light regimes. Even though these results seem to directly contradict our hypothesis, after analyzing the growth rate data for the low light experiment and realizing that the colonies were unable to grow sufficiently, we are unable to completely reject our initial hypothesis. In addition, data analysis and the accompanying statistical analysis are incomplete, which has prevented us from doing a statistical test to determine if any differences are significant.

However, the decreasing cell length over time raises intriguing points. The density of the colonies in the high light regimes undoubtedly increased significantly, and corresponds with the reduction in colony length, which leads us to ask whether the two factors are related and what might regulate this interaction. Even though we were able to create a gentle turbulence, we were unable to create a horizontal orientation, which was a significant part of our hypothesis and may affect the colonies differently. It is also possible that light intensity is not the factor which regulates the frequency of terminal valve formation (and thus colony length) in *Chaetoceros,* or that it is affected by a multitude of factors.

Conclusion

The tantalizing but preliminary evidence from both experiments suggest that light may very well impact diatom morphology. It was confirmed that greater growth rates occur under high light conditions. Data and statistical analyses are incomplete, but once completed, they will help to clarify our results, and allow for further refinement of questions to pose and development of the proper methodology needed to address them.

Acknowledgments. AG was supported by a Summer Undergraduate Research Fellowship in Oceanography (SURFO) (National Science Foundation REU grant # OCE-1460819). We thank Lucie Maranda as director of the SURFO program and for her assistance in calculating the growth rates. We thank Rodrigue Spinette for his technical expertise and teaching us how to use the plate reader. We thank Jim Sullivan, Aditya Nayak and Malcolm McFarland for their input in the experimental design and for access to unpublished work. We thank Melissa Omand for using her holographic microscope to view some colonies.

References

Anderson, R. 2005. Algal culturing techniques. Elsevier Academic Press.

Field, C., M. Behrenfeld, J. Randerson, and P. Falkowski. 1998. Primary production

of the biosphere: integrating terrestrial and oceanic components. Science. 281: 237–240.

Geider, R.1987. Light and temperature dependence of the carbon to chlorophyll a ratio in microalgae and cyanobacteria:

implications for physiology and growth of phytoplankton. New Phytol. 106: 1-34.

Kociolek, J. and E. Stoermer. 2010. Variation and polymorphism in diatoms: the triple helix of development, genetics and environment. A review of the literature. *Vie et milieu*. Proceedings of the ADLaF colloquium. Laboratoire Arago, Université Pierre et Marie Curie. 75–87.

McFarland, M., J. Sullivan, M. Twardowski, and A. Nayak. 2016. Effects of orientation on light absorption by colonial diatoms. Poster session. Ocean Sciences Meeting. New Orleans, LA USA.

Nayak, A., M. McFarland, M. Twardowski, and J. Sullivan. (in prep). Field observations of preferential particle orientation in undisturbed oceanic flows.

Nayak, A., M. Twardowski, J. Sullivan, M. McFarland, N. Stockley, and S. Nardelli. 2016. A field study of particle orientations in shear flows. Ocean Sciences Meeting, New Orleans, USA.

Pickett-Heaps, J. 1998a. Cell division and morphogenesis of the centric diatom *Chaetoceros decipiens* (Bacillariophyceae) I. living cells. J. Phycol. 34: 989-994.

Pickett-Heaps, J. 1998b. Cell division and morphogenesis of the centric diatom *Chaetoceros decipiens* (Bacillariophyceae) II. electron microscopy and a new paradigm for tip growth. J. Phycol. 34: 995-1004.

Rines, J. 1985. The seasonal distribution and floristic composition of the *Chaetoceros* Ehrenberg (Bacillariophyceae) of Narragansett Bay, Rhode Island. M.S. Thesis, University of Rhode Island.

Rines, J. and P. Hargraves. 1987. The seasonal distribution of the marine diatom genus *Chaetoceros* Ehr. in Narragansett Bay, Rhode Island (1981-1982). Journal of Plankton Research. 9(5): 917-933.

Rines, J. and P. Hargraves. 1988. The *Chaetoceros* Ehrenberg (Bacillariophyceae) flora of Narragansett Bay, Rhode Island, U.S.A. Bibl Phycol 79: 1-196.

Stein, J. 1979. Handbook of phycological methods: culture methods and growth measurements (Vol. 1). Cambridge University Press.

Sullivan, J., E. Swift, P. Donaghay, and J. Rines. 2003. Small-scale turbulence affects the division rate and morphology of two red-tide dinoflagellates. Harmful Algae 2: 183-199.

Key Points:

- High light appears to have produced longer colonies (analyses still in progress)
- Diatom colonies grew shorter over time as cell and colony density increased
- Different developmental life history stages grew at the same rate

Key Index Words:

Diatoms; *Chaetoceros*; light; morphological variation; setae

Effect of Wind on Water Level and Dissolved Oxygen Concentration at Assateague Island National Seashore

Annelise Hill[1,2] and Amanda Babson[3]
[1]Graduate School of Oceanography, University of Rhode Island, Narragansett, RI 02882 USA
[2]Department of Chemistry, Reed College, Portland, OR, USA
[3]Northeast Region, National Park Service, Narragansett, RI 02882, USA
Corresponding author: anhill95@gmail.com

Abstract
Inundation regime is a major determinant of salt marsh vegetation. Chincoteague Bay, adjacent to Assateague Island National Seashore (ASIS), is a micro-tidal system and wind direction has a significant effect on water level. Wind also has a significant effect on dissolved oxygen concentration. Existing data were used from long-term NOAA tide gauge and co-located wind, medium- and short-term National Park Service (NPS) water level gauges, Remote Automated Weather System (RAWS) wind, and dissolved oxygen from NPS Inventory & Monitoring and ASIS sources. Statistical models were developed using RStudio to best estimate water level based on weather at Buntings Bridge and Ocean City, MD. Wind speed and direction were investigated but speed was found not to be significant. The model was then used to estimate the component of water level due to wind direction. Based on the model, wind direction can cause a change in water level of 0.14 m, which is 22.9% of the tidal range. West winds are correlated to the highest water levels whereas east-southeast winds are correlated to the lowest levels, likely due to the shape of the basin. The dominant spring and summer wind is from the south-south west, which also increases water level. A model was developed to estimate the component of dissolved oxygen concentration based on wind. Westerly winds cause a decrease in dissolved oxygen concentration. Wind direction affects dissolved oxygen concentration, limiting organism access to oxygen. Wind direction also affects water level, altering inundation and affecting vegetation zonation, based on species inundation tolerance.

Tides are the primary driver behind salt marsh inundation and nutrient loading is a large determinant of dissolved oxygen concentration. In micro tidal systems (systems with tidal range less than 2 m), winds have the potential to have a significant impact on water level and the subsequent inundation of salt marsh vegetation. Additionally, previous research has shown that wind direction has the potential to affect dissolved oxygen concentration (Scully 2010). In the Chesapeake Bay, southwest winds are correlated to lower dissolved oxygen concentrations (Scully 2010). Climate change is causing sea level rise; these higher sea levels will exacerbate storm impacts and increase the potential for ecosystem changes and property damage. Warmer waters will also decrease dissolved oxygen concentrations and increase hypoxic events (Meire 2013). Atmospheric circulation is being altered in the form of poleward shifts of wind and pressure systems due to anthropogenic greenhouse gas emissions and the depletion of stratospheric ozone (Letcher 2009). Large-scale atmospheric and oceanic circulation is

connected to local climate and, on the Atlantic coast of the United States, this is largely determined by the location of the Bermuda High (Katz 2003). There is evidence that westerly winds are increasing in frequency in recent decades in the mid-latitude North Atlantic due to a weakening of the Bermuda High (Scully 2010).

There are multiple factors that affect water level, including tides, winds, air pressure, precipitation, and the shape of the shoreline. The National Park Service (NPS) has previously researched the impact of tides on water level and subsequent salt marsh inundation at Assateague Island National Seashore (ASIS). We aim to expand this research by focusing on the impacts of wind on water level at ASIS. Due to the micro tidal system of Chincoteague Bay, the tidal range at Buntings Bridge (Figure 1) is 0.61 m. Ocean City (Figure 1) is outside of the bay and has a tidal range of 2.1 m due to the exposure to the ocean. Wind therefore may have a significant impact on water level within Chincoteague Bay relative to tides.

Increased nutrient loading has been linked to an increase in primary productivity and an increase in microbial activity and subsequent depletion of bottom depth dissolved oxygen (Diaz and Rosenberg 2008). Currently at Chincoteague Bay, nutrient monitoring is lacking; eutrophication is estimated based on modeling of bay wide nutrient loading. This modeling is limited by the many non-point sources, which has led to uncertainty in loading amounts (Cole 2005). The modeling is also generalized for the entirety of the Bay and not to specific locations. NPS dissolved oxygen research at ASIS has been done through partners and has not included measurements of nutrients, but it has been assumed that nutrients are a major factor (Kopps and Neckles 2009). We explore winds as an additional factor that may affect bottom dissolved oxygen concentrations.

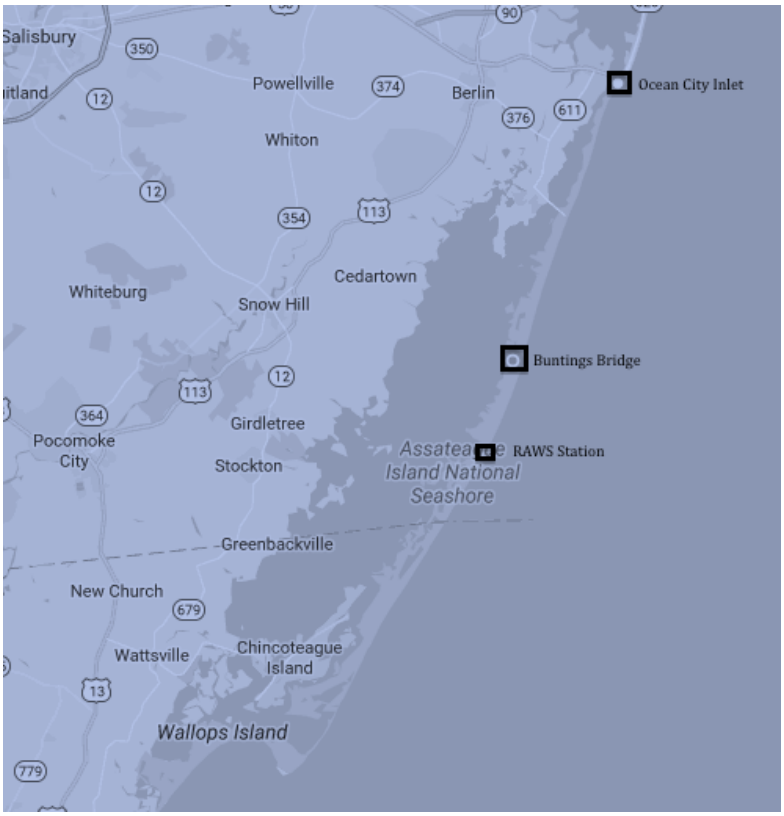

Figure 1. Map of Assateague Island and Chincoteague Bay

We ask two questions 1) what effect does wind currently have on water level relative to tides, and 2) what effect does wind have on dissolved oxygen concentration? Ultimately, we would want to estimate the second question relative to the effect of nutrients, but do not have necessary nutrient data at this time. This research provides a better understanding of how shifts in wind direction would impact salt marsh ecosystems and can help inform the management of these vital ecosystems. We hypothesize that westerly winds will be correlated to higher water levels at Buntings Bridge and lower levels of dissolved oxygen.

Data and Methods

Water Level Data

Water level data were taken from two sources, a long-term NOAA tide gauge at Ocean City Inlet, MD (Figure 1, Station ID 8570283, 38° 19.7' N, 75° 5.5' W) with present installation from 1997 to current date, and a short-term NPS water gauge in partner with NOAA at Buntings Bridge, MD (Figure 1, Station ID 8570691, 38° 8.3' N, 75° 11' W), which was in place from February 8, 2013 – March 5, 2014. At both stations data were collected every 6 minutes; the station included verified water levels and NOAA's astronomical predicted levels based on tidal harmonic analysis (NOS 2007).

Wind Data

Data were used from a long term Remote Automatic Weather Stations (RAWS) in place from 1993 to current date on ASIS (Figure 1). The station is close to Buntings Bridge and is on the coastal side of the island. The station was moved a short distance after Hurricane Sandy, but that did not affect the period of analysis for this study. The station records wind speed and gusts using a three-cup anemometer, wind direction using a wind vane, temperature using a temperature and relative humidity sensor, and accumulated precipitation using a tipping bucket precipitation gauge. All measurements are made hourly.

Global Historical Climatology Network (GHCN) weather data were taken from two locations for dissolved oxygen analysis, Wallops Island, VA (Station ID USW00093739) and Ocean City, MD (Station ID USW00093786).

NOAA wind data, co-located with tide gauge, were used from Ocean City Inlet, MD (Station ID 8570283).

Water Quality Data

Nutrient data were taken from the EPA STORET provider, generated by Horn Point Laboratory Nutrient Analytical Services Lab.

Water quality data were obtained from NPS Inventory and Monitoring. Sampling was done in 2006, 2008, 2010, 2012, and 2014. The 2006-2010 data were certified whereas 2012-2014 were provisional. A tessellated grid of 30 hexagons was used and sampling was done at a random location within each hexagon (Kopp and Neckles 2009). Samples were collected once a week in the months of July and August at the surface (0.001-0.1 m), middle of the water column (0.4 – 2.7 m), and at the bottom, just above the substrate (maximum 4.5 m). Depths vary widely by hex due to the depth of the type of location. Measurements recorded were Kd, which is the attenuation coefficient of downwelling PAR, conductance (millisiemens/cm), temperature (°C), chlorophyll-A (µg/L), and dissolved oxygen (mg/L and % saturation). All years of data were used.

Elevation Data

Elevation data are from University of Rhode Island's Environmental Data Center (Neil and Rasmussen 2014).

Seasonal Prevailing Winds

A filter was used in RStudio version 0.98.1028 to classify winds as one of 12

cardinal wind directions, N, NNE, NE, ENE, E, ESE, SE, SSE, S, SSW, SW, WSW, W, WNW, NW, or NNW. The date of each wind was also classified by season. A histogram was then created for each season charting the frequency of each wind direction. A boxplot of mean wind direction was also created.

Daily Winds

Daily shifts in wind direction were determined in R by first classifying winds by time of day. Time-of-day distinctions were determined by plotting time by direction for 15 days of every season. The times of changes in wind direction were noted. Time of day was classified as night, afternoon, midday, midnight, or morning based on the frequent times of wind shifts. The mean wind direction for every hour of the day was plotted for each season with each hour of observation classified by time of day.

Seasonal and Daily Water Level

RStudio was used to analyze daily and seasonal differences in water level deviations from tidal predictions. The difference between verified and NOAA's tidal predicted water level was taken as an explanatory factor of influences on water level other than tide and a boxplot was created of the differences by seasons. An analysis of variance was conducted of seasons and the difference between verified and predicted water level. The procedure was repeated for time of day.

Wind Direction

The program R was used to analyze wind direction effects on water level differences. The difference between verified and predicted water level was taken and a boxplot was created of the differences by wind direction. An analysis of variance was conducted of wind direction between verified and predicted water level. This was done on a 1-hour and 72-hour timescale of wind direction.

Model Generation

A model was generated in R in order to determine the effect of wind on water level deviations from tidal predictions. In order to generate the model, we looked at the effect of wind direction, wind speed, accumulated rainfall, air temperature as a reflection of season, and wind gusts, on the difference between verified and predicted water level. The impact of each factor was looked at on a 1-, 6-, 24-, and 72-hour timescale. Wind was looked at as an 8-level factor (N, NW, W, SW, S, SE, E, and NE) and as a 12-level factor (N, NNW, NW, WNW, W, WSW, SW, SSW, S, SSE, SE, ESE, E, ENE, NE, and NNE). Assumptions of the test were checked and rainfall was cubed to meet assumptions. A correlation matrix was created and correlations between factors were analyzed. Gusts were excluded because of correlation with speed. Correlations between timescales were analyzed and 6 and 24 hours were excluded due to similarity to 1 and 72 hours. Linear models were fit to each individual factor at each time scale. Each factor was tested singly against water level and factors were excluded if they had a p value > 0.2.

The model with highest predicting power was determined using a stepwise algorithm. Forward and backward directions were run. The models with the lowest Akaike Information Criterion (AIC), a reflection of relative quality of the model, were taken for each run. Interaction terms were added to the resulting models to investigate the predicting power of interactions. The AICs were compared and the final model was selected based on the lowest AIC value. The same procedure was repeated for the Ocean City Inlet, MD data for 2013 and 2014. The wind speed, gusts, and temperature factors were the same but barometer was used instead of rainfall because of differences in available data. Barometer and rainfall are likely both reflections of storms. Wind speed was looked at as an 8-level factor and as a reduced factor

with winds designated as westerly or non-westerly.

Predictions using model

The model was subsequently used to determine the effect of each wind direction on the difference between verified and predicted water level. Coefficient values were plugged in for all terms. The equation was used with a coefficient for each individual wind direction. Temperature and rainfall values were entered for mean, high, and low levels.

Model Generation - Water Quality

A linear mixed model was run in R using the package "nlme" to determine the effect of wind and water quality factors on dissolved oxygen concentration. Wind direction, wind speed, year, turbidity, nitrogen, chlorophyll-A, salinity, and water temperature were examined. The factors were examined on 24-hour, 3-day, and 90-day time scales. The assumptions of the test were checked. The log of dissolved oxygen, turbidity, and chlorophyll and the cube of salinity were taken to meet assumptions of the test. A correlation matrix of continuous variables was created and the data frame was narrowed to exclude one of a correlating variable. The data were reshaped by depth type. Multivariate normality was checked for independent variables. Each main effect was tested singly against dissolved oxygen and were excluded if $p > 0.2$. A likelihood ratio test was performed on the full model and it was determined that a randomly varying intercept best accounted for patterns of changes between hexes. AIC values were used to determine which fixed factors should be included in the final model. All combinations of significant factors were tested and the model with the lowest AIC was selected. A 2-D plot was created holding turbidity constant to determine the effect of wind direction on dissolved oxygen by year.

Salt Marsh Elevation Interpolation

Interpolations were done using ArcMap. Polygons were created around each of 10 clusters of Real Time Kinematic (RTK) elevation points. RTK elevations have an accuracy of 2-4 cm. The outline of the polygon was only as large as the outlying elevation or vegetation points. The elevation points were interpolated using four different techniques. Points-to-Raster conversion was run with cell assignment at mean. Inverse distance weighted (IDW) technique was used with a cell size of 1, checking four points, with a maximum distance of 200 m. Natural neighbor was run. Spline was done with an output cell size of 1 and the number of points set to four. The values of each technique were then extracted to specified vegetation points.

Results

Seasonal Prevailing Winds

The dominant wind for summer (June – August) and spring (March – May) was SSW, with few periods of other wind direction. For winter (December – February), the frequencies of wind direction were widely distributed. The most frequently occurring direction was SSW, but this direction occurred a few instances more frequently than other directions. There were few instances of S, SSE, SE, ESE, E, ENE, NE, and NNE winds. The mean wind direction was SW. For fall (September – November), the frequencies of wind direction were widely distributed. The most frequently occurring direction was NE, but this direction occurred few instances more frequently than other directions. There were few instances of SSE, SE, ESE, E, and ENE winds.

Daily Winds

The mean wind direction for time of day was determined. For 14:00 – 09:00 the mean direction was SSW, for 09:00 – 14:00 the mean was S. The mean direction varied by the hour of observation by up to 60 degrees. The general trend was a direction of a higher

degree at the start of the day, increasing into early morning, decreasing to its lowest point at midday, and increasing through the end of the day.

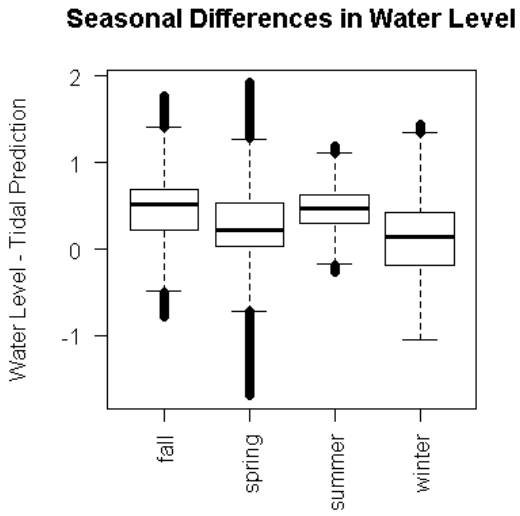

Figure 2. Boxplot of the difference between water level and predicted water level by season.

Seasonal and Daily Water Level

There was a significant difference between water level and tidal prediction during winter and spring, but not during summer and fall (Figure 2). The mean difference for every season was greater than 0, the tidal prediction was commonly lower than the observed water level. There were no differences based on the time of day.

Water Level Model 1

Buntings Bridge, MD water level model

Water Level – Predicted Water Level = Intercept + β_1• 72h Rainfall + β_2•1h direction + β_3•72h direction + β_4•72h temperature + β_5 •(72h temperature × 72h direction)

The models with the highest predicting power were determined (Table 1). The final model was chosen based on the lowest AIC value (Model 1). The factors with the highest predicting power which were included in the final model are 72-hour accumulated rainfall cubed (p value = 0.105), 1-hour wind direction (p value = 0.00030), 72-hour wind direction (p value = 0.00019), 72-hour temperature (p value = 5.86×10^{-11}), and an interaction term between 72-hour temperature and 72-hour wind direction (p value = 0.0123).

Table 1. Best models for predicting the difference between water level and tidal predictions at Buntings Bridge. K is the number of groups. L is the number of levels.

Model	K	AIC	Delta AIC	Cumulative Weight
72h rainfall^3 + direction 12 L + 72h direction 12 L+ 72h temperature + (72h temperature × 72h direction 12 L)	49	-336.68	0.00	0.76
72h direction 12 L + 1 h direction 12 L + 72 h temp + (72h temperature × 72h direction 12 L)	48	-334.17	2.51	0.98
72h direction 12 L + 1 h direction 12 L + 72 h temperature + 72 h rainfall^3	34	-329.66	7.03	1.00
72h direction 12 L + 72h temperature + (72h temperature × 72h direction 12 L)	33	-320.52	16.16	1.00
72 h temperature + 72h direction 12 L + 1 h direction 12 L + 1 h direction 12 L + (72h temperature × 72h rainfall^3)	49	-319.59	17.10	1.00
Intercept	2	-276.98	59.70	1.00

Water Level Model Predictions

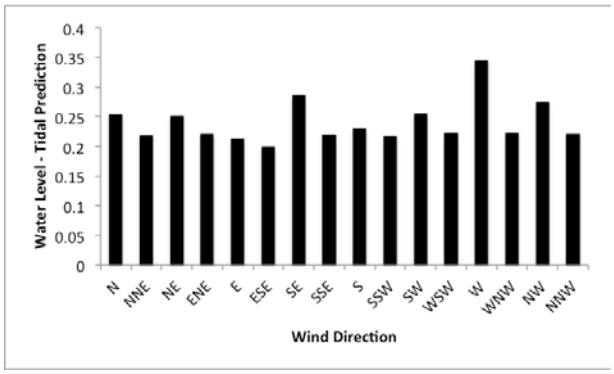

Figure 3. Model prediction of difference between water level and tidal prediction at mean rainfall and mean temperature.

Based on the model, different wind directions on a 1-hour time scale affect water level to different extents (Figure 3). The range of the difference between the wind direction causing the highest and lowest water level is 0.14 m. This is 22.9% of the tidal range at this location. ESE winds are correlated to the lowest water level and west winds are correlated to the highest water level.

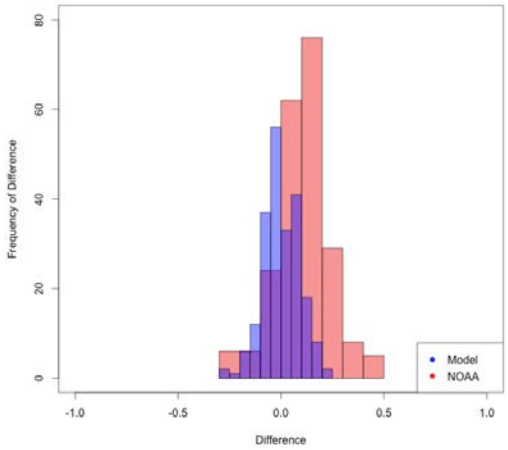

Figure 4. Histogram of difference between water level and tidal prediction for the NOAA tidal prediction model and weather model created.

Water level model compared to NOAA Tidal Prediction – Buntings Bridge, MD

The difference between water level and prediction at Buntings Bridge, MD using NOAA's tidal prediction is typically above zero, the estimate is typically lower than the actual water level (Figure 4). The difference is between -0.25 and 0.5 m. The weather correction model generated is typically at a difference of zero and the range is between -0.25 and 0.25 m.

As seen in Figure 5, extremes in water level are not explained by just tides. The weather model correction predicts water levels closer to the observed values for extreme water levels.

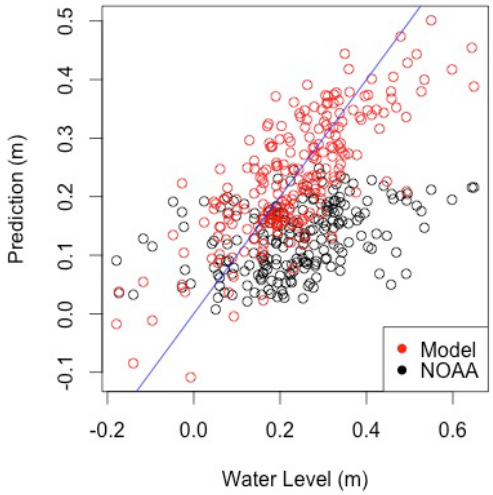

Figure 5. Scatterplot of predicted and verified water level (m) for the NOAA prediction and water level model.

Water level model – Ocean City Inlet, MD

Model 2. Ocean City water level model

Water Level – Predicted Water Level = Intercept + β_1• 1h direction + β_2•1 h barometer + β_3•72h direction + β_4•1h Speed + β_5•Speed^2 + β_6•72h Speed

The results for the Ocean City inlet model were largely comparable to the Buntings Bridge, MD results. The data were taken from a different location, which had differences in available data types and therefore include different terms. The models produced are reported (Table 2) and the model with the lowest AIC was used. The factors with the

highest predicting powers are 8 level 1-hour direction (p value 8.5 x 10^{-14}, 1-hour barometer (p value = 2.2 x 10^{-16}), 8 level 72-hour direction (p value = 3.2 x 10^{-9}, 1-hour speed (p value = 0.05), 1-hour speed squared (p-value = 0.2), and 72-hour speed (p value = 0.1). Unlike at Buntings Bridge, wind speed does contribute to the model, but still the effect of the speed factors are much smaller than the direction factors.

Table 2. Best models for predicting the difference between water level and tidal predictions at Ocean City Inlet.

Model	K	AIC	Delta AIC	Weight
1 h direction 8 L + Barometer 1h + 72 h direction 8 L + Speed 1 h + Speed 1 h sq + Speed 72 h	2	313.99	0.00	1
72 h direction reduced + Barometer 1hr + 1 h direction reduced + Speed 1 h + Speed 1 hr sq	7	351.80	37.81	1
Intercept	2	460.32	146.33	1

The difference between water level and prediction at Ocean City Inlet, MD using NOAA's tidal prediction is typically above zero; the estimate is typically lower than the actual water level (Figure 6). The difference is between -1.5 and 2.5 m. The weather correction model generated is typically at a difference of zero and the range is between -1.5 and 1.5 m.

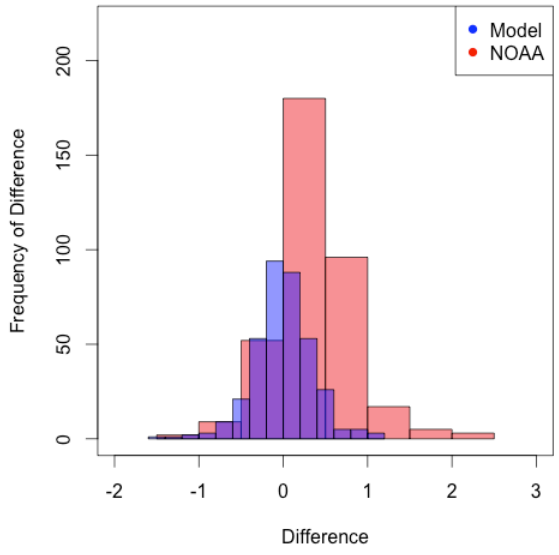

Figure 6. Histogram of difference between water level and tidal prediction for the NOAA tidal prediction model and weather model created at Ocean City Inlet.

Dissolved Oxygen Model

Model 3. Log Bottom Dissolved oxygen

Log Bottom Dissolved Oxygen = Intercept + β_1•Year + β_2•log (turbidity) +β_3• 24 h Wind Direction (west / non west)

Table 3. Dissolved oxygen models with lowest AICs. All models included random term (1|Hex)

Model	K	AIC	Delta AIC	Weight
Year + log Turbidity bottom	5	-1.97	0.00	0.58
Year + log turbidity bottom + 24 h direction west / non west	6	-1.35	0.62	1.00

The model with the highest predicting power (Table 3) that included wind was determined to include year (p = 0.02), turbidity (p = 0.0004), and the reduced wind direction factor (p = 0.0137). A model excluding wind (Table 2) had the highest predicting power but due to the similarity in AIC values and aim to investigate wind, this model was not chosen as the final model. Speed did not have a significant effect on prediction. Based on available models, which are based on limited data, nutrient levels were also not statistically significant.

Wind direction does have a significant effect on bottom dissolved oxygen concentration. Westerly winds are correlated to lower levels in dissolved oxygen (Figure 7).

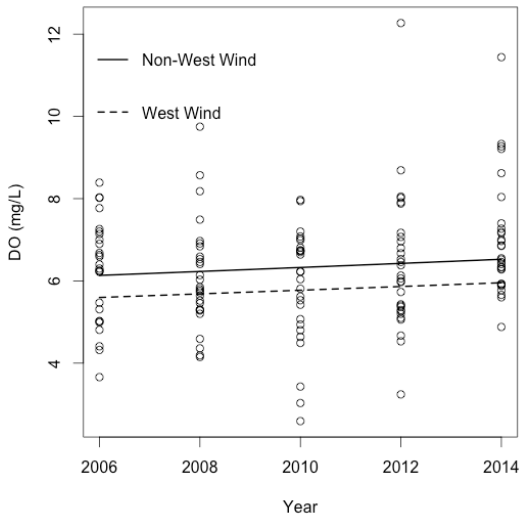

Figure 7. Dissolved oxygen concentration (mg/L) at different years.

Discussion

Water Level

Wind direction does have an effect on the water level in Chincoteague Bay. West winds lead to the highest water level and east-southeast winds are correlated to the lowest water levels, with a model predicted water level difference of 0.14 m between the two wind directions. While the positive difference values that the model predicts suggest that every wind direction leads to water levels higher than predicted, it is likely that other factors have an impact on the height of the water level.

The reason for the variation between water level and predicted water level may be the effect of where wind drives water based on the shape of the bay. Westerly winds would push water from the bay into inlets leading towards Buntings Bridge, likely increasing the water level at the location. Easterly winds may be pushing water out of these inlets and lowering the water level.

With the effect of wind on water level, wind direction is impacting the amount of inundation that salt marshes at ASIS experience. To understand the extent of this inundation and impacts it may have on vegetation, the mapping done in this research should be used as well as information on the elevation inhabited by different vegetation species. The mapping can be used to determine the extent of salt marsh that experiences increased inundation with west winds and the extent should west winds increase. The available vegetation data can be used to determine if the vegetation at the areas at risk are of a species that would be negatively impacted by changes in inundation and if the surrounding marsh is of a height that will allow for vegetation species shifts and migration. This analysis can inform management decisions, such as determining which marsh sites or vegetation species should be prioritized by the NPS for restoration efforts, which can improve the NPS ability to help the salt marsh keep pace with sea level rise.

Dissolved Oxygen

Wind does have a significant impact on bottom dissolved oxygen concentration in Chincoteague Bay. Westerly winds correlate to lower concentrations, which is consistent with Scully (2010) and our hypothesis. The reason for this decrease in dissolved oxygen with westerly winds may be related to turbidity. Westerly winds are correlated to increased bottom turbidity, which may be causing shading that is decreasing submerged aquatic vegetation production of dissolved oxygen.

In order to better understand the influences on dissolved oxygen and the relation of wind to dissolved oxygen, improved nutrient monitoring should be implemented. Nutrients were not statistically significant in this analysis, but this is likely due to the limited data and lack of data co-located with dissolved

oxygen data. The data used were estimates of total nutrient loading to Chincoteague Bay by year. When used in analysis, each estimate was assigned to every dissolved oxygen value for that year; it therefore is understandable that nitrogen would not appear to have a significant effect when it likely does. In order for the best understanding, it would be necessary to sample nutrients at the same times and locations the other measurements are made.

If westerly winds increase in the area with climate change or with shifts in Atlantic Multidecadal Oscillation, it is likely that decreased dissolved oxygen concentrations will be observed. This could have the potential to impact salt marsh ecosystems, including the nekton in Chincoteague Bay. In the future, wind analysis should be included in water quality analysis.

Conclusion

Wind does have a significant effect on water level with westerly winds correlating to the highest water levels: a change in wind direction can change water level by 0.14 m, which is 22.3% of the tidal range. Wind direction affects dissolved oxygen concentration in Chincoteague Bay, westerly winds are correlated to lower levels of dissolved oxygen than non-west winds. Climate change related to changes in prevailing winds could harm salt marsh ecosystems at ASIS through both increased marsh inundation and decreased dissolved oxygen levels.

Acknowledgements. Annelise Hill was supported by a Summer Undergraduate Research Fellowship in Oceanography (SURFO) (National Science Foundation REU grant # OCE-1460819). We are thankful to Margarete Walden for providing guidance on statistical analysis. We acknowledge Dennis Skidds, Brian Sturgis, Andrew Neil, and Scott Rasmussen for providing data.

References

Cole, Luke W. *Nitrogen Loading to Chincoteague Bay (MD, VA): A Reassessment*. Master's thesis, 2005.

Diaz, R. J., and R. Rosenberg. "Spreading Dead Zones and Consequences for Marine Ecosystems." *Science* 321, no. 5891 (2008): 926-29. doi:10.1126/science.1156401.

Katz, Richard W., Marc B. Parlange, and Claudia Tebaldi. "Stochastic Modeling of the Effects of Large-Scale Circulation on Daily Weather in the Southeastern U.S." *Issues in the Impacts of Climate Variability and Change on Agriculture*, 2003, 189-216. doi:10.1007/978-94-017-1984-1_9.

Kopp, B. S., and H. A. Neckles. 2009. A protocol for monitoring estuarine nutrient enrichment in coastal parks of the National Park Service Northeast Region. Natural Resource Report NPS/NCBN/NRR—2009/110. National Park Service, Fort Collins, Colorado.

Letcher, T. M. *Climate Change: Observed Impacts on Planet Earth*. Amsterdam: Elsevier, 2009.

Meire, L., K. E. R. Soetaert, and F. J. R. Meysman. "Impact of Global Change on Coastal Oxygen Dynamics and Risk of Hypoxia." *Biogeosciences* 10, no. 4 (2013): 2633-653. doi:10.5194/bg-10-2633-2013.

Neil A and Rasmussen S. 2014. Assateague Island National Seashore Marsh Elevation Points. Assateague Island National Seashore

NOS. 2003. Computational techniques for tidal datums handbook, NOAA special publication

Scully, Malcolm E. "The Importance of Climate Variability to Wind-Driven Modulation of Hypoxia in Chesapeake Bay." *J. Phys. Oceanogr. Journal of Physical Oceanography* 40, no. 6 (2010): 1435-440. doi:10.1175/2010jpo4321.1.

Key Points:

- Wind direction affects water level at Assateague Island National Seashore (ASIS)

- Wind direction affects dissolved oxygen concentrations in Chincoteague Bay

Key Index Words:
Wind direction; dissolved oxygen; inundation

Nitrogen Cycle Connectivity along the Agulhas Current

Alexandra L. Norwood[1,2] and Rebecca S. Robinson[1]
[1]Graduate School of Oceanography, University of Rhode Island, Narragansett, RI, USA
[2]Arizona State University, Tempe, AZ, USA
Corresponding author: Alexandra.Norwood@asu.edu

Abstract
The nitrogen cycle plays a key role in the biological productivity of the ocean. Phytoplankton growth is limited by the amount of bioavailable nitrogen. The bioavailable nitrogen budget depends on a balance between input through nitrogen fixation and output through denitrification and the budget appears to be balanced on a global scale. The Indian Ocean has a nitrogen deficit that may be created by excess denitrification, whereas the majority of the Atlantic Ocean has a nitrogen surplus due to excess nitrogen fixation. The South Atlantic Ocean has a small nitrogen deficit with an unclear source. The Agulhas Current delivers water from the Indian Ocean to the South Atlantic Ocean through eddies and these eddies may carry nitrogen deficient water into the South Atlantic Ocean from the Indian Ocean, linking the nitrogen cycles of the two oceans. Denitrification imparts an isotopic signature on a water mass, which is ultimately transferred to sediment on the sea floor. Anticipating that the water mass would be the most important source of the isotopic signature in the sediment, we measured ^{15}N to ^{14}N ratios in the bulk sediment through cores from three sites along the Agulhas flow path. The trends in these signals were inconsistent between sites, indicating that N isotope ratio in sediment likely results from a combination of factors for each site. The results do not directly reflect the movement of denitrified water masses from the Indian to South Atlantic Oceans and exemplify the complexity of nitrogen cycle connectivity along the Agulhas Current.

This manuscript intentionally left blank

This manuscript intentionally left blank

This manuscript intentionally left blank

This manuscript intentionally left blank

This manuscript intentionally left blank

This manuscript intentionally left blank

This manuscript intentionally left blank

This manuscript intentionally left blank

This manuscript intentionally left blank

This manuscript intentionally left blank

This manuscript intentionally left blank

This manuscript intentionally left blank

This manuscript intentionally left blank

Zooplankton Biodiversity and Community Composition in Response to Environmental Change in Narragansett Bay

Ariel K. Pezner[1,2], Gang Chen[1], and Tatiana A. Rynearson[1]
[1]Graduate School of Oceanography, University of Rhode Island, Narragansett, RI, USA.
[2]Environmental Science, University of California Los Angeles, Los Angeles, California, USA
Corresponding author: arielpezner@ucla.edu

Abstract
Characterized by their immense biodiversity, zooplankton are essential members of the Narragansett Bay (NB) estuarine system, facilitating bottom-up energy transfer from primary producers and thus supporting fishery production. Over the past decades, NB has been subject to strong impacts of climate change and anthropogenic exploitation. Whether and/or how the zooplankton community has undergone ecological changes in response to the environment remains unknown, but may have serious impacts on productivity and fishery health. Here we examined temporal changes in the composition and abundance of the NB zooplankton community at monthly, seasonal, yearly and decadal time scales, using 72 monthly samples for two sets of three consecutive years (2003–2006 and 2013–2016) from the Narragansett Bay Long-Term Plankton Monitoring program. With a Benchtop Video Plankton Recorder, we recorded and characterized zooplankton community composition and abundance from body size and its frequency distribution. Analyses focused on mesozooplankton (200–2000 μm), which were found to be a dominant size group of the common zooplankton in NB. We identified significant changes in the mesozooplankton community on seasonal and decadal scales, with a strong seasonality in abundance and body size distribution. In addition, abundance and richness of compositional size groups have dramatically decreased, whereas species evenness has slightly increased in the last decade. These changes are significantly associated with a combination of biotic (abundance, species richness, diversity, Chlorophyll *a*) and abiotic factors (surface temperature, salinity). As the environment of NB continues to change over time, it will become increasingly important to the ecosystem as a whole to monitor changes in zooplankton community structure and biodiversity, which play key roles in marine ecosystem resilience, stability, and overall health.

Environmental change has the capacity to dramatically affect not only the physical environment, but also the dynamics of an ecosystem as a whole. While there exists a considerable body of work examining the effects of climate change on terrestrial ecosystems, the effects on marine ecosystems are not well understood (Hoegh-Guldberg and Bruno, 2010). For many ecosystems, both marine and terrestrial, one of the most significant consequences of climate change is the loss of biodiversity (Hooper et al., 2005; Hoegh-Guldberg and Bruno, 2010), the maintenance of which has been known to be critical to the functional dynamics of an ecosystem (Hooper et al., 2005; Balvanera et al., 2006; Stachowicz et al., 2007; Cardinale et al., 2012). For example, biodiversity enhances ecosystem stability, defined as "the ability to withstand recurrent perturbations" (Worm et al., 2006). Marine systems with higher species richness are more stable, and commercially important fish and invertebrates show lower

rates of extinction and collapse over time in these species-rich environments (Worm et al., 2006). High species diversity also promotes faster recovery from perturbations, perhaps due to the ability of predators to switch prey species if necessary, allowing the perturbed prey populations to recover (Worm et al., 2006; Stachowicz et al., 2007). Losses in biodiversity can therefore have significant negative effects on the structural and functional dynamics of ecosystem as a whole (Cardinale et al., 2012).

Narragansett Bay (NB) is among the most productive estuaries in the United States, playing important ecological and socioeconomic roles in surrounding states. For example, commercial fisheries based out of Rhode Island landed more than 34,000 metric tons in 2007, valued at approximately $77 million (RIDEM, 2008). However, the NB estuarine system has been experiencing evident climate change and anthropogenic stressors over the last few decades, including a rise in water temperature of 1.2°C since 1950 (Smith et al., 2010), intermittent hypoxic events (Codiga et al., 2009), and a historical rise and recent fall of nutrient loading (Nixon et al., 2008). These environmental changes, particularly increases in seawater temperature, have reportedly led to system-wide structural changes in NB, including shifts from vertebrate to invertebrate and benthic to pelagic species (Collie et al., 2008), as well as a sharp decline in the abundance of boreal species such as the winter flounder over the past decades (Oviatt et al., 2003). Such evidence of change in large, nektonic species has raised concerns regarding the stability and health of the NB system, prompting us to examine it thoroughly in order to gain a full understanding of environmental impacts on NB and the community response, specifically through the lens of the marine zooplankton community.

Zooplankton are essential members of marine communities, often consisting of a diverse range of marine organisms, from unicellular protozoans, to multi-cellular invertebrates and vertebrate larval fish (Lalli and Parsons, 1997). Within a typical temperate estuary such as NB, zooplankton play a pivotal role in regulating primary production and transferring energy from primary producers to higher-level predators (Valdés et al., 2004; Richardson, 2008). For example, the growth and development of zooplankton predators such as menhaden in NB is highly related to the zooplankton community composition and size distribution within the bay (Durbin and Durbin, 1998). Compared to vertebrate animals, invertebrate-dominated zooplankton are more susceptible to environmentally-induced physiological and community changes due to their short generation times, enormous population sizes, and lack of commercial exploitation by humans (Richardson, 2008). As a result, zooplankton are expected to be useful "beacons of climate change" and the effects of environmental change on an ecosystem may be examined via changes in their community composition, abundance, and diversity (Richardson, 2008).

Specific zooplankton species in Narragansett Bay have already begun to show responses to local environmental change. Phenological shifts of abundance are one of the most conspicuous among the changes occurring in plankton communities, with environmental variation being the main driver (Machas et al., 1998; Sullivan et al., 2001; Edwards and Richardson, 2004; Costello et al., 2006a, b; Sullivan et al., 2007). For example, warmer temperatures are believed to have facilitated a shift in peak occurrence of the ctenophore *Mnemiopsis leidyi* (a planktivore) by approximately 2 months earlier than the previous annual mean (Sullivan et al., 2001) and an earlier spring population increase in the copepod *Acartia hudsonica*, though there were no changes in the appearance or abundance of the copepod

A. tonsa (Sullivan et al., 2007). Although these species-specific shifts have been identified and documented, few studies have examined how the zooplankton community composition as a whole has responded to climate change in NB. Within the community, not all ctenophore or copepod species have appeared to follow the same changing pattern, suggesting species-specific responses may not be assessed additively for a picture of the whole community. Rather, it is evident that community-wide responses may be complicated by complex interactions among species. In NB, the phenological shift of peak ctenophore abundance has led *A. hudsonica* to outnumber *A. tonsa* within copepod communities, and may have unprecedented long-term impacts on the trophic structure of the entire zooplankton community (Sullivan et al., 2007). Thus, it is important to investigate patterns of zooplankton responses at the community level, and gain insights into their underlying processes and mechanisms.

In this study, we sought to identify whether the zooplankton community of NB has changed over time, and if it has, what environmental factors may be driving this change. To attain this goal, we examined historical, preserved zooplankton samples from the Narragansett Bay Long Term Plankton Monitoring Program (NB-LTPMP, http://www.gso.uri.edu/phytoplankton/, August 2016). Instead of using the traditional and time-consuming taxonomy-based approach, we employed a rapid body size-based approach to characterize the zooplankton community. Using a Benchtop Video Plankton Recorder (BVPR), we recorded images of zooplankton individuals in a community sample and retrieved their body sizes through image analysis. Frequency distributions of zooplankton body sizes, equivalent to species composition and abundance, were compared among community samples to search for patterns of zooplankton community change in relation to environmental changes within NB. The ability to process many samples very quickly allows for the exploration of wider temporal trends, as well as the analysis of community-wide changes. By using body size distributions as a proxy for community composition, we are able to view and analyze changes in the zooplankton community over multiple time scales. More importantly, this method is highly promising for potential future use in real-time monitoring of zooplankton community change in response to changing environmental conditions.

Materials and Methods

Zooplankton Samples

We selected 72 zooplankton samples from the Narragansett Bay Long Term Plankton Monitoring Program (NB-LTPMP)'s historical zooplankton record (http://www.gso.uri.edu/phytoplankton/, August 2016), with each sample representing one month from two sets of three consecutive years: September 2003 to August 2006, and September 2013 to August 2016. In order to maintain temporal consistency between sample collection dates, we selected samples collected during the first week of each month (defined as between days 1 and 8), unless otherwise noted. In situ recorded environmental data for the samples (surface temperature in °C, surface salinity in PSU, and surface Chlorophyll *a* in µg/L) were also taken from the NB-LTPMP's historical record. Zooplankton samples were collected weekly from the R/V Cap'n Bert at the Narragansett Bay Station II (41° 34.2' N; 71° 23.4' W). Vertical net tows were taken from 5 m to surface with a ¼-m opening diameter, 64-µm mesh plankton net, filtering a volume of 0.25 m^3 each sample. The majority of samples were preserved in a buffered formalin-seawater solution with a final concentration of 4%, though two samples (September and October 2003) were preserved in 95% ethanol.

BVPR Data Collection and Image Analysis

The Benchtop Video Plankton Recorder (BVPR, SeaScan Inc., Falmouth, MA) takes zooplankton specimens into its circulating flow system and photographs them as they flow past a camera and strobe system. Before beginning data collection, we adjusted and calibrated the BVPR following the manufacturer's manual (SeaScan, Inc., 2012) to ensure the flow rate corresponded to a percent overlap of about 10% between successive image frames. Given slight variation in the percent overlap value as the BVPR was left running, the calibration was performed twice for each BVPR run (before and after). The percent overlap was calculated following the manual and the average of the two values was later used to convert the zooplankton number recorded in the specific run to true abundance by excluding the overlapped portion. To allow the flow to reach equilibrium and maintain a constant rate, the BVPR was turned on and warmed up for 20 min before first calibration and sample processing.

To run a sample through the BVPR, preserved specimens were first washed to remove fixatives (ethanol or formalin). Specifically, specimens were concentrated on a 64-µm mesh filter, washed multiple times using distilled water, and then diluted in 50 mL of freshwater. Each pre-processed sample was carefully added to the sample cone of the BVPR and recording was started immediately after the specimens were introduced and continued until no specimen remained in the sample cone. All the specimens were later recollected in the sample collection funnel using a 64-µm mesh sieve and returned back to the sample's fixative. Samples containing a particularly high load of phytoplankton were either pre-filtered through a 200-µm sieve or were recollected using a 200-µm sieve to prevent filter clogging and overflow into the BVPR system (Table S1).

The recorded data files were individually processed using the BVPR's data processing program and the default configuration settings developed for zooplankton by the NOAA Northeast Fisheries Science Center (Jonathan Hare). Suspected individual zooplankton bodies were automatically recognized from each image frame and extracted as "Regions of Interest" (ROI) TIFF image files. The raw BVPR ROI files were further analyzed to obtain biological data (abundance, body size distribution) for community ecology analysis. The number of ROIs collected from each sample was interpreted as the total recorded number of zooplankton, assuming all the ROIs represent zooplankton individuals. This number was first adjusted for the true number of individuals using the recorded overlap rate for the examined sample (SeaScan, Inc., 2012), and then converted to the field abundance in individuals/m^3 using the filtered volume.

The body size of a zooplankton individual was calculated directly from its ROI image by converting the pixels to distance using the calculated Image Scale Factor (µm/pixel, SeaScan, Inc., 2012). In order to automatically measure the body size of each individual from the ROI file, we developed a MATLAB (MATLAB R2016a, 2016) code to loop through each ROI from a particular sample, convert it to a binary image, identify the "blob" (organism in the image) with the largest area (to ignore the small particles in the background), and measure the longest major axis and the minor axis. We tested this protocol on a variety of known zooplankton groups and species to ensure that this measurement was accurately applied to true zooplankton objects of different sizes and shapes for the majority of images. For the purposes of this study, we use body length as the general measure of body size and defined it as the length of the longest major axis.

To characterize a sampled community, individual body sizes from a sample were

grouped into bins and a frequency distribution was obtained. To determine the appropriate bin size to use, we manually created a library composed of 22 identifiable zooplankton groups (including subgroups when relevant) present from 2003–2006 and calculated average body size and standard deviation for each group based on randomly selected ROI images (up to 200) within each group. An appropriate bin size was used in order to maximally distinguish all known zooplankton groups.

Community Ecology Analysis

Community ecology analysis was conducted using zooplankton body size data obtained from the BVPR, with size bins and frequencies equivalent to species and abundance, respectively. Species composition for each sample was defined as the number of bins (width = 0.1 mm, maximum bin limit = 19.2 mm) from the body size distributions with individuals present.

To assess the temporal change of the zooplankton community, we compared species diversity, total abundance, and size distribution pattern (histograms) among samples at seasonal, annual, and decadal time scales. Four diversity statistics (Species richness [Margalef], Pielou's evenness [J'], Shannon's H [H', log base e], and Simpson's Diversity [1- λ']) were calculated from the zooplankton body size distributions using DIVERSE in PRIMER v6.1.6. (Clarke and Gorley, 2006). The difference in diversity indices and total abundance among samples was statistically tested using the Student's *t*-test. The difference between two size distributions (histograms) was tested using the non-parametric Whitney-Mann U test, against a null hypothesis that the two histograms were sampled from a single community. For all assessments with regards to seasonal patterns, seasons were defined for a northern hemisphere temperate estuary: Fall (September, October, November), Winter (December, January, February), Spring (March, April, May), and Summer (June, July, August).

We analyzed the variation in the key environmental factors (surface temperature, surface salinity, and surface Chlorophyll *a*) over the sampling periods using Principal Component Analysis (PCA) in PRIMER v6.1.6 (Clarke and Gorley, 2006). Ecological correlation between the zooplankton community and the key environmental factors was explored using multiple linear regression methods (Kutner et al., 2004). Full multiple linear regression models were constructed for 2003–2006 and 2013–2016 data sets respectively, with one of two responsive variable (abundance [N] or Shannon's H') against "species" richness (S), Shannon's H' (or abundance), surface seawater temperature (SST in °C), surface seawater salinity (Sal in PSU), and Chlorophyll *a* concentration (Chl *a* in µg/L). The best-fit models were further searched through model selection in both forward and backward directions and selected based on Akaike Information Criteria (AIC) values. The variables selected by the best-fit models would be considered important candidate ecological factors driving the zooplankton community changes. All the statistical analyses were performed using statistical package R (R Core Team, 2015).

Results

Zooplankton Body Size and Frequency Distribution

All 72 samples were run through the BVPR, producing over 42,644 ROIs (Tables S1, S2). The MATLAB code developed for automatic measurement successfully recognized zooplankton of different shapes and calculated three size measures: area, major and minor axis lengths (Figure 1). There was apparent variation in these values for body shape and size for all 22 known zooplankton groups (Figure 2, Table S3). To best reflect the inter-group size differences,

we used 0.1 mm (100 µm) as the bin width to group the size data and construct the body size distribution histograms.

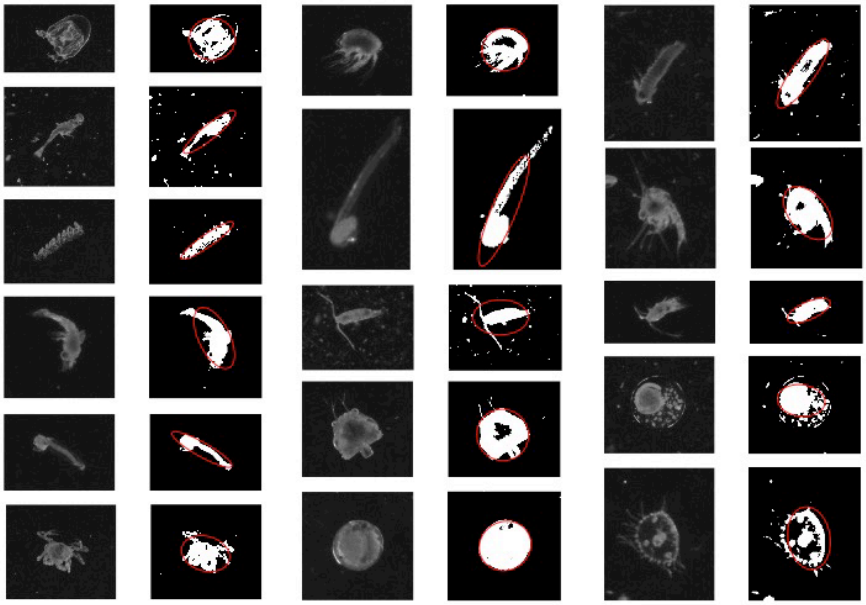

Figure 1. Regions of Interest (ROIs) from various representative zooplankton samples processed through the Benchtop Video Plankton Recorder (BVPR) with the original image on the left, and the post-processed MATLAB binary image on the right. Red ellipses represent body length measured in MATLAB, including the longest major axis and minor axis. Body size was defined as the length of the longest major axis.

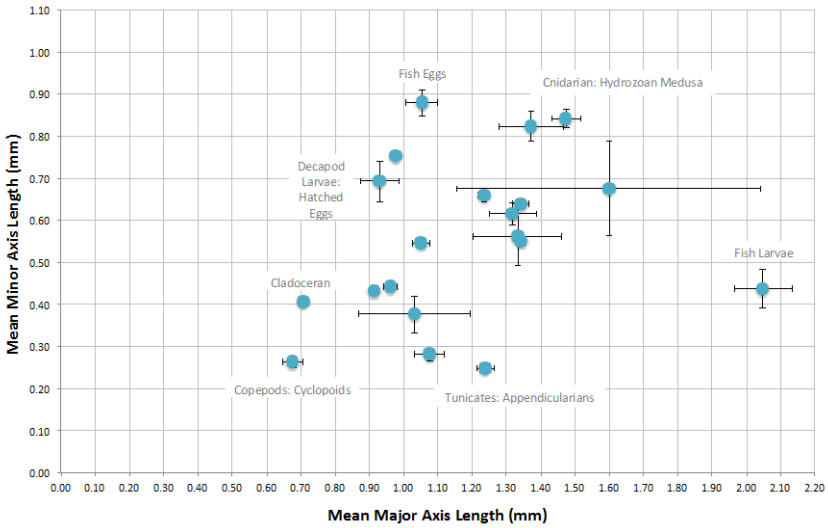

Figure 2. Distribution of the mean body measurements ± SE of the taxonomic groups present in the earlier sample set (2003–2006). Some of the groups are labeled in gray (See Table S3 for a full list of taxonomic groups).

There appeared to be defined seasonal patterns in zooplankton size distributions for all sets of years. The pattern was more visible in the earlier set of years (2003–2006) and especially for mesozooplankton, the dominant

zooplankton size group with a range of 0.2–2.0 mm (Figure 3). Thus, comparison analyses were focused on mesozooplankton, with an upper maximum of 2.0 mm imposed for all plots, though the distributions for all seasons and years spanned a wider range of body sizes (minimum = 0.1 mm, maximum = 19.2 mm). All seasonal distributions were fairly normal, though slightly skewed (Figure 3). Fall appeared to be characterized by evenest distribution of mesozooplankton within the varied size categories, whereas Winter distributions displayed the most limited range in size categories and the lowest average frequencies within each (Figure 3). Spring and Summer distributions were similar in their spread and mean frequencies, though highly variable within the 2003–2006 period (Figure 3). Statistical analysis of these distributions revealed statistically significant differences between the size distributions of both seasons and year sets (decadal scale) (Table 1). The majority of comparisons (8/12) showed significant differences between the seasonal size distributions (Whitney-Mann U test, $p < 0.05$) (Table 1).

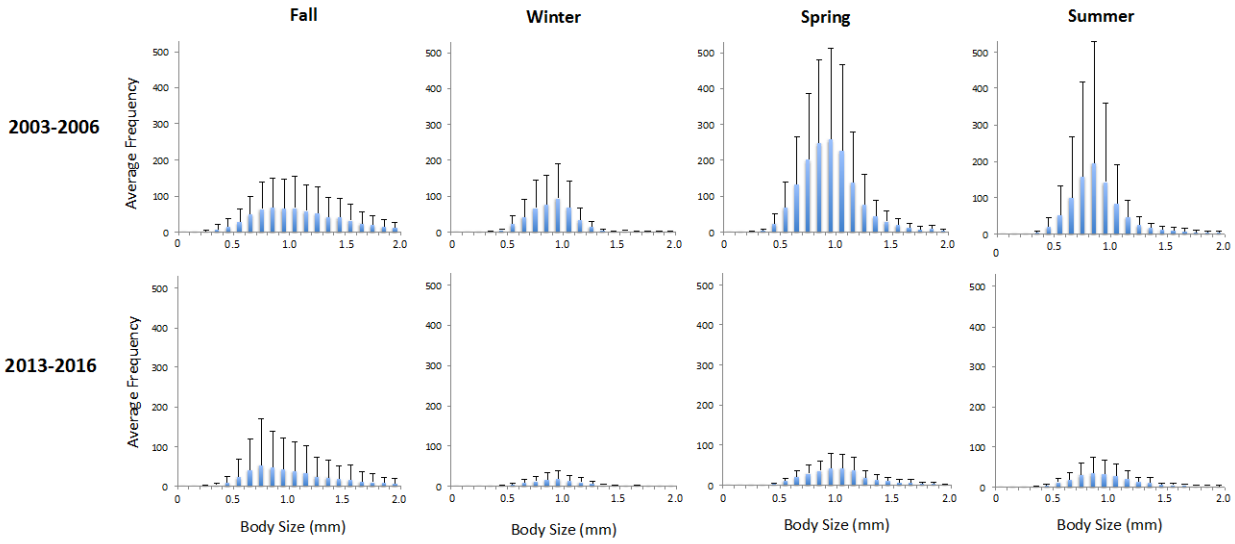

Figure 3. Mean body size distributions + STD of all samples from 2003–2006 (*top row*) and 2013–2016 (*bottom row*) divided by season: Fall, Winter, Spring, and Summer from left to right. Bin width was set to 0.1 mm, and size was limited to 2.0 mm to restrict analyses to the mesozooplankton community only.

Table 1. Whitney-Mann U test results of pairwise differences among seasonal size distributions of zooplankton community in Narragansett Bay. Statistical p-values are listed for each pair of comparison (2003–2006 below shaded diagonal, 2013–2016 above shaded diagonal). Along the shaded diagonal, the same seasons were compared for differences over a decade. Significant values are highlighted in bold and marked with asterisks: $p < 0.05$ *, $p < 0.01$ **, $p < 0.001$ ***.

		2013–2016			
		Fall	Winter	Spring	Summer
2003–2006	Fall	**0.0181***	**0.0000*****	**0.0236***	0.0959
	Winter	**0.0000*****	**0.0002*****	**0.0000*****	**0.0000*****
	Spring	0.1832	**0.0004*****	**0.0010*****	0.4849
	Summer	**0.0051****	**0.0363***	0.1125	0.2268

Temporal Patterns of Abundance and Diversity

We recorded a wide range of average seasonal zooplankton abundance (96–1,534 individual counts in samples, corresponding to 391,357.5–6,253,566.9 individuals/m^3 in the field), and a high level of species diversity (Simpson's index: > 0.88) and evenness (J': >0.71) in seasonal measurements. Overall, average abundance and diversity indices did not vary significantly among seasons of a year, with only a few exceptions, especially in the second year set (2013–2016) (Table 2). However, abundance, species richness, and species evenness differed significantly between the two sets of three years (Table 2, $p < 0.01$). Average seasonal zooplankton abundance decreased up to five-fold between 2003–2006 and 2013–2016 (Table 2). Species richness also appeared to decrease over the last decade, whereas species evenness significantly increased (Table 2). Neither measures of diversity were significantly different between the two sets of years ($p = 0.0612$ and 0.8402 for Shannon's H and Simpson's Index, respectively) (Table 2).

Table 2. Seasonal and decadal changes of zooplankton abundance and diversity in Narragansett Bay. All statistics for a season were averaged over its three monthly samples. Pairwise comparisons among seasons within each year set were conducted using monthly sample-based pairwise *t*-tests, with statistical significance adjusted with the Bonferroni method and labeled in superscript letters. Decadal difference between the two year sets was tested for each statistic using Student's *t*-tests.

Year Set	Time period	Abundance (counts/sample)	Species Richness	Species Evenness	Shannon's H'	Simpson's Diversity
2003–2006	Fall	736.6	**6.3027^{a}**	**0.8253^{a}**	**2.9602^{a}**	**0.9349^{a}**
	Winter	453.7	**3.9300^{b}**	0.7766^{ab}	**2.3926^{bc}**	**0.8843^{b}**
	Spring	1534.9	4.6709^{ab}	**0.7145^{b}**	2.4653^{c}	**0.8880^{bc}**
	Summer	917.6	4.5343^{bc}	0.7812^{ab}	2.5620^{cd}	0.8997^{ab}
	Average (N = 36)	*910.7*	*2.9780*	*0.7745*	*2.5951*	*0.9018*
2013–2016	Fall	452.3	4.1188^{ab}	0.8555	2.4795^{ab}	0.8947
	Winter	96.3	**2.7151^{a}**	0.8817	**2.0823^{a}**	0.8908
	Spring	300.0	3.7642^{ab}	0.8230	2.4515^{ab}	0.8976
	Summer	229.1	**4.5075^{b}**	0.8381	**2.6039^{b}**	0.9140
	Average (N = 36)	*274.6*	*2.2773*	*0.8496*	*2.4143*	*0.8998*
Student's *t*-test: 2003–2006 vs. 2013–2016		p = 0.0012 (one-tailed)	p = 0.0003 (one-tailed)	p < 0.0001 (one-tailed)	p = 0.0612 (two-tailed)	p = 0.8402 (two-tailed)

Environmental Correlation

Environmental factors varied widely and seasonally over both individual years and between the two sets of three years. From 2003–2006, sea surface temperature ranged from −1°C to 23.3°C, surface salinity reached a minimum of 25.6 PSU and a maximum of 31.3 PSU, and surface Chlorophyll *a* ranged from 0.66 µg/L to 20.94 µg/L. Between 2013 and 2016, sea surface temperature reached a minimum of −0.68°C and a maximum of 23.29°C, surface salinity range from 26.05 PSU to 32.15 PSU, and surface Chlorophyll *a* ranged from 0.05 µg/L to 12.28 µg/L.

A principal component analysis separated samples roughly by season (Figure 4a), but best by year set (Figure 4b). Winter and Spring were characterized by lower SST and lower Chlorophyll *a*, whereas Summer and Fall were associated with high Chlorophyll *a* values (Figure 4a). The year sets were most highly separated along the surface salinity axis, where the 2013–2016 samples were

associated with higher surface salinity values than the 2003–2006 samples (Figure 4b).

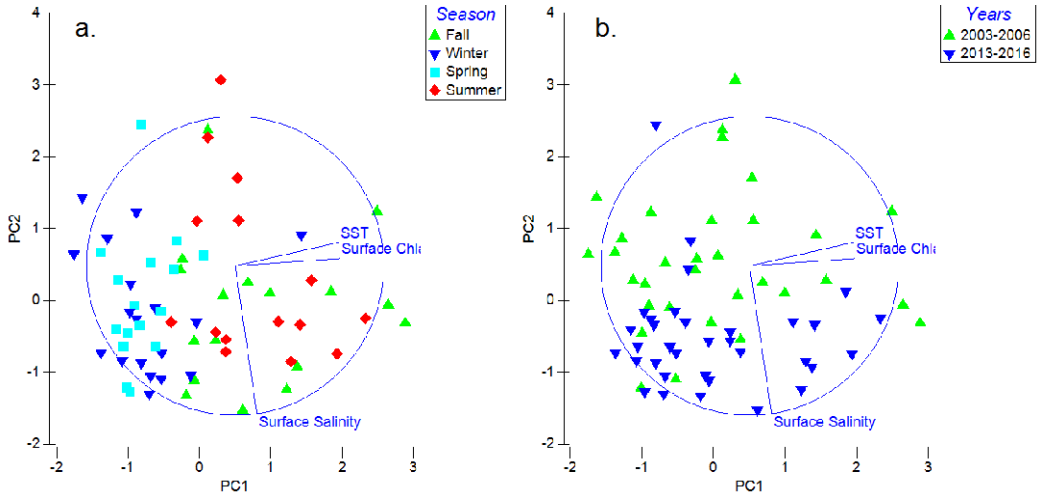

Figure 4. Principal component analysis of the environmental data associated with each sample. Environmental components are sea surface temperature (SST) in °C, surface Chlorophyll *a* in µg/L, and surface salinity in PSU. Samples identified by season [**a**] and year set [**b**].

The mean surface salinity of the 2013–2016 samples was about 2 PSU higher than that of the 2003–2006 samples (Figure 5). Surface Chlorophyll *a* values were highly variable within both sets of years, but overall appeared higher in the 2003–2006 samples than the 2013–2016 samples (Figure 5), much like zooplankton abundance values (Figure 5, bottom panels). Sea surface temperature varied seasonally throughout both sets of years, and in both, a linear trend line revealed increasing SST over both sets of three years (Figure 5, middle panels). Zooplankton diversity (Shannon's H') was also highly variable throughout both sets of years, but did not appear to follow any overall trend (Figure 5, bottom panels).

A multiple regression analysis revealed that for the 2003–2006 samples, variation in zooplankton abundance was best explained by Shannon's H', species richness, salinity, and Chlorophyll *a*, while zooplankton diversity best correlated with abundance, species richness, temperature and Chlorophyll *a* (F-statistic tests: $p < 0.0001$) (Table 3). For the 2013–2016 samples, variation in zooplankton abundance was best explained by Shannon's H', species richness, and Chlorophyll *a*, while abundance, species richness, temperature, salinity, and Chlorophyll *a* best correlated with zooplankton diversity in terms of Shannon's H' (F-statistic tests: $p < 0.0001$) (Table 3). In either case, both abiotic environmental factors (temperature, salinity) and biotic factors (Chlorophyll *a*, species diversity and abundance) appeared to have played a role in driving changes in the zooplankton community in terms of abundance and diversity.

Discussion

The mesozooplankton community of Narragansett Bay has undergone significant changes in body size distribution over both seasonal and decadal scales. Measures of community structure (abundance, species richness, and species evenness) have also changed significantly over the last decade, and these structural changes are related to a combination of biotic and abiotic factors in the Narragansett Bay estuary environment.

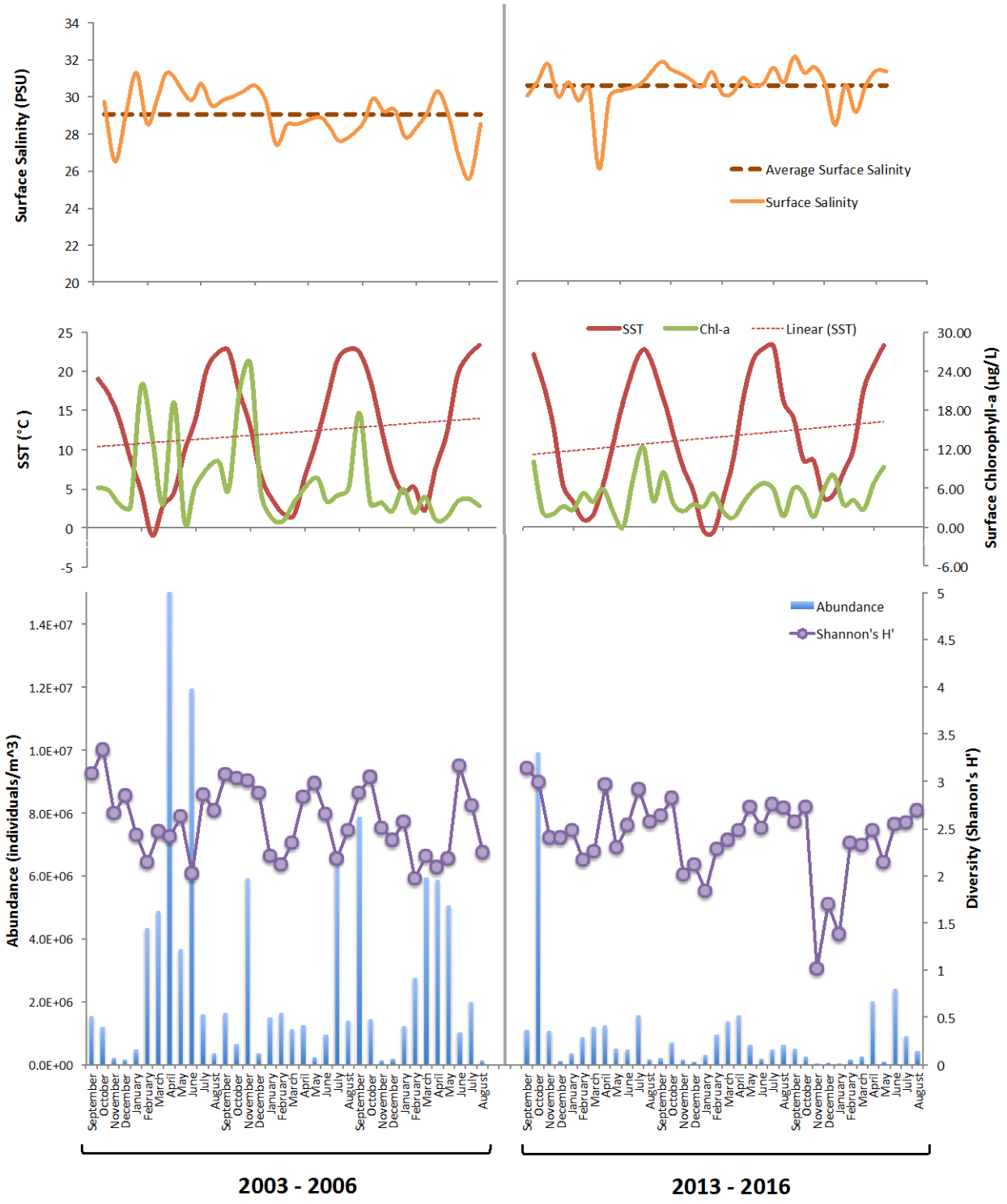

Figure 5. Monthly changes of environmental conditions, including surface salinity (top panel), surface temperature and Chlorophyll *a* (middle panel), and zooplankton abundance and diversity (bottom panel) along consecutive years during 2003–2006 and 2013–2016. Salinities over each set of three years were averaged to show a difference between the two year sets (*top panel*). Linear trend lines for surface temperature were estimated for both sets of three years (*dashed red lines in middle panel*).

Table 3. Environmental associates tested for zooplankton abundance and diversity using multiple linear regression methods. For predictor variables selected by best-fit models, regression coefficients are listed for each model. Statistically significant coefficients (different from zero; *t*-test) are highlighted in bold and significant levels marked with asterisks: <0.05 *, <0.01 **, <0.001 ***. Adjusted correlation coefficient R^2 showing the overall magnitude of modeled correlations and results of *F*-tests testing if a model is statistically significant are listed for each model.

	Responsive variables			
	2003–2006		2013–2016	
Predictor variables	N	H’	N	H’
Abundance (N)		**-0.0002*** **		**-0.0003***
Shannon’s H’	**-2844.35*** **		**-458.89***	
Species richness (S)	**88.79*** **	**0.025*** **	**48.13*** **	**0.0373*** **
Temperature (SST)		**0.0093***		0.0098
Salinity (Sal)	107.45			**-0.0905***
Chlorophyll *a*	**53.21***	**0.0146***	-32.66	
Intercept	2163.03	**1.812*** **	551.87	**4.3838****
Adjusted R^2	0.6922	0.8163	0.5721	0.6914
F-statistic test (p-value)	**<0.0001*** **	**<0.0001*** **	**<0.0001*** **	**<0.0001*** **

The significant seasonal differences in body size distributions within both three-year periods indicate that the zooplankton community experiences seasonal shifts in composition and abundance (Table 1). The common seasonal pattern appears to be characterized by large peaks in abundance in Spring and Summer, a smaller secondary peak in the Fall, and a sharp decline in abundance during the Winter (Figure 3) This pattern may be best interpreted as a response to the phytoplankton blooms in NB. Typical temperate marine ecosystems such as NB are generally expected to feature strong Winter-Spring phytoplankton blooms, followed by a smaller and less intense Fall bloom (Cushing, 1959). Given that zooplankton abundance peaks are expected to be temporally delayed compared to the phytoplankton blooms, we would expect peaks in zooplankton during the Spring and Summer months following a Winter-Spring phytoplankton bloom, as shown in the current study (Figure 3). Establishing this consistent pattern will be useful in tracking changes in the pattern over time in NB, and may help to identify future phenological shifts in the mesozooplankton community.

The significant differences between the two sets of years (2003–2006 and 2013–2016, Table 1) demonstrate that in addition to the distinct seasonal patterns, there has been a major shift in mesozooplankton community composition and abundance over the last decade. In the earlier years, 2003–2006, peak zooplankton abundance occurred strongly in the Spring and Summer, with a smaller peak in the Fall (Figure 3). However, the later set of years (2013–2016) showed overall lower abundances of mesozooplankton and a stronger peak in Fall compared to other seasons (Figure 3). Previous studies on phytoplankton in NB have identified a phenological shift and reduction in bloom magnitude over the last few decades, including a now less-dominant Winter-Spring bloom and a shorter, less intense Summer-Fall bloom (Fulweiler and Nixon, 2009; Nixon et al., 2009). This, in turn, appears to have affected organisms inhabiting higher trophic

levels, including zooplankton, and may help to explain the reduction in the magnitude of the mesozooplankton blooms in NB over the last decade. The cause of these changes is not certain, though there is evidence to support that warming trends and climate variability may be responsible (Fulweiler and Nixon, 2009). Phenology is often sensitive to even slight changes in local environmental conditions, and therefore phenological shifts may be effective signals of climate change (Edwards and Richardson, 2004). Tracking these changes over time in both the phytoplankton and zooplankton communities in NB will be important for monitoring ecosystem productivity and health, particularly considering the possible consequences of these changes for commercially important predators in higher trophic levels.

In terms of the measures of biodiversity, we found that abundance, species richness, and species evenness all differed significantly between the two sets of years, supporting that the zooplankton community has undergone changes in the last decade. Both abundance and species richness have declined in the last 10 years, whereas species evenness has increased (Table 2). The measures of diversity (Shannon's H' and Simpson's Diversity) declined in general over a decade (2.5951 *vs.* 2.4143 for H', and 0.9018 *vs.* 0.8998 for Simpson's), though not statistically significant ($p > 0.05$, Table 2). The significant changes of the community structure (abundance, richness, and evenness) may have potential impacts on trophic functions of the zooplankton community as well as the entire ecosystem, which can only be addressed by resolving composition and abundance of true biological species rather than size bins. The lack of statistical significance of overall biodiversity change over the last decade is likely due to its relatively small magnitude masked by its drastic seasonal variations. Either a lack of change or insignificant change in diversity measures may suggest that the mesozooplankton community is sufficiently diverse to help maintain ecosystem stability (Worm et al., 2006)—an intriguing hypothesis that should be specifically tested in future studies using true taxonomic species data.

The results of our linear models reveal that for each set of years, both biotic and abiotic factors influence abundance and diversity. However, which factors significantly predicted these measures depended on the year set and the specific measure. In all models, biotic factors including species richness, abundance, and diversity were significant (Table 3). The main environmental variables, however, were not consistently significant drivers of abundance or diversity across the sets of years. Surface Chlorophyll *a* was perhaps the most dominant environmental factor, associated with abundance and diversity for the 2003-2006 samples, but only with abundance in 2013-2016 (Table 3). This relationship is unsurprising given the reliance of zooplankton on phytoplankton prey, and it is reasonable to expect a tie between the significant decrease in zooplankton abundance and the seemingly decreasing trend in Chlorophyll *a* values in the last decade (Figure 5). Previous studies have also observed decreasing Chlorophyll *a* values in NB, with a 2009 study finding a near 70% decrease in mean annual water column Chlorophyll *a* concentrations since 1970 (Fulweiler and Nixon, 2009), attributed to the loss of the strong Winter-Spring bloom in phytoplankton (Nixon et al., 2008). Overall, however, it appears that biotic factors more strongly drive changes in zooplankton abundance and diversity in NB. This suggests that the zooplankton community as a whole may be more resistant to environmental change than biotic changes, though these factors are undoubtedly interrelated. With further analyses of specific species, these findings will also contribute to existing literature tracking phenological shifts in plankton

communities, with environmental variation as the main driver of these changes (Mackas et al., 1998; Edwards and Richardson, 2004; Costello et al., 2006a).

The use of a BVPR to process zooplankton samples has proved effective and advantageous over traditional species identification methods and abundance counts using microscopy. Other studies have used Video Plankton Recorders to track changes in individual plankton species (e.g., Olson et al., 2015), but to our knowledge no previous studies have used a BVPR to analyze temporal changes in zooplankton community structure. The patterns and conclusions obtained from size distribution data could be highly valuable for the formulation of hypotheses on ecological processes and mechanisms underlying zooplankton community changes, which will be further tested through species-based community ecological analysis.

Conclusions

The measurement of body length distributions is an effective way to assess changes in zooplankton community composition over multiple time scales. Driven by both biological and abiotic (environmental) factors, the mesozooplankton community of Narragansett Bay has undergone significant changes over seasonal, yearly, and decadal scales, with abundance and species richness dramatically decreasing, and species evenness slightly increasing in the last decade.

Acknowledgments. We thank Jon Hare at NOAA NEFSC for providing the BVPR and all of its associated computers and for his instrumental role in getting the machines to work properly, Stephanie Anderson for her assistance in accessing the historical zooplankton samples and environmental data, Mary Kane for her assistance with writing the MATLAB scripts, and the other members of the Rynearson Lab for their support and feedback on the project along the way. AKP was supported by a Summer Undergraduate Research Fellowship in Oceanography (SURFO) (National Science Foundation REU grant # OCE-1460819).

References

Balvanera, P., A.B. Pfisterer, N. Buchmann, J.-S. He, T. Nakashizuka, D. Raffaelli, and B. Schmid. 2006. Quantifying the evidence for biodiversity effects on ecosystem functioning and services. Ecol. Lett. 9:1146–1156, doi:10.1111/j.1461-0248.2006.00963.x

Beaugrand, G., and R.R. Kirby. 2010. Climate, plankton and cod. Global Change Biol. 16:1268–1280, doi:10.1111/j.1365-2486.2009.02063.x

SeaScan, Inc. 2012. Benchtop video plankton recorder owner's manual. SeaScan, Inc. Falmouth, Massachusetts.

Cardinale, B.J., J.E. Duffy, A. Gonzalez, D.U. Hooper, C. Perrings, P. Venail, A. Narwani, G.M. Mace, D. Tilman, D.A. Wardle, A.P. Kinzig, G.C. Daily, M. Loreau, J.B. Grace, A. Larigauderie, D.S. Srivastava, and S. Naeem. 2012. Biodiversity loss and its impact on humanity. Nature. 486:59–67, doi:10.1038/nature11148

Clarke, K.R., and R.N. Gorley. 2006. PRIMER v6: User Manual/Tutorial. PRIMER-E, Plymouth.

Codiga, D.L., H.E. Stoffel, C.F. Deacutis, S. Kiernan, C.A. Oviatt. 2009. Narragansett Bay hypoxic event characteristics based on fixed-site monitoring network time series: Intermittency, geographic distribution, spatial synchronicity, and interannual variability. Estuaries Coasts. 32:621–641, doi:10.1007/s12237-009-9165-9

Collie, J.S., A.D. Wood, and H.P. Jeffries. 2008. Long-term shifts in the species composition of a coastal fish community. Can. J. Fish. Aquat. Sci. 65:1352–1365, doi:10.1139/F08-048

Costello, J.H., B.K. Sullivan, and D.J. Gifford. 2006a. A physical–biological interaction underlying variable phenological responses

to climate change by coastal zooplankton. J. Plankton Res. 28:1099–1105, doi:10.1093/plankt/fbl042

Costello, J.H., B.K. Sullivan, D.J. Gifford, D. Van Keuren, and L.J. Sullivan. 2006b. Seasonal refugia, shoreward thermal amplification, and metapopulation dynamics of the ctenophore *Mnemiopsis leidyi* in Narragansett Bay, Rhode Island. Limnol. Oceanogr. 51:1819-1831, doi:10.4319/lo.2006.51.4.1819

Cushing, D. H. 1959. The seasonal variation in oceanic production as a problem in population dynamics. J. Cons. Exp. Mer. 24: 455–464, doi: 10.1093/icesjms/24.3.455

Durant, J.M., D.O. Hjermann, G. Ottersen, and N.C. Stenseth. 2007. Climate and the match or mismatch between predator requirements and resource availability. Clim. Res. 33:271–283, doi:10.3354/cr033271

Durbin, A.G., and E.G. Durbin. 1998. Effects of menhaden predation of plankton populations in Narragansett Bay, Rhode Island. Estuaries. 21:449-465, doi:10.2307/1352843

Edwards, M., and A.J. Richardson. 2004. Impact of climate change on marine pelagic phenology and trophic mismatch. Nature. 430:881–884, doi:10.1038/nature02808

Fulweiler, R.W., S.W. Nixon. 2009. Responses of benthic–pelagic coupling to climate change in a temperate estuary. Hydrobiologia. 629:147–156, doi:10.1007/s10750-009-9766-0

Hoegh-Guldberg, O., J.F. Bruno. 2010. The impact of climate change on the world's marine ecosystems. Science. 328:1523–1528, doi:10.1126/science.1189930

Hooper, D.U., F.S. Chapin, J.J. Ewel, A. Hector, P. Inchausti, S. Lavorel, J.H. Lawton, D.M. Lodge, M. Loreau, S. Naeem, B. Schmid, H. Setälä, A.J. Symstad, J. Vandermeer, and D.A. Wardle. 2005. Effects of biodiversity on ecosystem functioning: A consensus of current knowledge. Ecol. Monogr. 75:3–35, doi:10.1890/04-0922

Kutner, M. H., C.J. Nachtsheim, and J. Neter. 2004. Applied linear regression models, 4th ed. McGraw-Hill/Irwin, New York, NY.

Lalli, C. and T.R. Parsons. 1997. Biological oceanography: An introduction. Elsevier Butterworth-Heinemann, Burlington, MA.

Mackas, D.L., R. Goldblatt, and A.G. Lewis. 1998. Interdecadal variation in developmental timing of *Neocalanus plumchrus* populations at Ocean Station P in the subarctic North Pacific. Can. J. Fish. Aquat. Sci. 55:1878–1893, doi:10.1139/f98-080

MATLAB r2016a. 2016. The MathWorks, Inc., Natick, Massachusetts, United States.

Nixon, S.W., B.A. Buckley, S.L. Granger, L.A. Harris, A.J. Oczkowski, R.W. Fulweiler, and L.W. Cole. 2008. Nitrogen and phosphorus inputs to Narragansett Bay: Past, present, and future, p. 101–175. In: A. Desbonnet and B.A. Costa-Pierce [eds.], Science for ecosystem-based management. Springer.

Nixon, S.W., R.W. Fulweiler, B.A. Buckley, S.L. Granger, B.L. Nowicki, and K.M. Henry. 2009. The impact of changing climate on phenology, productivity, and benthic–pelagic coupling in Narragansett Bay. Estuarine, Coastal Shelf Sci. 82:1–18, doi:10.1016/j.ecss.2008.12.016

Olson, E.M., D.J. McGillicuddy, S.T. Dyhrman, J.B. Waterbury, C.S. Davis, and A.R. Solow. 2015. The depth-distribution of nitrogen fixation by Trichodesmium spp. colonies in the tropical–subtropical North Atlantic. Deep Sea Res. Pt. I. 104:72-91, doi:10.1016/j.dsr.2015.06.012

Oviatt, C., S. Olsen, M. Andrews, J. Collie, T. Lynch, and K. Raposa. 2003. A century of fishing and fish fluctuations in Narragansett Bay. Rev. Fish. Sci.11:221–242, doi:10.1080/10641260390244413

R Core Team. 2015. R: A language and environment for statistical computing. R

Foundation for Statistical Computing, Vienna, Austria. https://www.R-project.org/.
Richardson, A.J. 2008. In hot water: Zooplankton and climate change. ICES J. Mar. Sci. 65:279–295, doi:10.1093/icesjms/fsn028
RIDEM. 2008. Rhode Island Marine Fisheries Stock Status and Management. Rhode Island Department of Environmental Management, Division of Fish and Wildlife, Marine Fisheries Section, Jamestown, Rhode Island.
Shin, Y.-J., M.-J. Rochet, S. Jennings, J.G. Field, H. Gislason. 2005. Using size-based indicators to evaluate the ecosystem effects of fishing. ICES J. Mar. Sci. 62:384–396, doi:10.1016/j.icesjms.2005.01.004
Smith, L.M., S. Whitehouse, C.A. Oviatt. 2010. Impacts of climate change on Narragansett Bay. Northeast. Nat. 17:77–90, doi:10.1656/045.017.0106
Stachowicz, J.J., J.F. Bruno, and J.E. Duffy. 2007. Understanding the effects of marine biodiversity on communities and ecosystems. Annu. Rev. Ecol. Evol. Syst. 38:739-766, doi:10.1146/annurev.ecolsys.38.091206.095659
Sullivan, B.K., D.V. Keuren, and M. Clancy. 2001. Timing and size of blooms of the ctenophore *Mnemiopsis leidyi* in relation to temperature in Narragansett Bay, RI. Hydrobiologia. 451:113–120, doi:10.1023/A:1011848327684
Sullivan, B.K., J.H. Costello, and D. Van Keuren. 2007. Seasonality of the copepods *Acartia hudsonica* and *Acartia tonsa* in Narragansett Bay, RI, USA during a period of climate change. Estuarine, Coastal Shelf Sci. 73:259–267, doi:10.1016/j.ecss.2007.01.018
Valdés, L., R. Harris, T. Ikeda, S. McKinnell, and W.T. Peterson. 2004. The role of zooplankton in global ecosystem dynamics: Comparative studies from the world oceans. ICES J. Mar. Sci. 61:441–444, doi:10.1016/j.icesjms.2004.03.001
Worm, B., E.B. Barbier, N. Beaumont, J.E. Duffy, C. Folke, B.S. Halpern, J.B.C. Jackson, H.K. Lotze, F. Micheli, S.R. Palumbi, E. Sala, K.A. Selkoe, J.J. Stachowicz, and R.Watson. 2006. Impacts of biodiversity loss on ocean ecosystem services. Science. 314:787–790, doi:10.1126/science.1132294

Key Points

- The mesozooplankton community has exhibited significant seasonal shifts.
- Abundance, species richness and evenness have changed significantly in the last decade.
- Both biotic and abiotic factors may have driven changes in abundance and diversity.

Key Index Words

Zooplankton; Biodiversity; Climate Change; Community; Narragansett Bay

Note: Supplementary tables S1 and S2 not included in this report.

Sex-Specific Population Dynamics and Trophic Ecology of the Summer Flounder (*Paralichthys dentatus*) in Narragansett Bay, Rhode Island

Adena J. Schonfeld[1,2,3], Joseph A. Langan[1], Corinne L. Truesdale[1], M. Conor McManus[1,2], Jeremy S. Collie[1]
[1]Graduate School of Oceanography, University of Rhode Island, Narragansett, RI
[2]Rhode Island Department of Environmental Management, Marine Fisheries, Jamestown, RI
[3]Marine Science/Biology Program, University of Miami, Miami, FL
Corresponding author: a.schonfeld@umiami.edu

Abstract
Summer flounder, *Paralichthys dentatus*, is an aggressive predator and the most commercially-important finfish in Rhode Island. Accordingly, a long-term increase in abundance documented in Narragansett Bay may prove both economically beneficial and detrimental to resident fish populations. In addition to ecological concerns, management of summer flounder is complicated by sexual dimorphism; females grow larger and faster than males. This dimorphism, when coupled with previous evidence of spatial sex-segregation, increases the risk of disproportionate removal of females via fishing. Specimens were collected on the University of Rhode Island weekly fish trawl and Rhode Island Department of Environmental Management monthly fish survey to determine the role of summer flounder in the local ecosystem and elucidate the nearshore sex-driven population dynamics. Individuals were dissected and sexed based on visual inspection of the gonads. The stomach was then removed and classified as full or empty, and its contents identified to the lowest taxonomic level and weighed. Crangon shrimp (*Crangon septemspinosa*), squid (*Doryteuthis pealeii*), and scup (*Stenotomus chrysops*) were important components in the summer flounder diet. As total length increased, the probability that an individual was female also increased; of the 65 fish collected that were legal for recreational harvest, 63 were female. Additionally, a higher percentage of females was found in shallow inshore waters than deeper offshore areas. These results suggest that implementing a slot-trophy limit on the recreational fishery and restricting inshore commercial harvest would account for the sex-based population dynamics and better protect the spawning stock biomass from future overexploitation.

Significant increases in sea surface temperature and sea level due to climate change are occurring throughout the world's oceans. These impacts are particularly significant in the North Atlantic, where surface water temperatures are increasing at more than twice the rate of the global average (Levitus et al., 2005; Smith et al., 2010). From 1959-2016 the average winter-spring surface temperature in Narragansett Bay, Rhode Island has increased by approximately 2°C (Collie et al., 2008; Collie, 2016). Shifts in species distribution and composition in response to climate change have been well documented (Bell et al., 2014b; Collie et al., 2008; Murawski 1993). The mean temperature preference – defined as the midpoint of the range of acceptable temperatures of each species weighted by the mean abundance – of Narragansett Bay organisms increased by 2°C from 1959-2005, resulting in seasonal migrants superseding resident species (Collie et al., 2008).

One such dominant seasonal species is summer flounder, *Paralichthys dentatus*, which exhibits annual inshore-offshore seasonal migrations, migrating inshore as the water temperatures increase in the spring/summer and returning offshore in the fall (Murawski 1993; Wuenschel et al., 2013). Summer flounder are the most profitable finfish in the state of Rhode Island, with over 2 million pounds of landings worth over 7 million dollars in 2014 (National Marine Fisheries Service, 2016). Although fishing pressure in the 1980s caused the summer flounder population to decline, implementation of stricter regulations in the 1990's has since allowed the population to recover and increase (Bell et al., 2014a; Bell et al., 2014b). While summer flounder have always been common in Narragansett Bay (Collie et al., 2008), the attenuation of harvest pressure and lengthening residence times linked to rising temperatures have resulted in an all-time high abundance that necessitates further understanding of their role in the local ecosystem by fishery managers. In order to elucidate these potential impacts, the diet of summer flounder in nearshore Rhode Island waters needs to be characterized to identify resident species that they frequently predate.

Further, as the abundance of summer flounder increases, so will the incentive to increase fishing pressure. However, this species exhibits several sex-based population characteristics that may complicate management of the fishery. Summer flounder are sexually dimorphic; the females grow larger and faster, with sexual differentiation beginning at 6-12 cm (King et al., 2001). In addition, males have a higher natural mortality rate than females (Maunder and Wong, 2011). Moreover, a study conducted by Morson et al. (2012) found that there was a significant relationship between the sex ratio and the port at which summer flounder were collected, suggesting the potential for spatial sexual segregation. Together, these findings suggest there is a significant risk of disproportionate removal of female spawning stock biomass through fishing. Such concerns were validated in New Jersey in 2009 and 2010, as the recreational catch was predominantly female (Morson et al., 2012). These characteristics therefore suggest that to properly manage the summer flounder population in Narragansett Bay, the sex-based population dynamics of the local stock also need to be studied.

For a species that is so commercially important all along the east coast (National Marine Fisheries Service, 2016), there is a paucity of information on its sex-specific population dynamics. For example, it is not known whether the male summer flounder migrate inshore later than the females, thereby shifting the sex ratios of the inshore population throughout the season. Additionally, studies have not been conducted to evaluate the theory that females eat more often than males, and thus are more vulnerable to the recreational hook-and-line fishery, skewing the data used in the stock assessment (Morson et al., 2012; Northeast Fisheries Science Center, 2013). Finally because federal trawl surveys are conducted far offshore, the sex composition of the nearshore population remains an enigma (Northeast Fisheries Science Center, 2013). The present study aims to use continuous trawl surveys in Rhode Island waters to better inform management in these specific areas of uncertainty.

Materials and Methods

Data Collection

Summer flounder were collected from the University of Rhode Island Graduate School of Oceanography (URI GSO) fish trawl survey conducted in Narragansett Bay, Rhode Island as soon as they began their inshore migration and appeared in the catch in April 2016. The URI GSO fish trawl is conducted on the R/V *Cap'n Bert* and samples at two locations in Narragansett Bay: Fox Island, a mid-bay habitat with a depth of about 7 m,

and Whale Rock, an outer-bay location with a depth of about 22.9 m. Each trawl covers one nautical mile by towing for 30 minutes at a speed of two knots. The otter trawl net has 5.1 cm mesh and an effective opening of 6.5 m (Collie et al. 2008). All of the summer flounder were retained for further sampling.

To gain better spatial resolution, specimens were also collected from the Rhode Island Department of Environmental Management (DEM) monthly fish trawl on the R/V *John H. Chafee*. DEM samples at 13 set locations throughout the bay each month. The net has a 6.71 m wingspan and is in the water for 20 minutes traveling at 2.5 knots. Although DEM sampled several flounder from each survey for their own data collection, all data were shared with the investigators of this project and the excess summer flounder were donated to this study (Olszewski, 2016).

Summer flounder (N=218) were most often dissected immediately after the trawl, but in several instances the fish were first frozen. Other studies (Morson et al, 2012) found that freezing the fish had a negligible impact on the total length of the specimen. The fresh samples and the thawed samples, therefore, were aggregated for data analysis. It was assumed that the freeze-thaw cycle also had minimal impact on the stomach contents. The total length of each individual was measured, prior to dissection to determine the sex by visual inspection of the gonads. The stomach was then excised, opened, and classified as "full" or "empty" depending on the presence or absence of contents. Because some summer flounder were observed regurgitating stomach contents on the boat, individuals that appeared to have flaccid stomachs were also noted. The contents were then visually identified to the lowest possible taxonomic level and weighed.

Data Analysis

The trawl locations were characterized as "inshore" or "offshore" based on a number of physical factors including water depth (inshore generally less than 10 m and offshore greater than 10 m), temperature (inshore with warmer temperatures) and isolation from coastal circulation (inshore more protected) (Figure 1). A logistic regression was used to identify predictor variables, such as temperature, month and location, correlated to the sex of the fish captured. The function used to determine the probability of an inshore fish being male for a given size is given by equation 1, the function for an offshore fish is given by equation 2 and the function for all males in this study is given by equation 3. In these equations, p(M) is the probability of an individual being male and TL is the total length of the individual. The probability of being female is the complement of the probability of being male.

$$p(M) = \frac{e^{9.67538 - 0.26174 \times TL}}{1 + e^{9.67538 - 0.26174 \times TL}} \quad (1)$$

$$p(M) = \frac{e^{10.05889 - 0.25288 \times TL}}{1 + e^{10.05889 - 0.25288 \times TL}} \quad (2)$$

$$p(M) = \frac{e^{7.84318 - 0.20925 \times TL}}{1 + e^{7.84318 - 0.20925 \times TL}} \quad (3)$$

When determining the proportion of fish with full stomachs, the empty stomachs marked as flaccid were removed in order to correct for potential bias introduced by regurgitation. Stomachs which had contents but were noted as flaccid were considered as "full" stomachs in this analysis. To conduct a diet analysis, all of the fish were classified based on categorical variables, such as size class or habitat, to test the influence of these variables on diet composition. The empty stomachs were excluded from the diet composition analysis. In each of the remaining stomachs the frequency of occurrence of each prey item was totaled, with each appearance in a stomach counting as one occurrence of the

prey, regardless of the number of individuals of the same species in the same stomach. Unidentifiable contents were excluded from the total number of prey items observed. Then, the frequency of occurrence of each prey species was compared to the total number of organisms observed to generate percentages of the diet. Further quantitative methods were not considered due to the potential biases from regurgitation and depredation in the net. A logistic regression was used to determine significant relationships between variables, such as sex and location, and the likelihood of a stomach being empty.

All statistical analyses were performed using R (version 3.3.0), specifically RStudio (version 0.99.902). When conducting statistical tests using total length of the fish or weight of the stomach contents, both were log transformed to correct for non-normality.

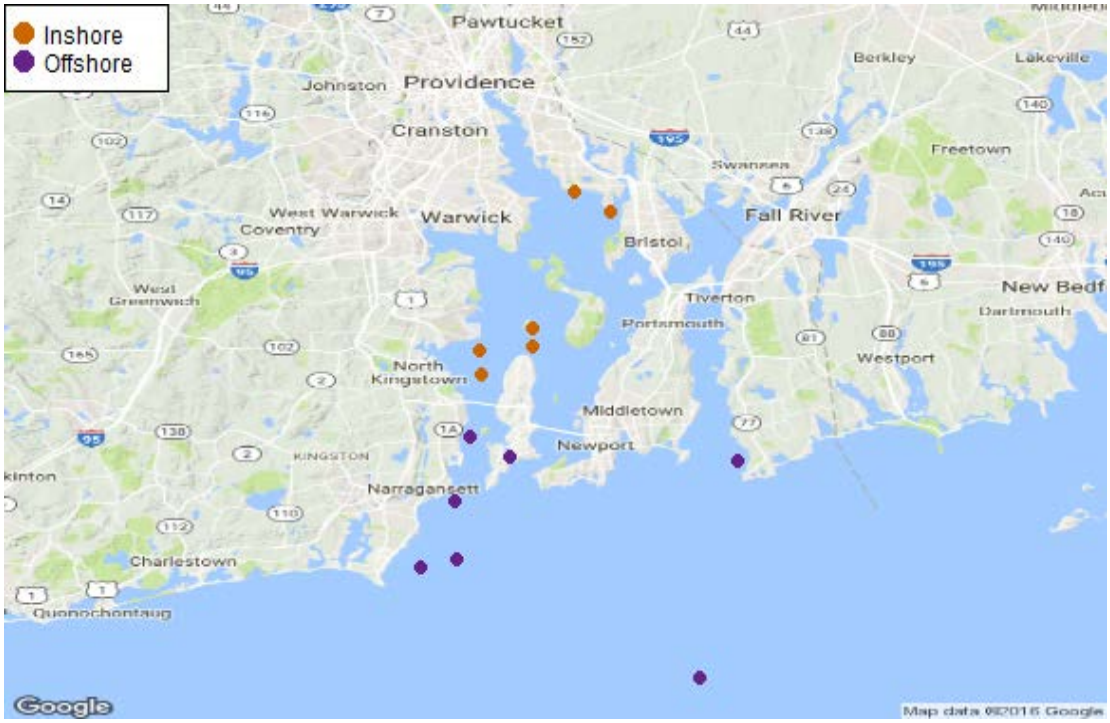

Figure 1. Trawl locations within and near Narragansett Bay where summer flounder specimens were collected.

Results

Diet Analysis

It was found that 46.63% of the stomachs considered (excluding empty stomachs marked as flaccid) had contents. Within these "full" stomachs there were 71 identifiable prey items. The most common components of the summer flounder diet were squid (*Doryteuthis pealeii*) (17/71, 23.94%), scup (*Stenotomus chrysops*) (17/71, 23.94%), and crangon shrimp (*Crangon septemspinosa)* (14/71, 19.72%). Other frequent prey items included mantis shrimp (*Squilla empusa*) (5/71, 7.04%), and silver hake (*Merluccius bilinearis*) (4/71, 5.63%). Less common prey included Say mud crabs (*Dyspanopeus sayi*), Atlantic herring (*Clupea h. harengus*), bay anchovy (*Anchoa mitchilli*), Atlantic butterfish (*Peprilus triacanthus*), tautog (*Tautoga onitis*) and Northern searobin (*Prionotus carolinus*).

Stomachs of smaller summer flounder (<40 cm) contained a higher proportion of crustaceans (44%) and fish (53%) than the stomachs of larger individuals (>40 cm) (21%

and 38%, respectively) (Figure 2). In comparison, the stomachs of larger individuals contained a much higher proportion of squid (41%) than the smaller individuals (3%) (Figure 2). The diet of the inshore individuals was primarily composed of fish (47%), followed by crustaceans (36%), with squid comprising the smallest proportion of the diet (17%) (Figure 3). In comparison, squid and fish were the most prevalent components of the offshore summer flounder diet (39%, 39%), and crustaceans were the least common component (22%) (Figure 3). In contrast to the female diet, the male diet included more crustaceans (M: 45%, F: 26%) and less squid (M: 10%, F: 29%), with the same amount of fish (M: 45%, F: 45%) (Figure 4). The summer flounder diet varied greatly between months. April was not included because only 17 individuals and 4 prey items were sampled that month. Crustaceans accounted for 57% of the diet in May, 5% in June, and 18% in July (Figure 5). Fish was the most important component of the diet in June (84%) and July (55%) and the least important in May (8%) (Figure 5). Squid followed the same pattern as the crustaceans: highest in May (35%), decreased in June (11%) and increased again in July (27%) (Figure 5)

Although there was no significant relationship found between prey presence in the stomach and the sex (p=0.203), there was a significant relationship found between whether the stomach had contents and the station (p=0.024). Of the individuals obtained from an inshore habitat, 55/97 (56.7%) had "full" stomachs, whereas only 35/96 (36.46%) of the offshore fish had "full" stomachs. A significant relationship was also found between the weight of the stomach contents and the total length of the individual (p<0.0001).

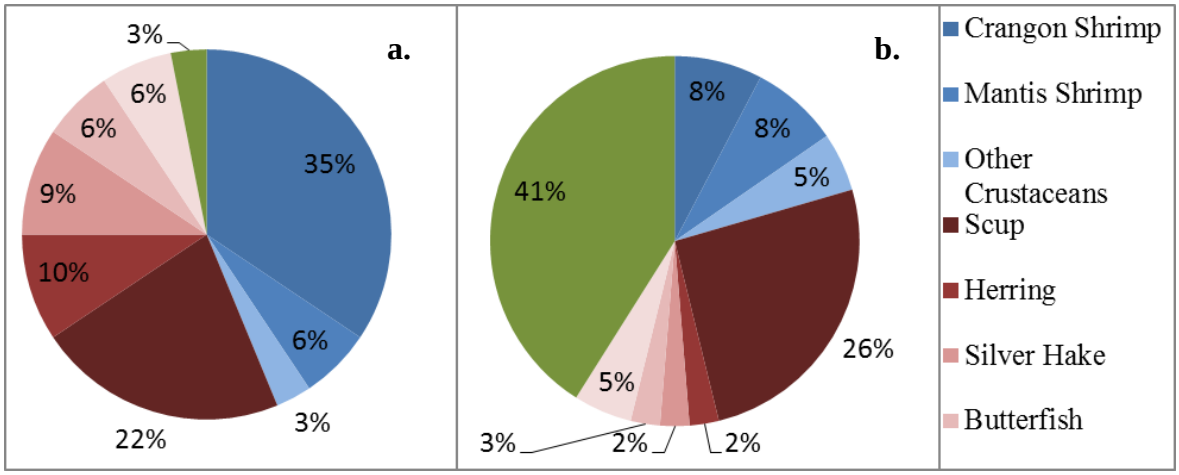

Figure 2. The diet components of (**a**) small summer flounder (<40 cm) (N=113) and (**b**) large summer flounder (>40 cm) (N=105): crustaceans (blue), fish (red), and squid (green).

Population Dynamics

The data from the 218 summer flounder retained from both fish trawls were supplemented with independently collected DEM data, resulting in sex and total length information for 281 total individuals. Sixty-five summer flounder were the minimum size for recreational harvest (45.72 cm) or larger; 63 of these 65 fish (96.92%) were female. Of the fish that were the minimum size for commercial harvest (35.56 cm) or larger (N=216), 70.37% (152) were female.

Male summer flounder were found to occupy a smaller range of sizes and had a smaller size overall compared with the females; the largest male summer flounder caught was 46.6 cm, whereas the largest female was 64.5 cm (Figure 6). The

probability of a fish being female increased as the total length of the fish also increased (Figure 7). Based on this sampling, the most probable size of a male summer flounder in Rhode Island waters was found to be between 35 cm and 40 cm, whereas the most probable size of a female summer flounder was approximately 45 cm (Figure 7).

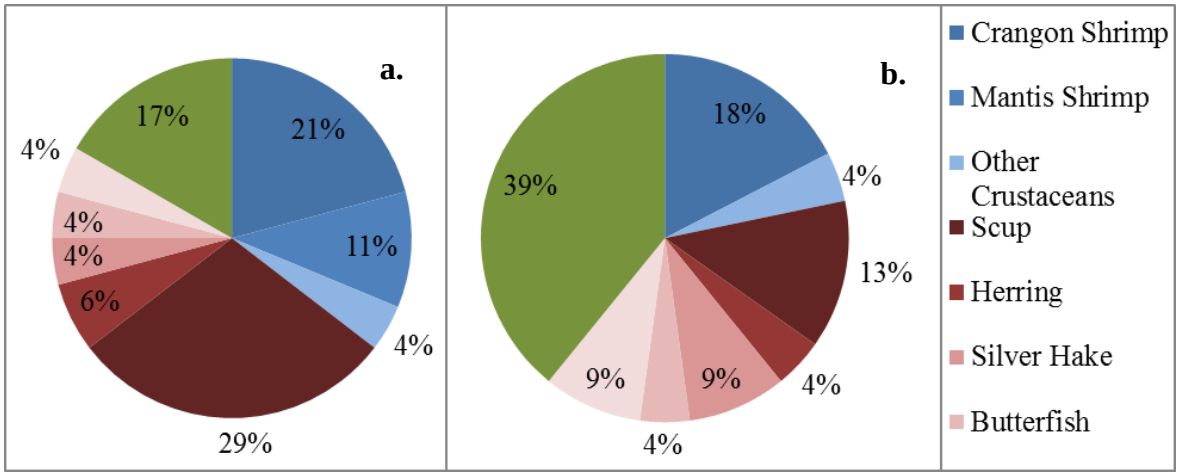

Figure 3. The diet components of (a) summer flounder caught inshore (N=106) and (b) summer flounder caught offshore (N=112): crustaceans (blue), fish (red), and squid (green).

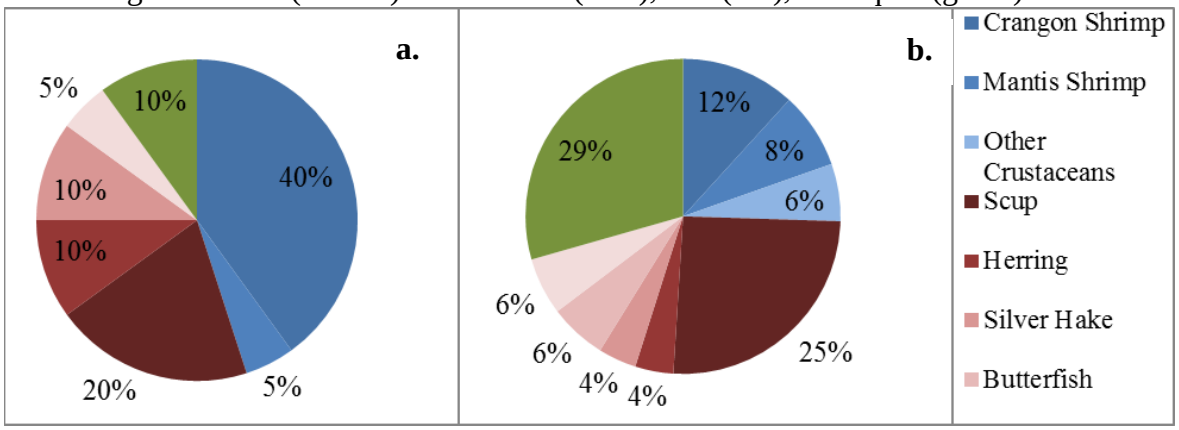

Figure 4. The diet components of (**a**) male summer flounder (N=87) and (**b**) female summer flounder (N=131). Crustaceans are in shades of blue, fish in shades of red, and squid in green.

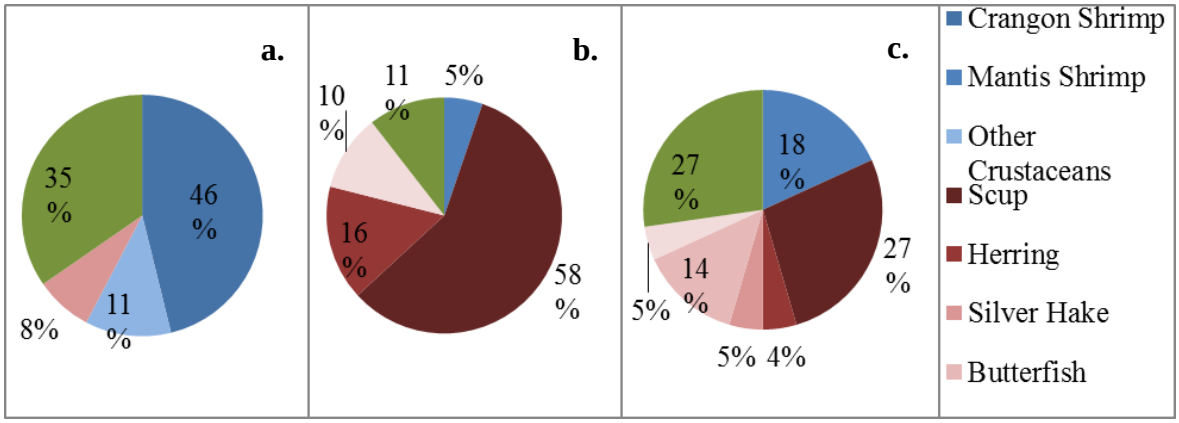

Figure 5. The diet components of (**a**) summer flounder caught in May (N=58), (**b**) June (N=61) and (**c**) caught in July (N=82): crustaceans (blue), fish (red), and squid (green).

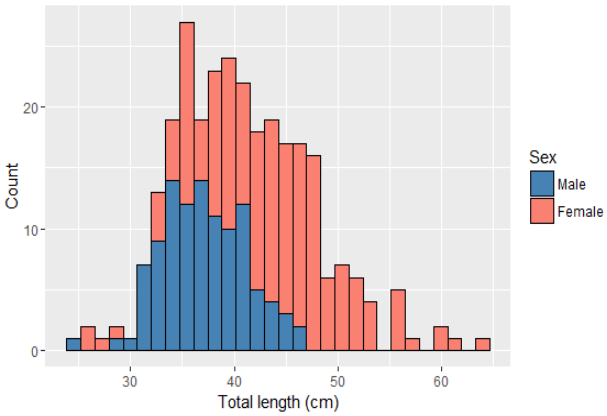

Figure 6. Histogram of total length based on sex (N=281).

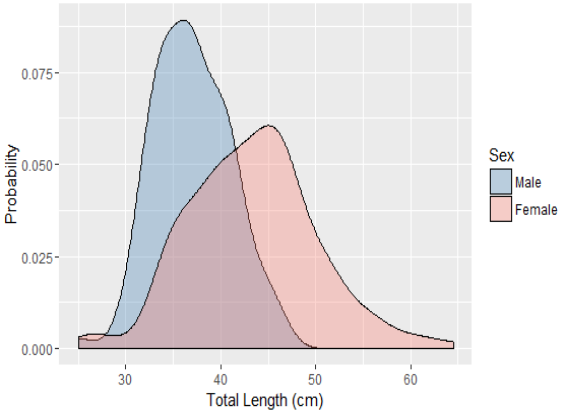

Figure 7. Probability density distribution based on sex (N=281).

The sex composition of the inshore and offshore habitats differs, with a higher percentage of females found inshore. Specifically, 67.5%-76.0% of the inshore summer flounder were female in May, June, and July, whereas females only comprised 47.62%-48.98% of the offshore population for these same months (Figure 8). There were approximately twice as many females inshore than offshore. Therefore, the probability of a fish being female inshore was found to be up to 20% greater than offshore (Figure 9). The month of April was again excluded in this analysis because only 17 of the 218 summer flounder were caught during this time period, and the small sample size may not accurately reflect the population given the sporadic and variable catch observed during this month. Small sample size notwithstanding, in April, 50% of the summer flounder inshore were female and 77.78% were female offshore.

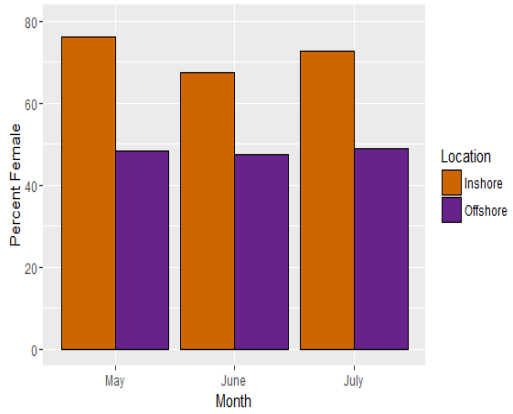

Figure 8. Percent female based on location (N=201).

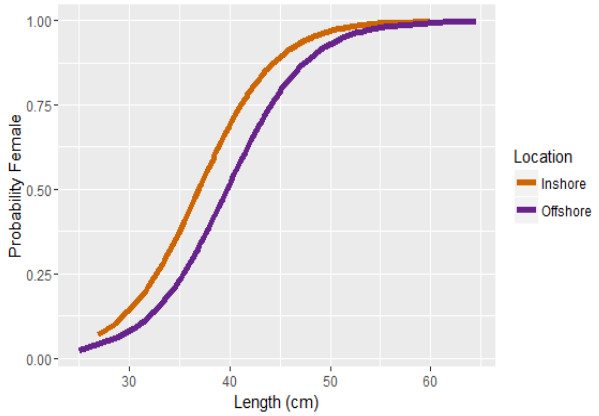

Figure 9. Logistic regression curve comparing the probability of a summer flounder being female by location (N=218).

Discussion

Diet Analysis

There have been many studies conducted on the diet of the summer flounder (e.g. Buchheister and Latour, 2011; Latour et al., 2008; Manderson et al., 2000; Sagarese et al., 2011; Staudinger, 2006; Wuenschel et al., 2013), but none specifically in Narragansett Bay. Investigations conducted by Buchheister and Latour (2011), Latour et al. (2008), Manderson et al. (2000), and Sagarese et al. (2011) noted the importance of crustaceans,

such as crangon shrimp and mantis shrimp, as components of the summer flounder diet, which is in accordance with the results found here. Additionally, Latour et al. (2008) found that there were ontogenetic changes in the summer flounder diet. Wuenschel et al. (2013) noted these shifts as well; specifically they found that as summer flounder grow, and therefore age, they transition from a diet dominated by crustaceans to one supplemented with more squid and fish. This trend was supported by the flounder in Narragansett Bay, as crustaceans were found to be superseded by fish and squid in frequency of occurrence in the diet of the larger size class.

Several summer flounder diet studies (e.g. Buchheister and Latour, 2011; Latour et al., 2008; Sagarese et al., 2011; Wuenschel et al. 2013) describe the summer flounder diet as diverse, which also supports the results of the present study. Here, four species of crustaceans and eight species of fish were present in the summer flounder diet. Sagarese et al. (2011) found that the components of the summer flounder diet fluctuated based on location, specifically between the contrasting environments of the North and South shores of Long Island, New York. Similarly, a difference in diet was found between the differing inshore and offshore habitats of Narragansett Bay.

Likely linked to this pattern, the studies conducted by Latour et al. (2008), Manderson et al. (2000), Sagarese et al. (2011), Staudinger (2006) and Wuenschel et al. (2013) also all found that the diet of summer flounder varied based on month or season. Again, this is similar to the results of this diet study where prey composition greatly shifted depending on the month. Both of these diet trends appeared to simply reflect the availability of prey species inferred from the URI GSO fish trawl catch among the habitat classifications and months sampled. Based on the opportunistic and varied diet of this species (Buchheister and Latour, 2011; Latour et al., 2008; Sagarese et al. 2011; Wuenschel et al. 2013) it therefore seems very likely that the diet of summer flounder is highly dependent on the abundance and spatial distribution of available prey.

Despite the number of diet studies conducted on summer flounder, few have compared the diets of males and females. This has caused uncertainty about the potential for differences in feeding frequency between the sexes. Such differences would lead to a bias in studies on sex composition using recreational landing data (Morson et al., 2012; Northeast Fisheries Science Center, 2013). The current work has allowed for clarification of this uncertainty, finding no significant relationship between sex and whether the stomach was "full" or "empty," implying that females do not eat at a higher frequency than males. However, Morson et al. (2015) found that growth rates of summer flounder are different between fishery-dependent and fishery-independent data, suggesting that gear, or the spatial distribution of sampling, may influence the patterns observed in the catch in a manner undetectable by the methods used here.

Population Dynamics

It has been found that female summer flounder grow larger and faster than their male counterparts (King et al., 2001). Similarly, the probability of a fish being female was found here to increase with total length. The most probable size of males was found to be approximately the minimum size for commercial harvest and the most probable size of females approximately the minimum size of recreational harvest (Figure 7). Since fishing mortality has the greatest influence on the distribution of summer flounder (Bell et al. 2014a; Bell et al., 2014b), the results of this study could be reflecting the impact of fishing pressure on the summer flounder population. Just as Morson et al. (2012) found in the New Jersey fishery in 2009 and 2010, this study

found that flounder that were the minimum size for recreational harvest were almost entirely female.

Morson et al. (2012) also found that the sex ratios were impacted by the port at which they were collected. The Narragansett Bay data reflected a relationship between sex ratio and location of the fish, inshore or offshore. However, unlike Morson et al. (2012), a significant relationship between the sex ratios and month of capture could not be identified. Although Morson et al. (2012) found that fish caught in June were significantly more likely to be female than the fish caught in August, this study found consistent sex ratios in May, June, and July. The difference in these results could be due to a migration of summer flounder. Summer flounder migrate inshore as the waters warm in the spring and migrate offshore in the fall (Murawski, 1993; Wuenschel et al. 2013). Although this study characterized locations in Narragansett Bay as inshore or offshore, federal trawl surveys and commercial fishing still often take place farther offshore than these sampling locations. If the present study locations were far enough inshore that they served as an endpoint to seasonal migrations, then it could explain why the sex ratios observed were consistent each month. Meanwhile, if the locations used in the Morson et al. (2012) study were on active migration routes, significant differences in the sex ratio based on month could be expected. Another uncertainty posed by the Northeast Fisheries Science Center (2013) and Morson et al. (2012) is the potential of the males migrating inshore later, and thereby influencing the recreational fishery data. As previously stated, this study found consistent sex ratios each month, despite increases in overall abundance, which contradicts the theory that males migrate inshore later, and suggests both sexes migrate at similar times.

Another uncertainty posed by the Northeast Fisheries Science Center (2013) to consider when updating the summer flounder stock assessment is whether the federal trawl surveys are truly reflective of the inshore population. The data presented here supports the conclusion that the federal trawl survey is not an accurate representation of the inshore population (Figure 10). Morson et al. (2015) found that the federal trawl survey was not representative of commercial and recreational fisheries. They found that the females landed through recreational and commercial fisheries grew faster than those collected in the federal trawl survey, whereas the males collected in the federal trawl survey grew faster than the males landed in the commercial and recreational fishery.

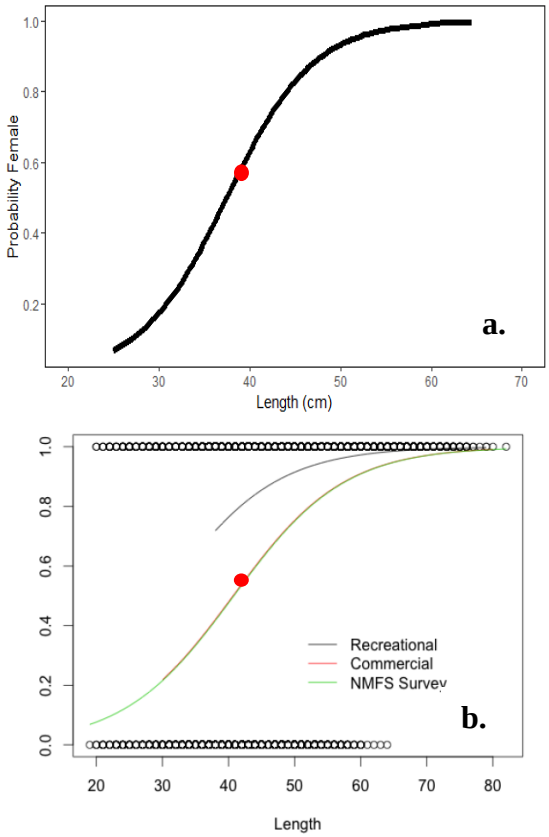

Figure 10. Logistic regression curve of the probability of being female to the total length (**a**) in Narragansett Bay (N=281) compared to (**b**) the National Marine Fisheries Service trawl data as published in the Summer Flounder Stock Assessment for 2013 (2013). Symbol represents 50% probability of being female.

Our results show that larger summer flounder are more likely to be female, and that the inshore population has a higher percentage of females than the offshore population. Management strategies that consider the sex ratios of the summer flounder could be implemented if the population begins to decline, or to prevent future overexploitation. For example, restrictions could be placed on inshore commercial fishing to prevent the disproportionate removal of females, or recreational slot-trophy limits with a size range consisting of a more equal sex ratio could be implemented. In summary, these results provide important consideration for managing the nearshore summer flounder population to ensure the continuation of a sustainable fishery.

Conclusions

There is a higher proportion of female summer flounder inshore than offshore; therefore, the offshore sex ratios, including those gathered through federal trawl surveys, are not reflective of inshore sex ratios. Males do not migrate inshore later than females, as shown by the consistent sex ratios between months of this study. The summer flounder are eating a varied diet that likely reflects local prey species abundances, but they do not appear to be consuming any commercially important species with populations in poor health in Rhode Island waters.

Acknowledgments. This research was supported by the National Science Foundation (NSF) Research Experience for Undergraduates (REU) program (Grant #1460819). We thank Scott Olszewski, Thomas Angell and Nicole Lengyel from RI Department of Environmental Management for providing summer flounder from their fish trawl and providing data. We also thank Captain Tom Puckett of the R/V *Cap'n Bert* as well as all others that assisted on the fish trawl collecting summer flounder specimens. We also thank the Summer Undergraduate Research Fellowship in Oceanography (SURFO) program and those involved with the program, specifically Steve Tadros and Drs. Lucie Maranda, Kathleen Donahue, and David Smith.

References

Bell, R. J., J. A. Hare, J. P. Manderson, and D. E. Richardson. 2014a. Externally driven changes in the abundance of summer and winter flounder. ICES Journal of Marine Science. 71(9):2416-2428

Bell, R. J., D. E. Richardson, J. A. Hare, P. D. Lynch, and P. S. Fratantoni. 2014b. Disentangling the effects of climate, abundance, and size on the distribution of marine fish: an example based on four stocks from the Northeast US shelf. ICES Journal of Marine Science. 72(5):1311-1322

Buchheister, A. and R. J. Latour. 2011. Trophic ecology of summer flounder in lower Chesapeake Bay inferred from stomach content and stable isotope analysis. Transactions of the American Fisheries Society. 140(5):1240-1254

Collie J. S., A. D. Wood, and H. P. Jeffries. 2008. Long-term shifts in the species composition of a coastal fish community. Canadian Journal of Fisheries and Aquatic Sciences. 65: 1352-1365, doi:10.1139/F08-048

Collie, J. S. 2016. University of Rhode Island Graduate School of Oceanography Fish Trawl Survey (1959-2016). Information available from http://www.gso.uri.edu/fishtrawl/

King, N. J., G. C. Nardi, and C. J. Jones. 2001. Sex-linked growth divergence of summer flounder from a commercial farm. Journal of Applied Aquaculture. 11(1/2):77-88, doi:10.1300/J028v11n01_07

Latour, R. J., J. Gartland, C. F. Bonzek, and R. A. Johnson. 2008. The trophic dynamics of summer flounder (Paralichthys dentatus) in

Chesapeake Bay. Fishery Bulletin. 106(1):47-57

Levitus, S., J. Antonov, and T. Boyer. 2005. Warming of the world ocean, 1955-2003. Geophysical Research Letters. 32: L02604, doi:10.1029/2004GL021592

Manderson, J. P., B. A. Phelan, A. W. Stoner, and J. Hilbert. 2000. Predator-prey relations between age-1+ summer flounder (Paralichthys dentatus, Linnaeus) and age-0 winter flounder (Pseudopleuronectes americanus, Walbaum): predator diets, prey selection, and effects of sediment and macrophytes. Journal of Experimental Marine Biology and Ecology. 251(1):17-39

Maunder, M. N. and R. A. Wong. 2011. Approaches for estimating natural mortality: Application to summer flounder (Paralichthys dentatus) in the U.S. and mid-Atlantic. Fisheries Research. 111(1):92-99

Morson, J. M., E. A. Bochenek, E. N. Powell, and J. E. Gius. 2012. Sex at length of summer flounder landed in the New Jersey Recreational Party Boat Fishery. North American Journal of Fisheries Management. 32(6):1201-1210

Morson, J. M., E. A. Bochenek, E. N. Powell, E. C. Hasbrouck, J. E. Gius, C. F. Cotton, K. Gerbino, and T. Froehlich. 2015. Estimating the sex composition of the summer flounder catch using fisher-independent data. Marine and Coastal Fisheries. 7(1):393-408

Murawski, S. A. 1993. Climate change and marine fish distributions: forecasting from historical analogy. Transactions of the American Fisheries Society. 122(5):647-658

National Marine Fisheries Service. 2016. Fisheries Economics of the United States, 2014. U.S. Department of Commerce, NOAA Tech. Memo. NMFS-F/SPO-163, 237p.

Northeast Fisheries Science Center. 2013. Summer flounder stock assessment for 2013, p. 17-419. In 57th Northeast Regional Stock Assessment Workshop (57th SAW) Assessment Report

Sagarese, S. R., R. M. Cerrato, and M. G. Frist. 2011. Diet composition and feeding habits of common fishes in Long Island Bays, New York. Northeastern Naturalist. 18(3):291-314

Olszewski, S. 2016. Rhode Island Department of Environmental Management Fish Trawl Survey (1995-2016).

Smith, L. M., S. Whitehouse, and C. A. Oviatt. 2010. Impacts of climate change on Narragansett Bay. Northeastern Naturalist. 17(1):77-90

Staudinger, M.D. 2006. Seasonal and size-based predation on two species of squid by four fish predators on the Northwest Atlantic continental shelf. Fishery Bulletin. 104(4):605-615

Wuenschel M. J., K. W. Able, J. M. Vasslides, and D. M. Byrne. 2013. Habitat and diet overlap of 4 piscivorous fishes: variation on the inner continental shelf off New Jersey. Fishery Bulletin. 111(4):352-369

Key Points:

- The majority of summer flounder of recreational harvest size are female (96.92% in this study)
- There is a greater proportion of female summer flounder inshore (67.5%-76% inshore, 47.62%-48.98% offshore)
- Slot-trophy limits or restricted inshore commercial fishing could protect the species from overexploitation

Key Index Words:

Summer flounder; Narragansett Bay; population dynamics; trophic ecology.

Non-volcanic tremors associated with slow slip event in South Central Alaska between 2009-2013

Whitney Schultz[1,2], Blake Cross[1,2], Meng Wei[1]

[1]Graduate School of Oceanography, University of Rhode Island, Narragansett, RI 02882, U.S.A.
[2]Geopphysical Engineering Program, Colorado School of Mines, Golden, CO 80401, U.S. A.
Corresponding author: matt-wei@uri.edu

Abstract

A slow slip event between 2009 and 2013 has been recorded in south central Alaska near the epicenter of the 1964 M9.2 earthquake. It is unclear if there is any change of non-volcanic tremors associated with the slip event. We search for tremor signals from January 2005 to May 2015 using seismic data from local seismic networks in this region. The data are filtered using a band-pass filter between 1-6 Hz. Potential tremors are detected using a waveform envelope method and are then visually inspected under several general criteria for validation. The observed tremors were recorded in a time series portraying frequency of occurrence per month. The tremor activity increased in 2010 and decreased from 2010 to 2013 then leveled off in 2014. This shows that tremor activity did intensify during the slip event and returned to normal after the conclusion of the slow slip event. There was no systematic change in the duration of the tremors before, during, and after the slow slip event. Seasonal variations in tremor activity with a peak in summer are also observed and are likely related to the seasonal hydrological loading. We locate the tremors using a 1D seismic velocity model, and their horizontal locations are near the downdip limit of the slow slip area. The depth of tremors is not well resolved due to the limited number of seismic stations in this region. Our study confirms the occurrence of non-volcanic tremors associated with the 2009-2013 slow slip event in south central Alaska.

Episodic tremor and slip (ETS) was first reported in Cascadia (Rogers and Dragert, 2003). Since then, ETS has been observed in many subduction zones including those in southwest Japan, Costa Rica, Mexico, and New Zealand (Peng and Gomberg, 2010; Dixon et al., 2014). Through detailed analysis of these events, our understanding of the variety of slip events has been improved significantly. In most cases, ETS occur near the downdip end of the mega-earthquake rupture area (Ghosh et al., 2012) and are likely caused by high pore pressure in the fault zone (Rubinstein et al., 2007, 2010; Audet et al., 2009).

ETS studies in Alaska are quite limited. Only one slow slip event (SSE) between 1998-2001 (Ohta et al., 2006) and the associated change in non-volcanic tremor (Peterson and Christensen, 2009) have been reported before 2010, which is partly due to the long interval between and duration of ETS events in Alaska. A low velocity zone identified in the south central Alaska where ETS occur suggests high pore-pressure on the fault interface (Kim et al., 2014). Tremors have also been identified along the Alaska-Aleutian subduction zone (Brown et al., 2013) and at two spots favoring dynamically triggered tremors in south central Alaska (Gomberg and Prejean, 2013). Between 2009-2013, two slow

slip events have been observed on the newly established Plate Boundary Observatory (PBO) GPS network at two separate but nearby locations (Figure 1). One SSE between 2009-2013 is near the slip area of the 1998-2001 SSE (Fu and Freymueller, 2013; Fu et al, 2015) and another 2010-2012 SSE is farther southwest (Wei et al., 2012). In the same time, enhanced seismic activity has also been observed with the slow slip event (Wei et al., 2012; Fu et al., 2015). However, Wech (2016) searched tectonic tremor in this region between 2007-2015 and found no-temporal change in tremor intensity related to the 2009-2013 SSE.

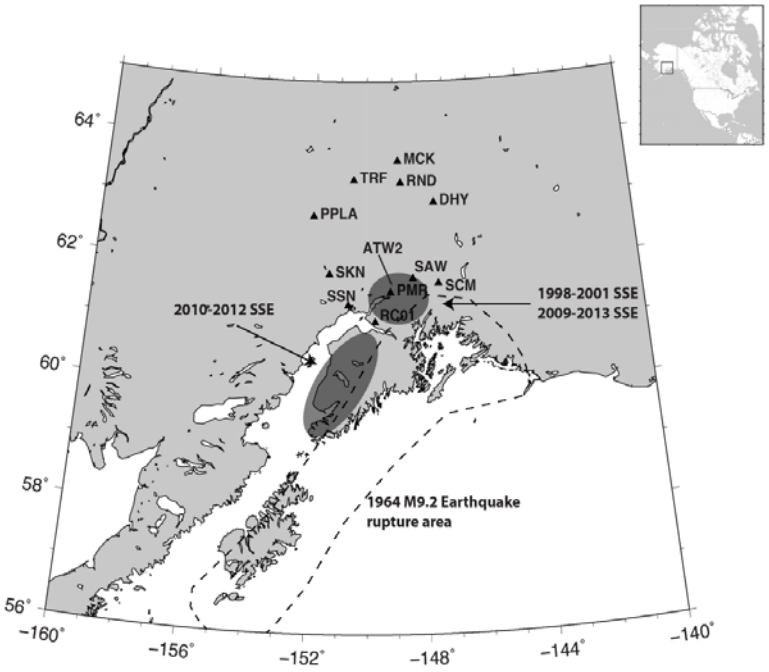

Figure 1. Map of south central Alaska, including the seismic stations (triangles) that are used in this study. Stations MCK, SAW, PMR are used for locating but not identifying tremors. The darker regions are the slip area of three known SSEs (Wei et al., 2012; Ohta et al., 2006; Fu et al., 2015). The dashed line highlights the rupture area of the 1964 M9.2 earthquake. GPS station ATW2 is very close to seismic station PMR.

In this paper we search and locate tremors between January 2005 and May 2015 using seismic data from the Alaska Regional Network, the National Tsunami Warning System Seismic Network, and the Multidisciplinary Observations of Subduction Array. Unlike Wech (2016), we focus on tremors with duration longer than 3 minutes and in the area near the 2009-2013 SSE. All the tremors discussed in this paper are non-volcanic, which means that they are not related to any volcanic processes. The methodology is adopted from many previous studies (Obara, 2002; Rogers and Dragert, 2003; Wech and Creager, 2008; Peterson and Christensen, 2009). Due to the large amount of data, we picked six stations with the longest record and near the previous non-volcanic tremor locations identified by Peterson and Christensen (2009) to monitor temporal changes of tremor activities. Then we used three additional stations to locate several well-recorded tremors. We also documented the durations of these tremors and explored

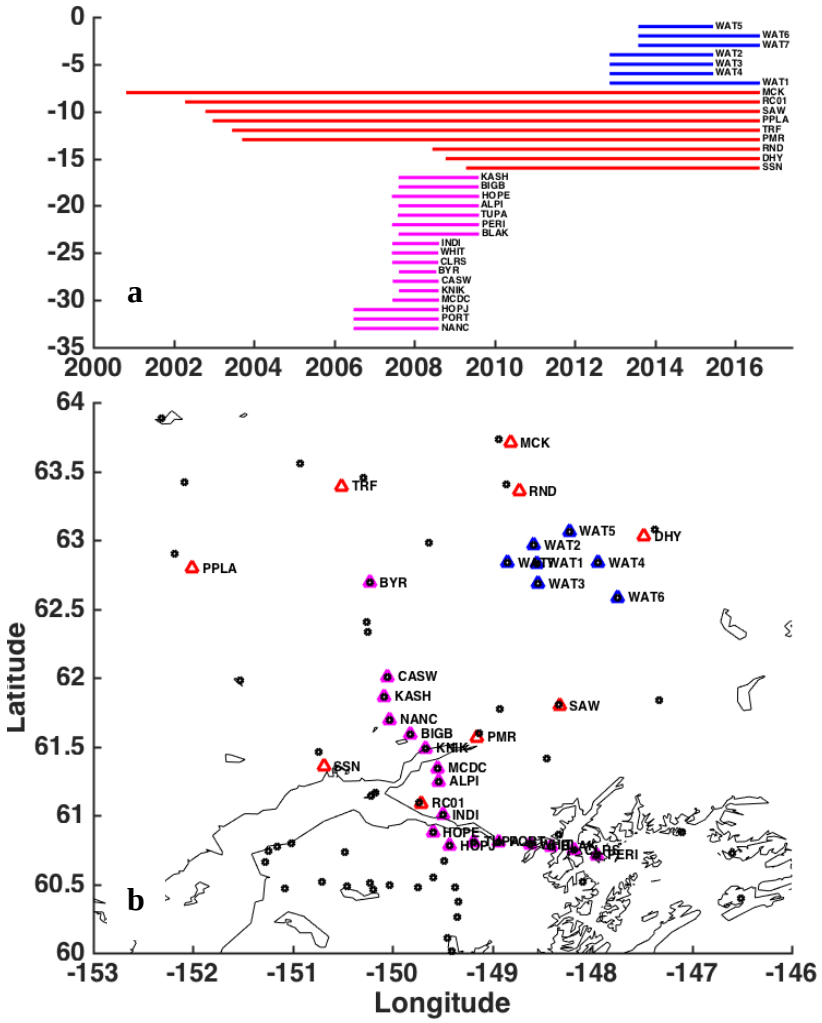

Figure 2. Temporal change in station coverage in the study area. (a) Time span of seismic stations used in this study. (b) Map of south central Alaska. Red triangles are the AK stations used to track the temporal change of tremor activities. 18 YV stations (Magenta triangles) exist between summers of 2007 and 2009. Seven stations (blue triangles) were established in summer 2012 and 2013, with station names starting with WAT. Black circles are stations that exist but were not used for poor data quality or too far away to the study area.

possible dynamic triggering by regional and global large earthquakes.

Data

We used seismic data from the Alaska Regional Network, the National Tsunami Warning System seismic network, and the Multidisciplinary Observations of Subduction array (Figure 1). All the data were downloaded from Data Management Center (DMC) database of the Incorporated Research Institutions for Seismology (IRIS). The corresponding network code are AK, AT, and YV, respectively. Some stations and network only exist for a short time period (Figure 2). The YV network is temporary and only exists between summers of 2007 and 2009. Several new stations with names of WAT are established in summer of 2012. To minimize the bias from additional stations, we use eight

stations that span 2010-2015 and six stations that span 2005-2010 as the main stations to detect the tremor activities. Later we will show that the additional stations do not increase the number of detected tremors much. Therefore, our approach provides a robust way to measure the temporal change of non-volcanic tremors in this region. to measure the temporal change of non-volcanic tremors in this region. show that the additional stations do not increase the number of detected tremors much. Therefore, our approach provides a robust way to measure the temporal change of non-volcanic tremors in this region.

The Alaska Regional Network provides most of the seismic data that are used for identifying tremors. The AK network currently has 121 stations that predominantly cover the area of south central and southeastern Alaska. The data are recorded at a rate of 50 data points per second. Out of the 121 stations, we choose eight stations to monitor the tremor activity changes since 2010. These eight stations cover the northern part of the area of the 2009-2013 slow slip event and tremors (Figure 1). For locating tremors, we used three additional stations, MCK and SAW are from the AK network, and PMR is from the AT network. The YV network is available between summers of 2007 and 2009. We used a subset of the YV network to see if additional tremors are identified by the additional stations.

Methods

Identifying non-volcanic tremors

Non-volcanic tremors are seismic signals with low frequency (1-6 Hz) and long duration (at least several minutes). We adopt an envelope detection method used by many previous studies (Obara, 2002; Rogers and Dragert, 2003; Wech and Creager, 2008; Peterson and Christensen, 2009). Seismic data from eight AK stations are downloaded from the IRIS database using the Matlab script irisFetch.m. The waveform data are filtered through a band-pass filter for a frequency range of 1-6 Hz (Peterson and Christensen, 2009). Signals from local earthquakes are masked out based on a ratio of peak amplitude and background noise. Once earthquakes are removed an envelope is created to overlay the waveform. The data are then run in hour sections and automatically screened to produce a list of possible tremor events. Only events that last longer than three minutes are listed. In the meantime, figures with hourly waveforms are produced and are used to visually inspect the tremors under the following criteria: (1) the tremors last for more than three minutes, (2) they lack evident P and S waves, (3) there is no sharp increase in signal, and (4) the times of increased seismic signals from at least three stations are closely aligned and the shapes look alike. From this visual inspection, a list of determined tremors is created and used to show tremor activity per month since January 2005. The visual inspection primarily removes earthquake signals, characterized as a sudden onset of large energy. Over 90% of events were identified as earthquakes therefore not included in the tremor list. An example of the tremor signals is shown in Figure 3a. This tremor event occurred in September 19, 2010. The signal lasted about 10 minutes and showed up in all the eight stations. The similarity of the signal and the timing suggest that the signals are from the same event. Figure 3b illustrates an hour of waveform that the Matlab code identified as possible tremors, but were excluded by visual inspection. A clear onset of large energy indicates this to be an earthquake instead of a tremor. This particular event is possibly a glacial event because of the sharp onset and it is occurring in an area known for producing large glacial calving signals (Wolf and Davis, 1986). The waveform in stations PPLA and TRF, in figure 3c, is cut based on the large signal-to-noise ratio of this earthquake.

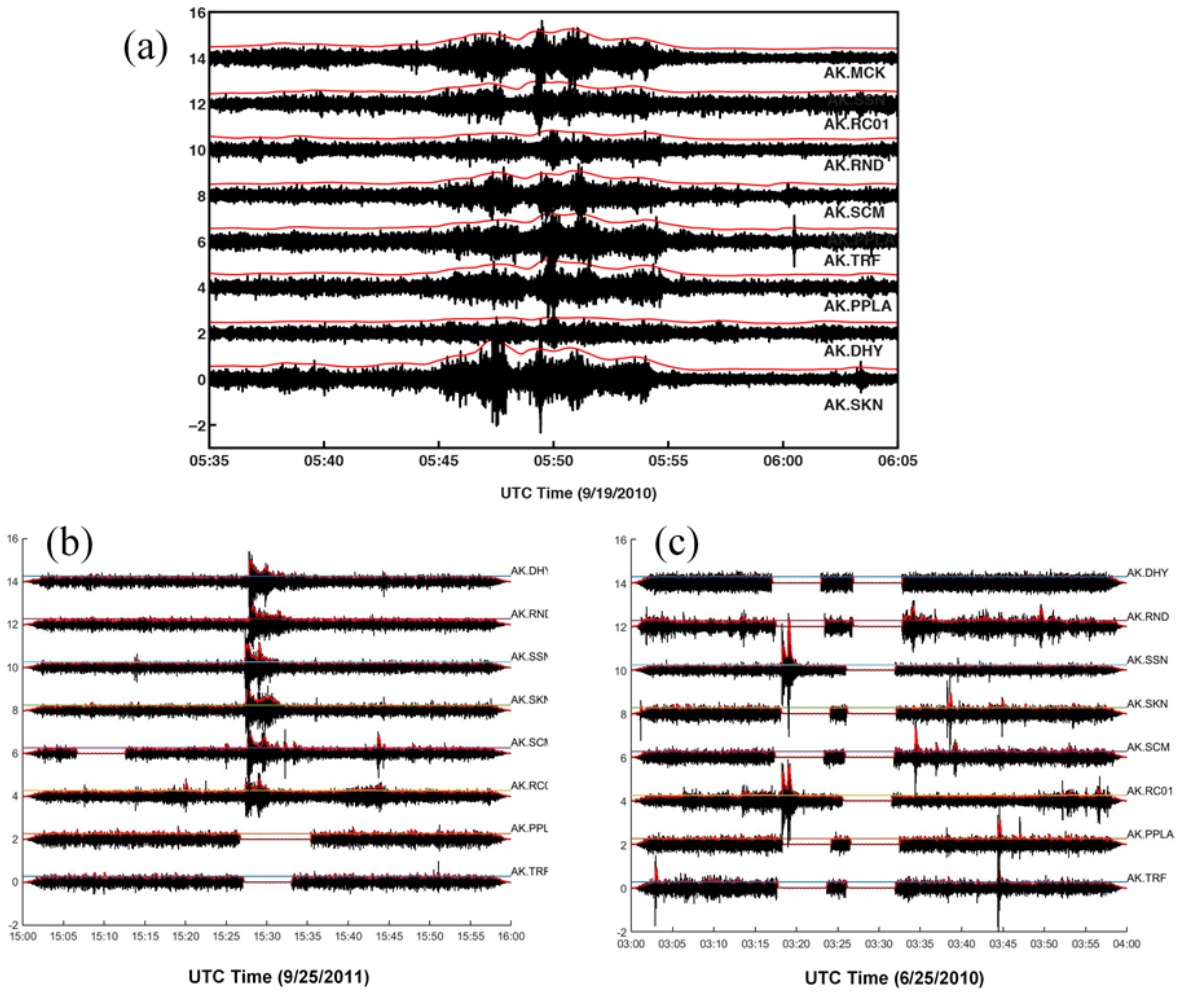

Figure 3. (a) Waveforms of a well-recorded tremor on September 19, 2010. The black lines are the band-pass filtered waveform and the red lines are the smoothed envelopes. (b) A typical seismic signal not identified as a tremor. This example was identified as a possible tremor by the script automatically but was excluded from the list of tremor because of the sharp increase in signal that is indicative of earthquakes. (c) Another earthquake that was automatically identified as a possible tremor. The earthquake is masked out on most of the stations, but it is still seen at two stations.

We locate tremors to understand the spatial relationship between the slow slip event and tremors. First, the lag time between stations is determined by cross correlating the smoothed envelopes of different stations (Figure 3a). Then, for simplicity, we forward model the arrival time using a 1D-velocity model based on CRUST 1.0 (Laske et al., 2013) even though more complex models are available (Wang and Tape, 2014). Next we perform a grid search including location (x,y), depth (z) and origin time (dT). For each grid, a misfit is calculated between the modeled and observed arrival times. The grid that generated the smallest misfit is considered as the most likely location and origin time of tremors. We have good constraints on the horizontal location of the tremors. Resolving the depth is less successful, with the smallest misfit point being usually the largest depth in the search grid (Figure S1 in Supplementary Materials). The difficulty of resolving depth is expected (Wech and Creager, 2008).

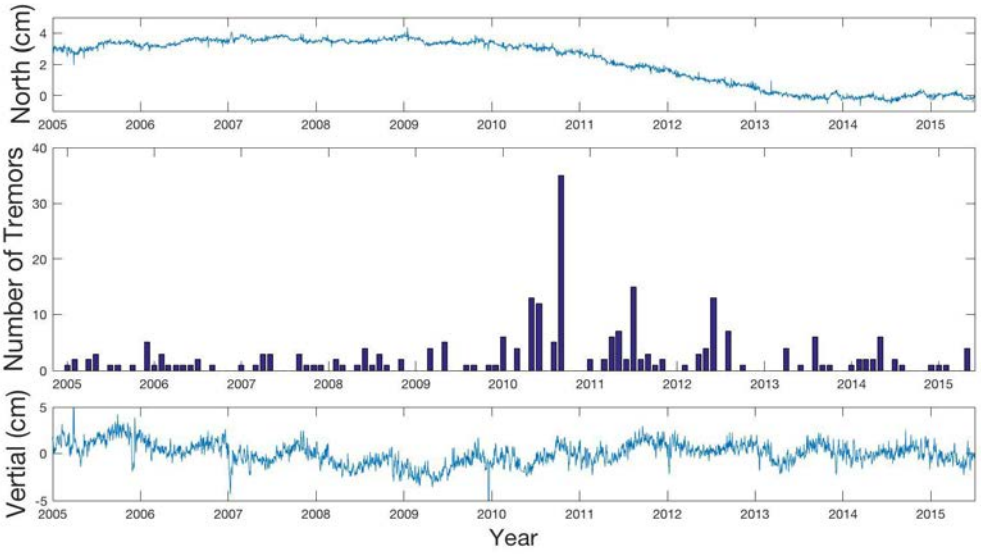

Figure 4. Surface displacement at GPS station ATW2 and tremor activities at eight stations between January 2005 and May 2015. (a) Displacement in the north direction at station ATW2. A linear trend has been removed. (b) The number of tremors per month at eight stations. (c) Vertical displacement at station ATW2. A linear trend has been removed.

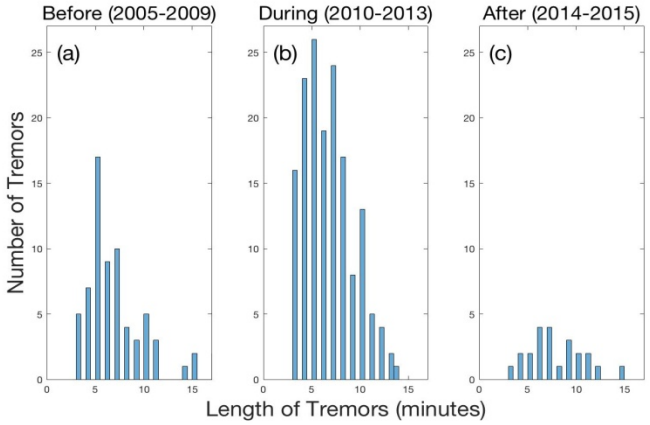

Figure 5. Duration of tremor duration before, during and after the 2009-2013 SSE.

Results

A total of 251 tremors with durations longer than three minutes have been identified between January 2005 and May 2015. The tremor activity per month is plotted on the same figure as the north and vertical displacement recorded in a nearby GPS station (ATW2) (Figure 4). The GPS data in north direction show about 3 cm southward slip over the course of 2010 to the start of 2013, with no significant change in displacement afterward. During the time of the slow slip event, there was an average of 45 tremors per year in contrast to the years with no slow slip event, both before and after the SSE, that had an average of 10 tremors per year.

The tremor activity shows a seasonal variation that peaks in the summer. The months for each year of peak tremor activity on average for the eight stations are, in order starting from 2010 and not including 2015, September, July, June, August, and May,

showing a tendency for tremor activity to peak in or around the summer months (Figure 4b). In south central Alaska, seasonal hydrological loading can be significant (Fu et al., 2012) and might modulate tremor activity. In this study, the peak of tremor activity each year is at the time of the highest vertical displacement at GPS station ATW2 in year 2010 and 2013 but not in other years (Figure 4b,c), suggesting a possible but complex link between hydrological loading and tremor activity. However, the decrease of tremor activity in each year since 2010 is more likely related to the nearby SSE because no decrease of hydrological loading is observed in vertical GPS data (Figure 4c). Annual cycles of tremor activity are also observed in northern Cascadia where tremor events tend to occur in the third quarter of the year and match the annual cycle of hydrological loading (Pollitz et al., 2013).

The duration of the tremors was visually estimated. Before and during the SSE, the most common tremor length is 5 minutes (Figure 5). The distributions are very similar before, during, and after the 2009-2013 SSE, indicating that the event has no effect on the duration of the tremors. This is different from what happened in 1998-2001, where Peterson and Christensen (2009) found a decrease in the duration of tremors towards the ending of the 1998-2001 SSE. There are a number of possible reasons.

Large earthquakes can trigger non-volcanic tremors (Gomberg et al., 2008; Rubinstein et al., 2007; Han et al., 2014). However, there is no correlation between large earthquakes and increases in tremor activity in our study (Figure 6). There are two spikes in tremor activity, one in 2008 and one in 2011, which line up with an earthquake. A close look at the timing between these events reveals that there are no tremor occurrences shortly after these events. We only focus on tremors with duration longer than three minutes. This is likely why no earthquakes triggered tremors in this study.

We locate all the identified tremors that occurred between January 2005 and May 2015 (Figure 7). We fix the depth at 40 km. In most cases, the tremors occur near the downdip end of the slow slip event, which shows a possible link between the two phenomena. Tremors are labeled based on their occurrence before, during, or after the SSE. There is no connection between the location of the tremor and the time that it occurred. The tremors that we were unable to locate either did not have enough station coverage or were located too far outside of the circle of MK stations to determine an accurate location. These tremors could be related to the tremor clusters identified by Wech (2016) to the North East of the current area of interest. The depth of the tremors are not well constrained. The misfit between modeled and observed arrival time tends to decrease with depth until at least 100 km. However, it is hard to imagine physically how a tremor can occur at 100-km depth. Therefore, we solve tremor locations for depth from 30-60 km.

Discussion

Our results show similarities with the behavior of non-volcanic tremors related to the 1998-2001 SSE in the same area (Peterson and Christensen, 2009). First, the tremors occur at the downdip limit of the area of SSE. Second, the intensity of the tremor activity increases during the SSE and leveled off when the SSE stops. However, there are some noticeable differences. For the 1998-2001 event, tremor intensity is at its maximum in 2000, which is close to the later stage of the SSE. For the 2009-2013 event, tremor intensity is at its maximum in 2010, in the middle of the SSE. This might reflect different temporal evolution during each SSE. Also, there was a decrease of duration of tremors towards the ending of the 1998-2001 SSE, which is not observed for the 2009-2013 event. In addition, many more tremor epicenters were resolved for the 1998-2001

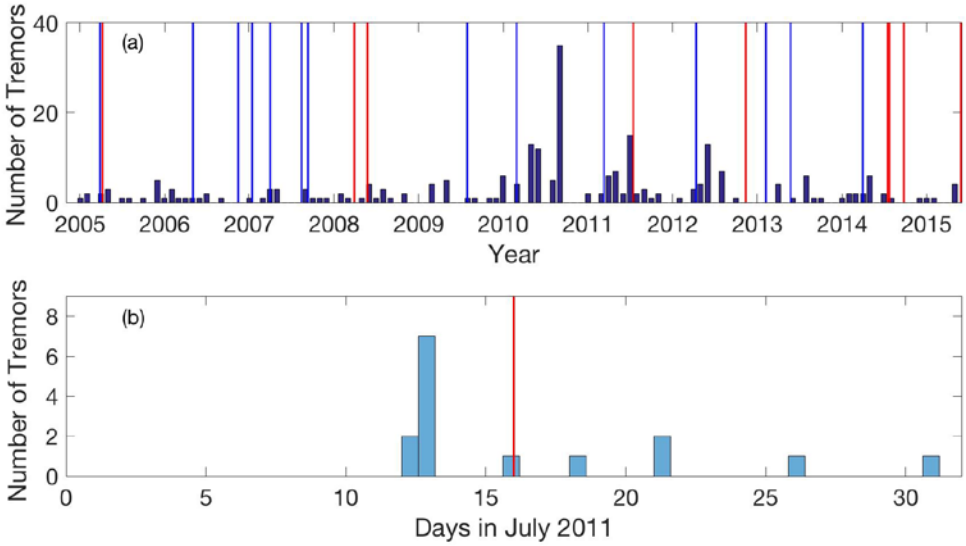

Figure 6. Correlation of tremor activity with regional M>6 (red lines) and global M>8 (blue lines) earthquakes. (a) Number of detected tremors per month aligned with timing of large earthquakes. (b) same as (a) but only shows the month of July in 2011. One tremor occurred on the same day as the M6.1 earthquake, but the tremor was recorded at 0:44:51 UTC, while the earthquake occurred at 19:59:12 UTC.

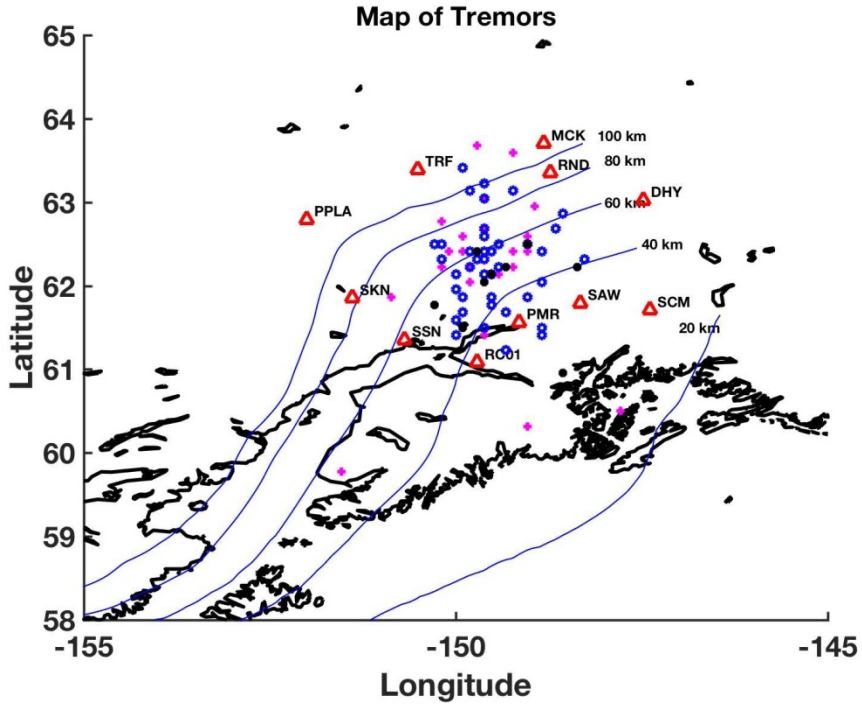

Figure 7: Locations of tremors and seismic stations. The Alaskan coast line is represented with the thick black line. The triangles are the stations used to locate the tremors, excluding the YV stations. The tremors are indicated as crosses for 2005-2009, circles for 2010-2013, and dots for 2014-2015. The GPS station ATW2 is located very close to the seismic station PMR. Thin lines represent the contour of the slab interface at depth (Li et al., 2013).

event as a temporary seismic array was in the region and provide many more seismic stations.

Several factors affect the robustness of identifying tremors. One factor is the noise level. High noise levels would prevent a tremor from showing up in the waveforms. The second factor occurs during the subjective visual inspection of the figures to confirm or deny the existence of tremors. Though the visual inspection follows a set of guidelines for identifying tremors, there are still cases where it is not possible to clearly distinguish a tremor from an earthquake or string of earthquakes. We discarded 95% of the tremor hours that the computer identified because they did not meet the guidelines necessary for the types of tremors important for this study. Another issue is due to the process of identifying tremors in hour sections, some potential tremors could have been excluded because they did not last long enough during each hour in order to be recorded as a possible tremor. These issues are diluted by the large number of possible tremors that arise and the consistency with identification; they are not significant to the point of incorrectly skewing results. However, more precise results could be obtained if better managed. Despite these reservations, the temporal data clearly show the connection through the observation of the tremor activity before and after 2013. With the tremor activity before 2013 three times larger than that after 2013 and the slow slip event ending at the start of 2013, the temporal relationship between the two appears very evident.

We were unable to locate all identified tremors because the process requires a tremor with a clearly defined arrival time and a similar shape at the different stations. The reference envelope of the tremor has a large impact when locating tremors. The reference envelope can affect the correlation among the tremors and if the correlation from one station is not strong enough, that station is not used when locating the tremor. Many times, in years with low station coverage, the parameters of the reference envelope can determine whether or not the tremor is locatable.

Wech (2016) found no temporal correlation between tremor activity and the 2009-2013 slow slip event. There are a few differences between the studies: Wech (2016) used several additional stations far east of our study region, and therefore found a lot more tremors on the west of our study area. We don't miss events that occurred within the circle. For events initiated outside, the time delay is only 1-2 minutes. So if the tremors were large enough, we see them in our method. Wech's method is more complex and sophisticated and ours is straightforward and simple. We focus on tremors that last more than 3 minutes and Wech might see more short tremors.

Conclusions

Our study confirms the occurrence of non-volcanic tremors associated with the 2009-2013 slow slip event in south central Alaska. The SSE has no effect on the duration or location of the tremors. Seasonal variations in tremor activity with a peak in summer have been observed and are likely related to the hydrological loading in this region.

Acknowledgments. We thank Lucie Maranda, Kathleen Donahue, David Smith, and Kim Carey for organizing the 2015 and 2016 SURFO program at the University of Rhode Island. We thank the National Science Foundation (grant # OCE-1460819) for providing the funding for the SURFO program. We thank Yajing Liu for a pre-review of this manuscript.

References

Audet, P., Bostock, M. G., Christensen, N. I. & Peacock (2009). S. M. Seismic evidence for overpressured subducted oceanic crust

and megathrust fault sealing. Nature 457, 76–78.

Brown, J. R., S. G. Prejean, G. C. Beroza, J. S. Gomberg, and P. J. Haeussler (2013). Deep low-frequency earthquakes in tectonic tremor along the Alaska-Aleutian subduction zone. J. Geophys. Res. 118, 1079–1090, doi:10.1029/2012JB009459.

Dixon, T. H., Y. Jiang, R. Malerservisi, R. McCaffrey, N. Voss, M. Protti, and V. Gonzalez (2014). Eartqhauke and tsunami forecasts: relation of slow slip events to subsequent earthquake rupture. PNAS 111,17039-17044, doi:10.1073/pnas.1412299111

Eberhart-Phillips, D., D. H. Christensen, T. M. Brocher, R. Hansen, N. A. Ruppert, P. J. Haeussler, and G. A. Abers (2006). Imaging the transition from Aleutian subduction to Yakutat collision in central Alaska, with local earthquakes and active source data. J. Geophys. Res. 111, 1–31, doi:10.1029/2005JB004240.

Fu, Y., and J. T. Freymueller (2013). Repeated large slow slip events at the south central Alaska Subduction zone. Earth Planet. Sci. Lett. 375, 303–311, doi:10.1016/j.epsl.2013.05.049.

Fu, Y., J. T. Freymueller, and T. Jensen (2012). Seasonal hydrological loading in southern Alaska observed by GPS and GRACE. Geophys. Res. Lett. 39, doi:10.1029/2012GL052453.

Fu, Y., Z. Liu, and J. T. Freymueller (2015). Spatiotemporal variations of the slow slip event between 2008 and 2013 in the southcentral Alaska subduction zone. Geochem. Geophys. Geosyst. 16, doi:10.1002/2015GC005904

Ghosh, A., J. E. Vidale, and K. C. Creager (2012). Tremor asperities in the transition zone control evolution of slow earthquakes. J. Geophys. Res. 117, B10301, doi:10.1029/2012JB009249.

Gomberg, J., J. L. Rubinstein, Z. Peng, K. C. Creager, J. E. Vidale, and P. Bodin (2008), Widespread triggering of nonvolcanic tremor in California., Science (80-.)., 319(5860), 173, doi:10.1126/science.1149164.

Gomberg, J., and S. Prejean (2013). Triggered tremor sweet spots in Alaska, J. Geophys. Res. 118, 6203–6218, doi:10.1002/2013JB010273.

Han, J., J. E. Vidale, H. Houston, K. Chao, and K. Obara (2014), Triggering of tremor and inferred slow slip by small earthquakes at the Nankai subduction zone in southwest Japan, Geophys. Res. Lett., 41(22), 8053–8060, doi:10.1002/2014GL061898.

Kim, Y., G. A. Abers, J. Li, D. H. Christensen, J. Calkins, and S. Rondenay (2014). Alaska Megathrust 2: Imaging the megathrust zone and Yakutat/Pacific plate interface in the Alaska subduction zone. J. Geophys. Res. 119, 1924–1941, doi:10.1002/jgrb.50358.Alaska.

Laske, G., Masters., G., Ma, Z. and Pasyanos, M. (2013). Update on CRUST1.0 - A 1-degree Global Model of Earth's Crust, Geophys. Res. Abstracts, 15, Abstract, EGU 2013-2658.

Li, J., G. a. Abers, Y. Kim, and D. Christensen (2013). Alaska megathrust 1: Seismicity 43 years after the great 1964 Alaska megathrust earthquake. J. Geophys. Res. 118, 4861–4871, doi:10.1002/jgrb.50358.

Obara, K. (2002). Nonvolcanic deep tremor associated with subduction in southwest Japan. Science 296, 1679 – 1681, doi:10.1126/science. 1070378.

Ohta, Y., J. T. Freymueller, S. Hreinsdottir, and H. Suito (2006). A large slow slip event and the depth of the seismogenic zone in the south central Alaska subduction zone. Earth Planet. Sci. Lett. 247, 108–116.

Peng, Z., and J. Gomberg (2010). An integrated perspective of the continuum between earthquakes and slow-slip phenomena. Nat. Geosci. 22, doi:10.1038/NGEO940.

Peterson, C. L., and D. H. Christensen (2009). Possible relationship between nonvolcanic tremor and the 1998–2001 slow slip event, south central Alaska. J. Geophys. Res. 114, B06302, doi:10.1029/2008JB006096.

Pollitz, F. F., A. Wech, H. Kao, and R. Bürgmann (2013). Annual modulation of non-volcanic tremor in northern Cascadia. J. Geophys. Res. 118, 2445–2459, doi:10.1002/jgrb.50181.

Rogers, G., and H. Dragert (2003). Episodic tremor and slip on the Cascadia subduction zone: The chatter of silent slip. Science 300, 1942– 1943, doi:10.1126/science.1084783.

Rubinstein, J. L., D. R. Shelly, and W. L. Ellsworth (2010). Non-volcanic Tremor: A Window into the Roots of Fault Zones, in New Frontiers in Integrated Solid Earth Sciences, edited by S. Cloetingh and J. Negendank, Springer Netherlands, Dordrecht.

Rubinstein, J. L., J. E. Vidale, J. Gomberg, P. Bodin, K. C. Creager, and S. D. Malone (2007). Non-volcanic tremor driven by large transient shear stresses. Nature 448, 579–82, doi:10.1038/nature06017.

Wang, Y., and C. Tape (2014). Seismic velocity structure and anisotropy of the Alaska subduction zone based on surface wave tomography. J. Geophys. Res. 119, 1–21, doi:10.1002/2014JB011438.Southcentral.

Wech, A. G., and K. C. Creager (2008). Automated detection and location of Cascadia tremor. Geophys. Res. Lett. 35, L20302, doi:10.1029/2008GL035458.

Wech, A. G. (2016), Extending Alaska's plate boundary: Tectonic tremor generated by Yakutat subduction, Geology, 44(7), 587–590.

Wei, M., J. J. McGuire, E. Richardson (2012). A slow slip event in the south central Alaska Subduction Zone and related seismicity anomaly. Geophys. Res. Lett. 39, 15, 1944-8007, doi: 10.1029/2012GL052351.

Wolf, B. Y. L. W., and J. N. Davies (1986), Glacier-generated earthquakes from Prince William Sound, Alaska, Bull. Seismol. Soc. Am., 76(2), 367–379.

Key Points:

- Intensity of non-volcanic tremors increases with the 2009-2013 SSE in south central Alaska Tremor activity peaks in the summer and might be related to hydrological loading
- Tremor locations are near the downdip end of the slip area of SSE.

Key Index Words:

Non-volcanic tremor; slow slip events; south central Alaska; PBO

Passive Sampling of Perfluoroalkyls in Aqueous Film Forming Foam with Polyacrylate Fibers

Christopher D. Vatral[1,2], Rachel Miller[1], Rainer Lohmann[1]
[1]Graduate School of Oceanography, University of Rhode Island, Narragansett, RI, USA
[2]Department of Chemistry, Eastern Nazarene College,Quincy, MA 02170
Corresponding author: Christopher.D.Vatral@lions.enc.edu

Abstract
Perfluoroalkyl substances (PFAS) are organic anthropogenic contaminants found ubiquitously in the environment. PFAS are commonly used in nonstick-cookware, food packaging, pesticides, water and stain repellents, and alkaline cleaners. PFASs are also key ingredients of aqueous film forming foam (AFFF), mixtures used heavily at airports and military bases to extinguish hydrocarbon fuel fibers. In recent years, exposure to C8 perfluorinated carboxylic acids and sulfonates has been linked to several types of cancer. An accurate way to sample contaminants in the environment is by using passive sampling. Passive sampling relies on the free flow of analytes from the sampling medium to the collecting device. In this study, polyacrylate fibers were tested as passive samplers for PFAS, particularly perfluorinated carboxylic acids and sulfonic acids. Polyacrylate passive samplers were used to sample dilutions of AFFF to confirm whether these passive samplers can be used to quantify PFAS in groundwater at suspected contamination sites. Polyacrylate fibers (33 and 9 µm) were submerged in AFFF dilutions for 1-24 hours; the PFAS were then extracted from the fibers. HPLC/MS-MS was used to determine the concentration of PFAS collected by the fibers. A ratio near unity of the PFAS concentrations of the two sizes of fibers would indicate that the contaminants are adsorbed on the surface of the fibers rather than dissolved in the fibers. Results show that the PFAS concentrations on the fibers decrease from C4 to C8 compounds. Future work should include varying the sampling time and determining the partitioning correlations.

This manuscript intentionally left blank

This manuscript intentionally left blank

This manuscript intentionally left blank

This manuscript intentionally left blank

This manuscript intentionally left blank

This manuscript intentionally left blank

This manuscript intentionally left blank

This manuscript intentionally left blank

Sinking Microfibers on the New England Continental Shelf Break

Jennie L. Warmack[1,2] and Melissa M. Omand[1]
[1]Graduate School of Oceanography, University of Rhode Island, Narragansett, RI, 02882 USA.
[2]Department of Oceanography, Humboldt State University, Arcata, CA, 95521 USA.
Corresponding author: momand@uri.edu

Abstract
While the abundance of microfibers (< 5 mm) in coastal and deep-sea sediments is well documented, the flux and sinking speed of these particles within the water column remain unknown. In June 2016, the water column abundance and vertical flux profile of microfibers were examined using Niskin bottle collection and a vertical array of surface-tethered sediment traps (STSTs, spanning 60 to 200 m) on the R/V *Endeavor* at the continental shelf break south of Rhode Island (40°N, 71°W). Fibers were extracted and analyzed on a Fourier transform infrared spectrometer to determine the type of materials present, namely polyester and cotton. A total of 178 fibers averaging 1100 ± 1000 μm long and 11 ± 7 μm wide were imaged and quantified. Sinking rates (Ws) of the fibers were estimated through three independent approaches. The observed sediment tube flux divided by the water column concentration yielded $W_{s,\ field}$ = 2.4 ± 2.3 m day^{-1}, whereas settling chamber observations gave $W_{s,\ lab}$ = 16 ± 4 m day^{-1}. These results were compared to the theoretical Stokes sinking speed for cylindrical particles $W_{s,\ theory}$ = 12 ± 15 m day^{-1}. In general, the field-based approach indicated roughly 8x slower sinking speeds than those observed in the lab or predicted by theory. To our knowledge, this is the first study that attempts to quantify and compare in situ sinking rates with laboratory and theoretical approaches to understand the fate of microfibers in the ocean.

Plastics have permeated today's society through electronics, packaging, and synthetic clothing. Moreover, they have infiltrated today's water systems. Plastics have been observed in rivers (Castañeda et al., 2014; Wagner et al., 2014), lakes (Imhof et al., 2013; Free et al., 2014), arctic sea ice (Obbard et al., 2014), surface oceans (Law et al., 2010; Collignon et al., 2012; Reisser et al., 2013; Eriksen et al., 2014), and in ocean floor sediments (Van Cauwenberghe et al., 2013; Woodall et al., 2014; Fischer et al., 2015). While larger plastic debris such as discarded water bottles and stray fishing nets dominate the focus of the general populace and is addressed through beach cleanups, the study of microplastics (< 5 mm) (Barnes et al., 2009) has been increasing in the scientific community since the turn of the millennium (Thompson et al., 2004; Wagner et al., 2014). Microfibers, including a subset of microplastics as well as other synthetic and organic materials, have only begun to be quantified in the marine environment within the last five years (Goldberg, 1997; Browne et al., 2011).

Implications of microfibers in the marine environment are not fully known since the field is still developing, but studies are presently underway to determine the nature of these effects. Adsorption of hydrophobic pollutants is known to occur in marine plastics (Lee et al., 2014), and studies have shown marine plastics have the ability to transport foreign contaminants to benthic communities, due to pollutant transfer from particle to pore water, becoming available for ingestion by benthic infauna (Graham and Thompson,

2009). This transport mechanism has the potential to increase the number of ecosystems impacted by point source contamination, such as oil spills and harmful algal blooms, to include those otherwise thought to be unaffected. In addition to chemical transport, invasive species can spread by using plastic as a substrate (Barnes, 2002). Laboratory studies have observed a wide range of biological effects from plastic interaction including lowered cellular chlorophyll concentrations and growth rates in the green alga *Scenedesmus obliquus* (Besseling et al., 2014), no observed feeding or developmental effects in the larvae of oyster *Crassostrea gigas* (Cole and Galloway, 2015), severe developmental defects in the embryos of sea urchin *Paracentrotus lividus* (Della Torre et al., 2014), and reduction in both body size and reproduction rate in the crustacean *Daphnia magna* (Besseling et al., 2014). The trophic level transfer of microplastics has been observed through the ingestion of the mussel *Mytilus edulis* by the crab *Carcinus maenas* (Farrell and Nelson, 2013). Further long-term studies on trophic level transfer of these particles are needed to comprehend any risk of bio-magnification of hydrophobic contaminants (Teuten et al., 2007). Ingested plastics have been observed to alter the ballast of fecal pellets (Cole et al., 2016) and phytoplankton aggregates (Long et al., 2015). Sinking rates are either enhanced with plastic densities greater than that of the surrounding material or reduced with those less dense. Whether this phenomenon benefits or hinders the carbon cycle and sequestration is currently unknown. While a potential for harm is established, fibers taken from the marine environment have the potential to act as passive samplers for pollutants present in locations where larger passive sampling techniques are not viable. Ultimately, the plastics reach the benthos where it has been suggested by Goldberg (1997) that the gas exchange between sea water and pore water has the potential to be disrupted due to smothering, resulting in anoxia and hypoxia, theoretically disrupting other water-sediment interactions such as oceanic nutrient cycling (Klump and Martens, 1981).

Whereas general microplastics have a variety of sources including industrial spills of pre-production plastic pellets (Moore et al., 2001), use of cosmetic products (Fendall and Sewell, 2009), and fragmentation of existent marine macroplastics (> 5 mm) (Andrady et al., 1998), it is currently understood that microfibers originate from laundry effluent (Browne et al., 2011). This residential contribution to marine debris is made possible by microfibers shedding from clothing and passing through filters in the waste water treatment process (Browne et al., 2011).

It is generally assumed that plastics float, and therefore remain in the surface oceans and filtered out on beaches, but global studies have proven otherwise (Table 1). While the presence of microplastics in coastal and deep-sea sediments have been studied extensively, the water column has not been surveyed for the flux of sinking particles (Woodall et al., 2014). Some laboratory methods suggest that fibers settle after incorporation into phytoplankton aggregates due to biofouling and turbulence (Long et al., 2015), and marine snow due to ingestion (Cole et al., 2013, 2016). Previous studies performed by Alldredge and Silver (1988) have found marine snow sinking rates to range between 1 – 168 m day^{-1}.

Known densities of fibers found in deep-sea sediments (Table 2) are greater than that in seawater, offering that the fibers sink individually. Factors such as biofouling and the compressibility of the fibers introduce potentials of variance of sinking rate with depth, as biofouling may fluctuate due to grazing, and compressible fibers effectively increase in density as the water pressure rises. Sedimentation of the fibers would vary depending on the sinking rate, with higher

sinking rates depositing fibers closer to the shoreline on the continental shelf or slope than fibers with slower sinking rates, which would reach farther on the abyssal plain (Figure 1). Models suggest that further transport is possible within submarine canyons due to shear force movement and resuspension (Ballent et al., 2013).

Table 1. Global concentration of marine microfibers per 50 mL of sediment collected in previous studies.

Location	Concentration	Sources
Sandy Beach		
UK	0.5	Thompson et al., 2004
Chagos Arch, Indian Ocean	4.5	Readman et al., 2013
Worldwide range	0.4 – 6.2	Browne et al., 2001
Australia	0.4	
Portugal	6.2	
Estuary		
UK	4	Thompson et al., 2004
Subtidal Zone		
UK	6	Thompson et al., 2004
Submarine Canyon		
NE Atlantic, 1400 m	6	Woodall et al., 2014
NE Atlantic, 2000 m	40	
Mediterranean, 300 m	35	
Mediterranean, 1300 m	10	
Continental Slope		
Subpolar N Atlantic, 2000 m	15	Woodall et al., 2014
Subpolar N Atlantic, 1000 m	10	
Mediterranean, 900 m	10	
NE Atlantic, 2200 m	10	
Basin		
Mediterranean, 3500 m	15	Woodall et al., 2014
Abyssal Plain		
NW Pacific, 4870 m	0.0057 (114 m^{-2})	Fischer et al., 2015
NW Pacific, 5412 m	0.00075 (15 m^{-2})	
NW Pacific, 5229 m	0.025 (505 m^{-2})	
Seamount		
SW Indian, 900 m	3.5	Woodall et al., 2014
SW Indian, 1000 m	4	
SW Indian, 900 m	1.4	

Here, three approaches to calculating the sinking rate (W_s) of microfibers collected during June 2016 in the water column of the continental shelf break south of Rhode Island (40°N, 71°W) are presented: theoretical, laboratory-based, and field-based. This first look at how dense microfibers are reaching deep-sea sediments was achieved through the use of polyacrylamide-gel-tube sediment traps deployed for a drift period of three and a half days. Further analysis of collected fibers included the use of microscopy, Fourier

transform infrared (FT-IR) spectrometry, and the image-recognition software ImageJ.

Table 2. Known densities (g cm^{-3}) of cotton and synthetic fibers observed in oceanic sediments (Kolb and Kolb, 1991; Woodall et al., 2014)

Material	Class	Density
Nylon	Plastic	1.15
Acrylic	Plastic	1.18
Polybutylene Terephthalate	Plastic	1.30
Polyethylene Terephthalate (PET)	Plastic	1.39
Rayon	Organic-based synthetic	1.49
Cotton	Organic	1.55

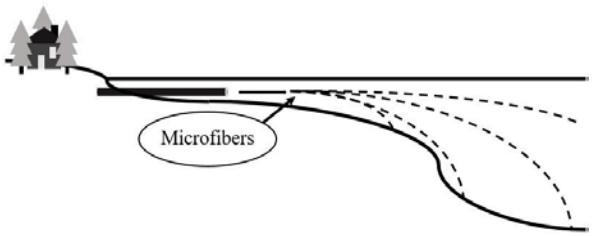

Figure 1. Schematic of sinking-rate-dependent sedimentation of microfibers originating from laundry effluent.

Materials and Methods

Sample collection

An array of cylindrical, Lagrangian surface tethered sediment traps (STSTs) (Figure 2) designed for the collection of marine snow particles (Durkin et al., 2015) was deployed from the R/V *Endeavor* to drift for a period of three and a half days on the continental shelf break south of Rhode Island (40°N, 71°W). Unpublished observation of microfibers in previous deployments suggested these traps were appropriate for microfiber collection. Suitability of existent features and deployment for optimal microfiber collection is tested. Six STSTs used in this study consisted of tubes with removable cup bases filled with roughly 1 cm of polyacrylamide gel. Each tube was filled with filtered seawater before deployment. STSTs were located at 200 m, 150 m, 100 m, and 60 m. Gel cups were removed and capped after recovery to be visually inspected for marine snow and microfibers in a laboratory setting. In addition to an array of four STSTs, each sampling one of these depths, two additional traps were attached to Lagrangian floats within 1 km of the STST array, one located at 150 m on the base of a Scripps Wirewalker vertical profiler, and the second from a neutrally buoyant sediment trap located at 100 m.

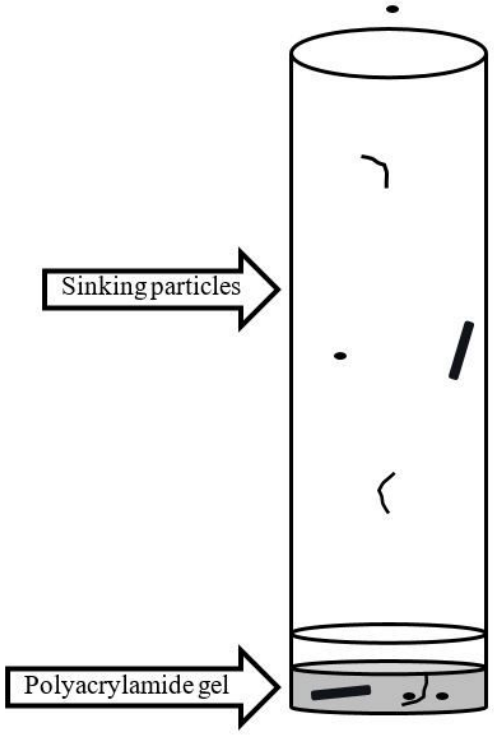

Figure 2. Schematic of a gel-based sediment trap

A CTD (conductivity, temperature, and depth) rosette with twelve Niskin bottles was deployed twice daily near the STST array to collect water samples and characterize the water column temperature and salinity. The particulate organic carbon concentration was measured at a range of depths comparable to those of the STSTs. Volumes of 2-4 L were filtered from depths sampled by Niskin bottles

between 5 – 200 m onto pre-combusted GF/F filters and frozen for later laboratory analysis.

Microfiber characteristics

Based on previous microfiber studies, the following characteristics were utilized to identify microfibers (Norén, 2007; Cole et al., 2011; Mohamed Nor and Obbard, 2014; Woodall et al., 2014): 1. No visible cellular or organic structures; 2. No visible segmentation or appearance resembling a flat, twisted ribbon; 3. Consistent thickness throughout length of fiber with no tapering at either end; 4. Bright and homogenous coloration throughout fiber.

Microfiber analysis

Concentration

The concentration of microfibers in the water column was determined by inspecting particulate organic carbon filters from STST deployment depths with an Olympus SZX16 dissecting microscope paired with an Allied Vision Technologies Stingray camera and dividing counts by the specific volume filtered onboard the R/V *Endeavor*.

Sinking flux

The sinking flux of microfibers was determined through the quantification of microfibers collected in each polyacrylamide-gel cup utilizing a camera paired dissecting microscope (Figure 3). Each microfiber was catalogued in a spreadsheet segmented by gel depth describing color, relative shape and size, and in which focal plane the fiber was located. A 9x9 focal-plane grid labeled vertically by letters and horizontally by numbers was printed on a transparency sheet and placed underneath each gel during inspection. Each focal plane was photographed at 10x magnification for further analysis.

Dimensions

Length and width of each fiber was determined through the use of the image-recognition software ImageJ. The scale was calibrated through photographing a stage micrometer at 10x, 40x, 80x, and 100x magnifications. The captured millimeter was then measured in pixels within ImageJ to determine conversion factors at each magnification. Three fibers were photographed at the same increasing magnifications as the micrometer to determine any bias introduced by pixilation at the general 10x magnification used during visual inspection. An average pixilation bias of 7 μm was observed on each border. Each fiber identified during the initial visual inspection was then measured to determine length and width. The pixilation bias was accounted for by subtracting 14 μm from each measurement.

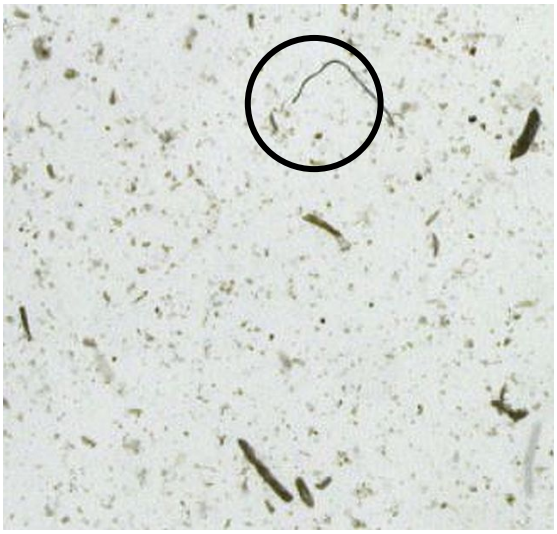

Figure 3. Blue 16 x 1440 μm microfiber (circled, top right) collected at 100 m imaged in polyacrylamide gel. Marine snow particles can be observed throughout image.

Composition

Microfiber composition was determined through the use of a Nicolet Continuum Fourier transform-infrared (FT-IR) spectrometer. A subsample of fibers was extracted from the polyacrylamide gels, consisting of at least one fiber of each color from each gel. Individual fibers were located with the dissecting microscope and identified

by comparing field of view with archived focal plane images. A 250-µL micropipette set to 150 µL was first half-filled with filtered seawater before extracting the fiber and surrounding gel. The fiber, gel, and filtered seawater were then deposited onto an acrylic disk where the excess water and gel were removed, isolating the fiber. Each fiber was attached to a small strip of transparent tape labeled with a number code for FT-IR analysis. The fibers were then analyzed with the FT-IR, collecting spectra in the range of 650 – 4000 cm^{-1} in three locations along each fiber to prevent false spectra due to partial gel or biofilm coverage (Barnes, 2002). The spectra were compared with a library of known spectra of common items, crime lab samples, plasticizers, and polymers to determine each fiber composition and confirmed the presence of polyester (PET) and cotton fibers. False spectra due to polyacrylamide gel interference were common, which calls for future experimentation with fiber isolation ranging from solvents to sediment trap designs excluding the use of gel. A 70% ethanol solution was utilized during the extraction of four fibers in an attempt to remove the gel, instead causing the gel to harden around each of the fibers, further biasing the spectra.

Settling chamber experiments

Laboratory-based observations were obtained by building a custom 19x19x70-mm chamber with 12 mm thick walls out of acrylic. Individual sinking microfibers were filmed in time lapse with an image frequency of 4 s^{-1} with a macro lens fitted iPhone (Figure 4). Microfibers were taken directly from a brightly colored fleece (PET) and shortened to be characteristic of collected fibers (~ 1 mm). Calipers were first used to measure an object of known length, which was placed within the settling chamber to convert recorded length to actual length, and then to measure on-screen sinking distance. The converted sinking distance was combined with the sinking time to determine $W_{s,\,lab}$.

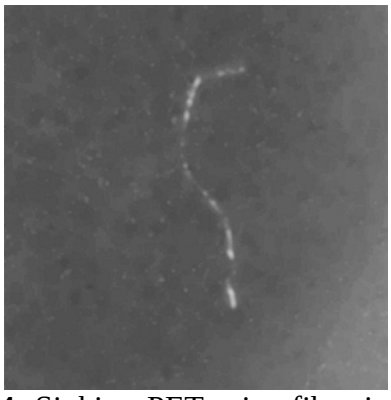

Figure 4. Sinking PET microfiber in settling chamber

Contamination prevention

Two gel blanks were analyzed to determine fill-water and airborne contamination. One tube was treated for deployment, but remained on board to detect the presence of microfibers in the STST fill-water. The second tube did not receive any fill-water and was paired with the gel cup from the 100 m tube. This blank was open to the environment whenever the paired experimental gel cup was exposed to the air during analysis. The blank was visually inspected before and after each air exposure. Clothing worn during each stage with a potential for contamination was 100% cotton, and was not blue due to the high prevalence of this color in fibers found in the sediments (Woodall et al., 2014).

Results

Microfiber collection

A total of 178 fibers were collected from the six sediment traps. Of these fibers, 121 were bright blue. The next two most common colors of microfibers were red (29) and turquoise (19). The blue and red fibers were found at every depth, whereas the turquoise were only observed in gel cups from 150 m and 200 m. Fiber length ranged from 49 – 6900 µm with an average of 1100 ± 1000 µm

(Figure 5). Width ranged from 0.13 – 64 μm with an average of 11 ± 7 μm.

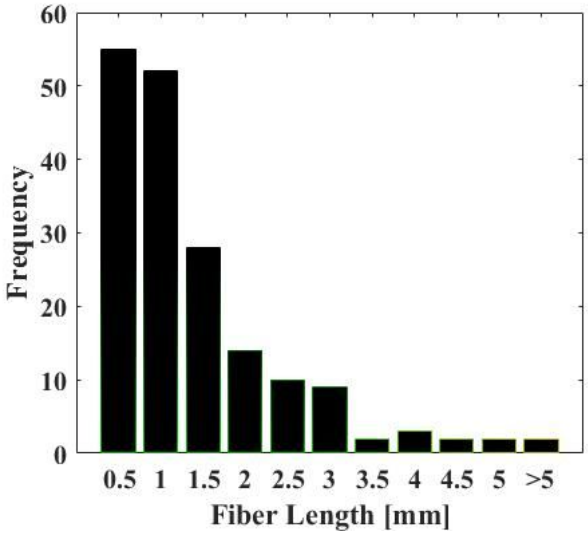

Figure 5. Size distribution of collected fibers. Maximum length shown on x-axis.

Theoretical sinking rate

Stokes Law for a cylindrical particle (Eq. 1), the balance of the gravitational force and drag of a sinking particle, allowed for the prediction of microfiber sinking rates ($W_{s,\ theory}$) (Komar, 1980).

$$W_{s,\ cylinder} = \frac{0.079(\rho_p - \rho_f)L^2 g}{\mu}\left(\frac{L}{D}\right)^{-1.664} \quad (1)$$

Particle length (L), width (D), and density (ρ_p) were used in combination with ambient water density (ρ_f), gravitational acceleration (g), and dynamic viscosity (μ). Dynamic viscosity was calculated as El-Dessouky and Ettouney (2002) described with temperature and salinity values taken from the means of four CTD casts characteristic of the water column during STST deployment. Whereas dynamic viscosity is affected by pressure as well as temperature and salinity, diagnostics performed in Matlab determined that this variable was negligible, thus outside the scope of this study. The theoretical sinking rate was most affected by fiber dimensions. Sinking rate ranges were calculated for fibers with widths 1 – 30 μm and lengths ≤ 5 mm and of either PET or cotton known densities. This resulted in 1 – 100 m day^{-1} (Figure 6) and 1 – 140 m day^{-1}, respectively.

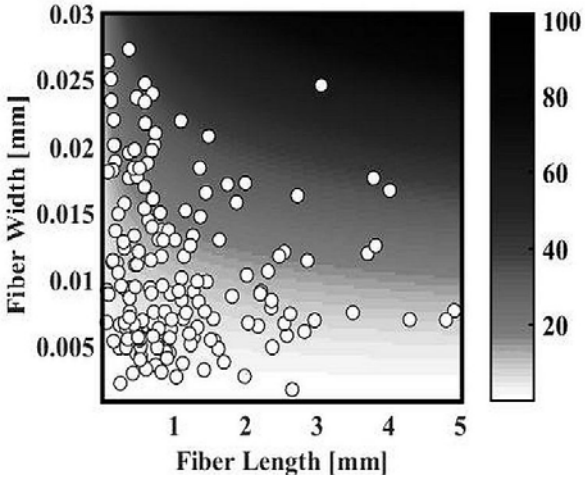

Figure 6. Sinking rate of PET microfibers derived from Stokes Law of a cylindrical particle varied by particle dimension in meters per day. Locations of overlaid white circles show distribution of collected fiber dimensions and predicted sinking rates, $W_{s,\ theory}$.

Applying Stokes Law to the dimensions of the particles collected June 2016 produced an average theoretical sinking rate of $W_{s,\ theory}$ = 12 ± 15 m day^{-1} for PET microfibers (Figure 4) and $W_{s,\ theory}$ = 18 ± 22 m day^{-1} for cotton microfibers. At this rate, it is expected that a PET microfiber with average dimensions based on those collected within this study would reach a depth of 200 m (continental shelf break/slope) in 17 days.

Laboratory-based sinking rate

Laboratory observations with sinking chamber experiments produced a sinking rate of $W_{s,\ lab}$ = 16 ± 4 m day^{-1} for a PET microfiber. Further experimentation is required to determine $W_{s,\ lab}$ of a cotton microfiber. While slight advection within the settling chamber may have enhanced the

sinking rate, the value agrees with the theoretical prediction. At this rate, an average PET microfiber would reach 200 m in roughly 13 days.

Field-based sinking rate

The field-based average sinking rate of $W_{s,\ field} = 2.4 \pm 2.3$ m day^{-1} was determined by dividing the observed sinking flux by the observed concentration. This sinking rate would result in 83 days required for an average PET microfiber to sink 200 m.

Discussion

Sources of bias

While $W_{s,\ lab}$ and $W_{s,\ theory}$ are in general agreement for the collected microfibers, $W_{s,\ field}$ disagrees with these rates. Variance is observed in each sinking rate approach, which is expected based on other flux studies such as that of carbon. However, the 8x difference seen in $W_{s,\ field}$ suggests a bias within the field experiment. This could be due to methodology or environmental factors. $W_{s,\ field}$ predicts an average PET microfiber would take over four hours to sink the distance between the sediment trap opening and the polyacrylamide gel (17 cm) compared to the 50 minutes based on $W_{s,\ theory}$. Increasing the aperture of the trap from the current 7 cm would increase the surface area of the collection column, increasing both the number of particles collected and the sinking flux resolution. Placing multiple sediment traps at each depth would not only increase collection, but also identify any spatial variation, which could be skewing values from single tube collections. Environmental factors may be hindering the microfibers from sinking in ways that are not included within the theoretical calculations or laboratory observations, such as biofouling, which has the potential to increase particle drag.

Sediment trap suitability

Lagrangian platforms are preferred for microfiber collection, as the sediment traps drift with the water mass, removing any bias from water movement, which could be present in stationary, Eulerian sampling methods. The small aperture of 7 cm has the potential to restrict sample size; further experimentation with aperture enlargement is suggested. Due to polyacrylamide-gel interference during FT-IR analysis, sediment traps without gel might be more appropriate for the collection of microfibers. Sediment traps dedicated to microfiber research would be beneficial, as the disruption of gel contents or filter surface would not hinder other studies.

Suggestions for future studies

Increasing sample collection through a variety of suggested techniques discussed above in combination with increasing concentration data would improve the resolution of sinking flux and concentration. This would reveal whether the bias in $W_{s,\ field}$ is methodological. Furthermore, a cleanroom should be used if available to reduce the presence of airborne fibers. Due to the time scale of this study, subsample sizes were restricted for FT-IR analysis; future studies would benefit from larger subsamples. Furthermore, identifying the material of all collected fibers would reveal any material related relationships such as size fractionation or coloration patterns. Experimentation with solvents during fiber extraction would decrease false spectra from polyacrylamide gel interference, which could also be avoided by the use of non-gel-based sediment traps. Filters used in clarification of water samples for microfiber concentration should be explored, with pore sizes small enough to isolate microfibers, but large enough to allow unwanted organic material to flow through during filtration.

Implications of sinking microfibers

It is currently undecided if microfibers are beneficial, harmful, or neutral within the marine environment. Studies are underway, but further research both in the laboratory and in the field is required to determine the nature of these particles, which are both abundant and widespread in the global oceans. Understanding the sinking rates of microfibers may lead to understanding the mechanics of sedimentation patterns. Models predicting the location of marine microfibers in the water column or sediments would allow for scientists to target study areas to best fit their research including in situ ingestion, inhibition of pore water processes, or toxin transfer.

Conclusions

Sinking microfibers were quantified in the water column for the first time. Sinking rates determined through theory, laboratory experiments, and field observations average 12 ± 15, 16 ± 4, and 2.4 ± 2.3 m day^{-1}, respectively. Further studies regarding regional composition, distribution, and refining of sinking rate models are suggested in addition to those regarding biological and ecological effects.

Acknowledgments. This study was supported by a Summer Undergraduate Research Fellowship in Oceanography (SURFO) (National Science Foundation REU grant # OCE-1460819). We thank Captain Rhett McMunn and the crew on board the R/V *Endeavor* for a safe research cruise; Meg Estapa and Pat Kelly for access to their samples; Katie Kelley, Susanne Menden-Deuer, and Rodrigue Spinette for granting us access to their labs and equipment; and Kim Carey, Kathy Donohue, Lucie Maranda, and David Smith for their guidance and organization within the SURFO program.

References

Alldredge, A. L., and M. W. Silver (1988), Characteristics, dynamics and significance of marine snow, *Progress in Oceanography*, *20*(1), 41–82, doi:10.1016/0079-6611(88)90053-5.

Andrady, A. L., S. H. Hamid, X. Hu, and A. Torikai (1998), Effects of increased solar ultraviolet radiation on materials, *Journal of Photochemistry and Photobiology B: Biology*, *46*(1), 96–103, doi:10.1016/S1011-1344(98)00188-2.

Ballent, A., S. Pando, A. Purser, M. F. Juliano, and L. Thomsen (2013), Modelled transport of benthic marine microplastic pollution in the Nazare Canyon, *Biogeosciences*, *10*(12), 7957, doi:http://dx.doi.org/10.5194/bg-10-7957-2013.

Barnes, D. K. A. (2002), Biodiversity: Invasions by marine life on plastic debris, *Nature*, *416*(6883), 808–809, doi:10.1038/416808a.

Barnes, D. K. A., F. Galgani, R. C. Thompson, and M. Barlaz (2009), Accumulation and fragmentation of plastic debris in global environments, *Philosophical Transactions of the Royal Society B: Biological Sciences*, *364*(1526), 1985–1998, doi:10.1098/rstb.2008.0205.

Besseling, E., B. Wang, M. Lürling, and A. A. Koelmans (2014), Nanoplastic affects growth of S. obliquus and reproduction of D. magna, *Environmental Science & Technology*, *48*(20), 12336–12343, doi:10.1021/es503001d.

Browne, M. A., P. Crump, S. J. Niven, E. Teuten, A. Tonkin, T. Galloway, and R. Thompson (2011), Accumulation of Microplastic on Shorelines Woldwide: Sources and Sinks, *Environ. Sci. Technol.*, *45*(21), 9175–9179, doi:10.1021/es201811s.

Castañeda, R. A., S. Avlijas, M. A. Simard, and A. Ricciardi (2014), Microplastic pollution in St. Lawrence River sediments, *Can. J. Fish. Aquat. Sci.*, *71*(12), 1767–1771, doi:10.1139/cjfas-2014-0281.

Cole, M., and T. S. Galloway (2015), Ingestion of nanoplastics and microplastics

by pacific oyster larvae, *Environmental Science & Technology*, *49*(24), 14625–14632, doi:10.1021/acs.est.5b04099.

Cole, M., P. Lindeque, C. Halsband, and T. S. Galloway (2011), Microplastics as contaminants in the marine environment: A review, *Marine Pollution Bulletin*, *62*(12), 2588–2597, doi:10.1016/j.marpolbul.2011.09.025.

Cole, M., P. Lindeque, E. Fileman, C. Halsband, R. Goodhead, J. Moger, and T. S. Galloway (2013), Microplastic ingestion by zooplankton, *Environmental Science & Technology*, *47*(12), 6646–6655, doi:10.1021/es400663f.

Cole, M., P. K. Lindeque, E. Fileman, J. Clark, C. Lewis, C. Halsband, and T. S. Galloway (2016), Microplastics alter the properties and sinking rates of zooplankton faecal pellets, *Environmental Science & Technology*, *50*, 3239–3246, doi:10.1021/acs.est.5b05905.

Collignon, A., J.-H. Hecq, F. Glagani, P. Voisin, F. Collard, and A. Goffart (2012), Neustonic microplastic and zooplankton in the North Western Mediterranean Sea, *Marine Pollution Bulletin*, *64*(4), 861–864, doi:10.1016/j.marpolbul.2012.01.011.

Della Torre, C., E. Bergami, A. Salvati, C. Faleri, P. Cirino, K. A. Dawson, and I. Corsi (2014), Accumulation and Embryotoxicity of Polystyrene Nanoparticles at Early Stage of Development of Sea Urchin Embryos Paracentrotus lividus, *Environmental Science & Technology*, *48*(20), 12302–12311, doi:10.1021/es502569w.

Durkin, C. A., M. L. Estapa, and K. O. Buesseler (2015), Observations of carbon export by small sinking particles in the upper mesopelagic, *Marine Chemistry*, *175*, 72–81, doi:10.1016/j.marchem.2015.02.011.

El-Dessouky, H. T., and H. M. Ettouney (2002), *Fundamentals of Salt Water Desalination (Appendix A: Thermodynamic Properties)*, Elsevier.

Eriksen, M., L. C. M. Lebreton, H. S. Carson, M. Thiel, C. J. Moore, J. C. Borerro, F. Galgani, P. G. Ryan, and J. Reisser (2014), Plastic Pollution in the World's Oceans: More than 5 Trillion Plastic Pieces Weighing over 250,000 Tons Afloat at Sea, *PLOS ONE*, *9*(12), e111913, doi:10.1371/journal.pone.0111913.

Farrell, P., and K. Nelson (2013), Trophic level transfer of microplastic: Mytilus edulis (L.) to Carcinus maenas (L.), *Environmental Pollution*, *177*, 1–3, doi:10.1016/j.envpol.2013.01.046.

Fendall, L. S., and M. A. Sewell (2009), Contributing to marine pollution by washing your face: Microplastics in facial cleansers, *Marine Pollution Bulletin*, *58*(8), 1225–1228, doi:10.1016/j.marpolbul.2009.04.025.

Fischer, V., N. O. Elsner, N. Brenke, E. Schwabe, and A. Brandt (2015), Plastic pollution of the Kuril–Kamchatka Trench area (NW pacific), *Deep Sea Research Part II: Topical Studies in Oceanography*, *111*, 399–405, doi:10.1016/j.dsr2.2014.08.012.

Free, C. M., O. P. Jensen, S. A. Mason, M. Eriksen, N. J. Williamson, and B. Boldgiv (2014), High-levels of microplastic pollution in a large, remote, mountain lake, *Marine Pollution Bulletin*, *85*(1), 156–163, doi:10.1016/j.marpolbul.2014.06.001.

Goldberg, E. D. (1997), Plasticizing the Seafloor: An Overview, *Environmental Technology*, *18*(2), 195–201, doi:10.1080/09593331808616527.

Graham, E. R., and J. T. Thompson (2009), Deposit- and suspension-feeding sea cucumbers (Echinodermata) ingest plastic fragments, *Journal of Experimental Marine Biology and Ecology*, *368*(1), 22–29, doi:10.1016/j.jembe.2008.09.007.

Imhof, H. K., N. P. Ivleva, J. Schmid, R. Niessner, and C. Laforsch (2013), Contamination of beach sediments of a subalpine lake with microplastic particles, *Current Biology*, *23*(19), R867–R868, doi:10.1016/j.cub.2013.09.001.

Klump, J. V., and C. S. Martens (1981), Biogeochemical cycling in an organic rich coastal marine basin—II. Nutrient sediment-water exchange processes, *Geochimica et Cosmochimica Acta*, *45*(1), 101–121, doi:10.1016/0016-7037(81)90267-2.

Kolb, K. E., and D. K. Kolb (1991), Method for separating or identifying plastics, *J. Chem. Educ.*, *68*(4), 348, doi:10.1021/ed068p348.

Komar, P. D. (1980), Settling Velocities of Circular Cylinders at Low Reynolds Numbers, *The Journal of Geology*, *88*(3), 327–336, doi:10.1086/628510.

Law, K. L., S. Morét-Ferguson, N. A. Maximenko, G. Proskurowski, E. E. Peacock, J. Hafner, and C. M. Reddy (2010), Plastic Accumulation in the North Atlantic Subtropical Gyre, *Science*, *329*(5996), 1185–1188, doi:10.1126/science.1192321.

Lee, H., W. J. Shim, and J.-H. Kwon (2014), Sorption capacity of plastic debris for hydrophobic organic chemicals, *Science of The Total Environment*, *470–471*, 1545–1552, doi:10.1016/j.scitotenv.2013.08.023.

Long, M., B. Moriceau, M. Gallinari, C. Lambert, A. Huvet, J. Raffray, and P. Soudant (2015), Interactions between microplastics and phytoplankton aggregates: Impact on their respective fates, *Marine Chemistry*, *175*, 39–46, doi:10.1016/j.marchem.2015.04.003.

Mohamed Nor, N. H., and J. P. Obbard (2014), Microplastics in Singapore's coastal mangrove ecosystems, *Marine Pollution Bulletin*, *79*(1–2), 278–283, doi:10.1016/j.marpolbul.2013.11.025.

Moore, S. L., D. Gregorio, M. Carreon, S. B. Weisberg, and M. K. Leecaster (2001), Composition and Distribution of Beach Debris in Orange County, California, *Marine Pollution Bulletin*, *42*(3), 241–245, doi:10.1016/S0025-326X(00)00148-X.

Norén, F. (2007), Small plastic particles in coastal Swedish waters, *KIMO Sweden*.

Obbard, R. W., S. Sadri, Y. Q. Wong, A. A. Khitun, I. Baker, and R. C. Thompson (2014), Global warming releases microplastic legacy frozen in Arctic Sea ice, *Earth's Future*, *2*(6), 2014EF000240, doi:10.1002/2014EF000240.

Readman, J. W. et al. (2013), Contaminants, Pollution and Potential Anthropogenic Impacts in Chagos/BIOT, in *Coral Reefs of the United Kingdom Overseas Territories*, edited by C. R. C. Sheppard, pp. 283–298, Springer Netherlands.

Reisser, J., J. Shaw, C. Wilcox, B. D. Hardesty, M. Proietti, M. Thums, and C. Pattiaratchi (2013), Marine Plastic Pollution in Waters around Australia: Characteristics, Concentrations, and Pathways, *PLOS ONE*, *8*(11), e80466, doi:10.1371/journal.pone.0080466.

Teuten, E. L., S. J. Rowland, T. S. Galloway, and R. C. Thompson (2007), Potential for Plastics to Transport Hydrophobic Contaminants, *Environ. Sci. Technol.*, *41*(22), 7759–7764, doi:10.1021/es071737s.

Thompson, R. C., Y. Olsen, R. P. Mitchell, A. Davis, S. J. Rowland, A. W. G. John, D. McGonigle, and A. E. Russell (2004), Lost at sea: where is all the plastic?, *Science*, *304*, doi:10.1126/science.1094559.

Van Cauwenberghe, L., A. Vanreusel, J. Mees, and C. R. Janssen (2013), Microplastic pollution in deep-sea sediments, *Environ Pollut*, *182*, doi:10.1016/j.envpol.2013.08.013.

Wagner, M. et al. (2014), Microplastics in freshwater ecosystems: what we know and what we need to know, *Environmental Sciences Europe*, *26*(1), 1–9, doi:10.1186/s12302-014-0012-7.

Woodall, L. C., A. Sanchez-Vidal, M. Canals, G. L. J. Paterson, R. Coppock, V. Sleight, A. Calafat, A. D. Rogers, B. E. Narayanaswamy, and R. C. Thompson (2014), The deep sea is a major sink for microplastic debris, *Royal Society Open*

Science, *1*(4), 140317, doi:10.1098/rsos.140317.

Key Points:

- Midwater column presence of microfibers confirmed
- Both synthetic and organic fibers observed
- Predicted and observed sinking rates compared

Key Index Words: Anthropogenic; Atlantic Ocean; Marine debris; Microplastic; Sinking; Water column

Assessing the effect of copepod excretions on the growth and ingestion rate of the phagotrophic protist *Oxyrrhis marina*

Elizabeth Wright-Fairbanks[1,2], Andreas Oikonomou[1], and Susanne Menden-Deuer[1]
[1]Graduate School of Oceanography, University of Rhode Island, Narragansett, RI, USA
[2]Middlebury College, Middlebury, Vermont, USA

Abstract
The contribution of microbial organisms to the primary production of the world's oceans has received a great deal of attention over the last decades. There is still a need to develop our understanding of contributions by heterotrophic microzooplankton, which consume approximately two-thirds of daily picoplankton production and play an intermediary trophic role by transferring organic matter to mesozooplankton such as copepods. Copepods are known predators of *Oxyrrhis marina*, which successfully feeds on *Isochrysis galbana*, a microalga. *Oxyrrhis marina* was used as a model for the diverse group of heterotrophic protists, which are known to be sensitive to chemical signals produced by their predators and prey. Cultures of *O. marina* were grown on five concentrations of *I. galbana* and exposed to three concentrations of ammonium, the main excretory product of copepods. Based on published estimates of copepod abundances and excretion rates, ammonium treatments were categorized as low (15 ng $NH_4^+ L^{-1}$), medium (744 ng $NH_4^+ L^{-1}$), and high (3955 μg $NH_4^+ L^{-1}$). Measuring changes in population sizes of *O. marina* and *I. galbana*, we found that *Oxyrrhis* exposed to the high ammonium treatment exhibited lower growth rates than the no-ammonium control at both 24 and 48 hours, while a lag in ingestion rate was observed at 24 hours that wore off at 48 hours. Overall, results showed that ammonium affects *O. marina* growth and ingestion on *I. galbana* only at high concentrations, indicating that dense localized copepod aggregations could have a negative effect on heterotrophic flagellates.

Microzooplankton grazers (20-200 µm) play a dominant role in consuming autotrophic picoplankton (0.2-2 µm) which form the basis of aquatic food webs (Barber, 2007; Fenchel, 1987). Heterotrophic protists may graze on 60-75% of phytoplankton biomass, making them the main source of autotroph mortality in the oceans (Calbet & Landry 2004). These protistan assemblages play an important role in transferring organic carbon and energy to larger mesozooplankton and subsequently to higher trophic levels in the oceanic carbon cycle.

This complex set of ecosystem-level trophic interactions creates a gap in our understanding of oceanic food webs. Chemical signaling plays a pivotal role in these microbial interactions; it has been seen that protists have a keen ability to "smell" (Wolfe, 2000; Roberts et al., 2011). One chemical used in signaling, nitrogen, is excreted in many forms by a multitude of organisms, including marine mesozooplankton grazers such as copepods. Copepods are primarily ammonotelic animals, meaning their main excretory product is ammonium (Gardner and Paffenhofer, 1982). Excretions of mesozooplankton grazers can indirectly affect the physiological activity of bacteria and phytoplankton (Carman, 1994; Meunier, 2015). However, very little is known about how excretions in the form of ammonium (NH_4^+) released by planktonic copepods can affect the growth and ingestion rates of

heterotrophic protists. It is important to quantify protistan-copepod relationships in order to include them in computer-based oceanic models to more accurately predict how changes in the ocean affect carbon cycling and population dynamics.

In the present study, we tested the consequences of copepod excretions on the growth and ingestion of *Oxyrrhis marina* as a function of concentration of their prey, *Isochrysis galbana*. *Oxyrrhis marina*, a single-celled heterotrophic dinoflagellate, is known to react to various environmental chemical cues and has been observed exhibiting chemotaxis, a physical response to changes in chemical abundance (Martel, 2006; Boakes 2011). Chemotaxis is often seen as a positive response to the presence of prey, guiding *O. marina* in its grazing (Martel, 2010; Roberts et al., 2011). However, *O. marina* exposed to saturating amounts of nitrogen-stressed *I. galbana* exhibit cannibalism as opposed to feeding on the microalga (Martel, 2006; Roberts et al., 2010). Based on the negative chemotaxis seen from *O. marina* in response to N-saturated *I. galbana*, we hypothesize that *O. marina* exhibits negative chemotaxis when exposed to high levels of ammonium, the excretory product of their predators.

Materials and Methods

Culture maintenance

Clonal cultures of the heterotrophic dinoflagellate species *Oxyrrhis marina* (SPMC 107) were used as predator stocks for the growth and grazing experiments. Cultures of *O. marina* were maintained in 2-liter polycarbonate bottles and exposed to 10 μmol photons m^{-2} s^{-1} on a 12:12 light:dark cycle at 14.5 °C. *Oxyrrhis marina*, fed daily with prey culture of *Isochrysis galbana* (CCMP 1323), were grown to a concentration of ca. 3,000 cells mL^{-1} and refreshed with filtered seawater weekly. The prymnesiophyte *I. galbana* was cultured in f/2-Si medium and transferred every 3-4 days to maintain exponential growth (Guillard, 1975). The prey cultures were maintained in 450 mL polycarbonate bottles on a 12:12 light:dark cycle of 80-100 μmol photons m^{-2} s^{-1} at 14.5 °C. The filtered seawater (31.98 psu) used for predator and prey cultures was collected from the Narragansett Bay at high tide (June 22, 2016), prescreened through a 0.2-μm filter cartridge and sterilized at 121 °C for 40 minutes. Prior to the experiments, *O. marina* was grown to a population density of 3,366 cells mL^{-1} and *I. galbana* abundance in the heterotrophic predator cultures was 1,088 cells mL^{-1}.

Mimicking copepod excretions

Ammonium (NH_4^+) constitutes 50 to 90% of the total nitrogen excreted by zooplankton, thus ammonium additions provide a realistic proxy for copepod excretions (Checkley et al., 1992; Frangoulis et al., 2007). Ammonium treatments were determined based on available literature outlining both ammonium excretion rates by copepods expressed per individual per time and copepod abundances. Final NH_4^+ treatments were categorized as low (15 ng NH_4^+ L^{-1}), medium (744 ng NH_4^+ L^{-1}), and high (3955 μg NH_4^+ L^{-1}). The low treatment estimate was based on an excretion rate of 6.2 ng NH_4^+ $copepod^{-1}$ h^{-1} (Checkley et al., 1992) and a minimum copepod abundance of 0.1 copepods L^{-1} (Durbin & Durbin, 1981). The medium ammonium treatment was meant to resemble the natural biology of Narragansett Bay and was based on an excretion rate of 6.2 ng NH_4^+ $copepod^{-1}$ h^{-1} (Checkley et al., 1992) and an average abundance of *Acartia tonsa* in Narragansett Bay, 5 copepods L^{-1} (Durbin & Durbin, 1981). The species *A. tonsa* was used because it is a dominant mesozooplankton grazer in Narragansett Bay (Deason, 1980). The high ammonium treatment concentration was based on an excretion rate of 257.5 ng NH_4^+ $copepod^{-1}$ h^{-1} (Verity, 1985) and a maximum abundance of 640 copepods L^{-1}, as seen in monospecific copepod swarms measured by net tows (Hamner & Carleton,

1979). Ammonium was added as ammonium chloride (NH_4Cl) solution in a single pulse representing copepod excretion over a period of 24 hours.

Experimental Design and Rate Measurements

For each ammonium treatment, incubation experiments were performed along a gradient of five prey concentrations ranging from 1000 cells *I. galbana* mL^{-1} to 200,000 *cells I. galbana* mL^{-1}. Initial predator abundance was 800 cells *O. marina* mL^{-1} for every prey concentration and ammonium treatment. In order to account for growth of *I. galbana* in the absence of its predator, control bottles with 50,000 cells *I. galbana* mL^{-1} and no *O. marina* were tested at each NH_4^+ treatment. At each prey concentration, additional control bottles were treated with deionized water instead of NH_4^+ to ensure that physical disturbance caused by the addition of NH_4^+ was not the cause of any change in *O. marina* growth or ingestion. Each treatment was tested in duplicate to account for measurement errors, for a total of 48 experimental bottles.

Population sizes of *I. galbana* and *O. marina* in each incubation bottle were measured using a Multisizer TM3 Coulter Counter® (version 3.53, Beckman Coulter, USA). Measurements were taken at 0, 24, and 48 hours. Growth rate (μ d^{-1}) of *O. marina* was measured in each incubation bottle at 24 and 48 hours using the equation

$$\mu = [\ln(C_f/C_0)]/\Delta t \quad (1)$$

where C_0 and C_f represent the concentration of *O.marina* cells at the beginning and end of the experiment, and Δt is the difference in incubation time in days.

Clearance and ingestion rates were calculated using the methods of Frost (1972) and Heinbokel (1978) to account for changes in predator growth. Specifically, clearance rate (F) of *O. marina*, expressed as volume cleared per predator per day, was measured as

$$F = V \times (g/n) \quad (2)$$

where V is the volume of the incubation vessel, g is the instantaneous feeding coefficient and n is the adjusted absolute predator population during the incubation experiment (Heinbokel, 1978). Daily ingestion rate (I) of *O. marina*, expressed as cells of *I. galbana* consumed $predator^{-1}$ day^{-1}, was calculated at 24 and 48 hours

$$I = F \times [C] \quad (3)$$

where F is the clearance rate and [C] is the mean prey concentration (Frost, 1972). All statistical analyses were performed using the IBM® SPSS® Statistics Developer 23.0.

Results

Oxyrrhis marina showed positive specific growth rates at all ammonium treatments and concentrations of *I. galbana*. There was no significant difference seen in the growth rates of predator-free prey growth controls ($p=0.999$), so prey growth was not a confounding variable in this experiment. Variations in growth and grazing rates were observed among the three ammonium treatments over our 48-hour incubation experiments.

Ingestion Rate

At 24 hours, there was a sharp decrease in *O. marina* ingestion rate at the highest prey concentration for all ammonium treatments, with the most extreme decline seen in the high ammonium treatment (Fig. 1). *Oxyrrhis marina* exposed to this experimental treatment had a significantly lower ingestion rate than those exposed to low, medium, or control ammonium treatments ($p=0.000$, 2-way ANOVA), suggesting a collaborative effect of high prey abundance and high ammonium concentration.

At 48 hours, *O. marina* in the high ammonium treatment had a significantly

higher ingestion rate than the low, medium, and control ammonium treatments at every prey concentration (p=0.000, 2-way ANOVA, Fig. 2).

Growth Rate

There was no significant difference in *O. marina* growth rate among ammonium treatments at 24 hours (p=0.261, 2-way ANOVA, Fig. 3) or at 48 hours (p=0.138, 2-way ANOVA, Fig, 4). A general trend was observed where *O. marina* in the high ammonium treatment exhibited lower growth rates than the control treatment throughout the course of the experiment, while those in the low and medium treatment groups appeared to have more positive growth rate values over time (Fig. 3 and Fig. 4).

Discussion

Ingestion Rate

At 24 hours, *Oxyrrhis marina* exhibited an expected pattern of increasing ingestion rate with increasing prey concentration up until the high prey treatment. At the high prey concentration, *O. marina* exposed to the combination of high ammonium and high prey treatments displayed a noticeably lower ingestion rate than the other three ammonium treatments. This pattern points to a distinct stress accompanying the high prey/high ammonium treatment. It has been shown that the ingestion rates of some heterotrophic protists are negatively affected when exposed to high prey concentrations due to mechanical interference with feeding (Montagnes & Lessard, 1999; Calbet et al., 2013). Thus, it is possible that the overloading of inhibitory chemicals and prey may have had a similar effect on *O. marina* in our incubation experiments. At 48 hours, the decline in ingestion rate observed in the high prey/high ammonium treatment disappeared and the values became positive. This could be due to the removal of excess ammonium from the system by bacteria or *I. galbana*, which in turn removed stress from *O. marina* and allowed them to begin grazing more normally. In the future, to confirm that ammonium is being removed from the system, we suggest measuring ammonium content in the incubation bottles over time.

Growth Rate

Growth rate of *O. marina* varied among ammonium treatments and prey concentrations. Generally, *O. marina* exhibited lower growth rates at 24 hours at the three highest prey concentrations, independent of ammonium treatment. At 48 hours, the growth rates of *O. marina* in the low and medium ammonium treatments increased compared to the same treatments at 24 hours, while those of the high ammonium treatment group remained low. A consistently lower growth rate in the high ammonium treatment than the control treatment points to stress caused by the presence of high ammonium concentrations.

Stress Response

In the high ammonium treatment, ingestion rate dropped off significantly at the high prey concentration at 24 hours, but rebounded by 48 hours. The initial lag in ingestion rate wore off after 24 hours, but growth rate did not follow the same trend, remaining low throughout the experiment. A possible explanation to the observation is that at 48 hours, *O. marina* in the high ammonium treatment was grazing efficiently but the cells were not reproducing.

This result points to a stress response by *O. marina*. When exposed to the stress of high ammonium and high prey concentration, *O. marina* cells initially ceased to graze and therefore reproduced less. After that stress was removed from the system, *O. marina* cells began to feed again at high grazing rates, but did not reach maximum growth. We speculate that after the stress factor was removed, *O. marina* acquired carbon and energy to expand

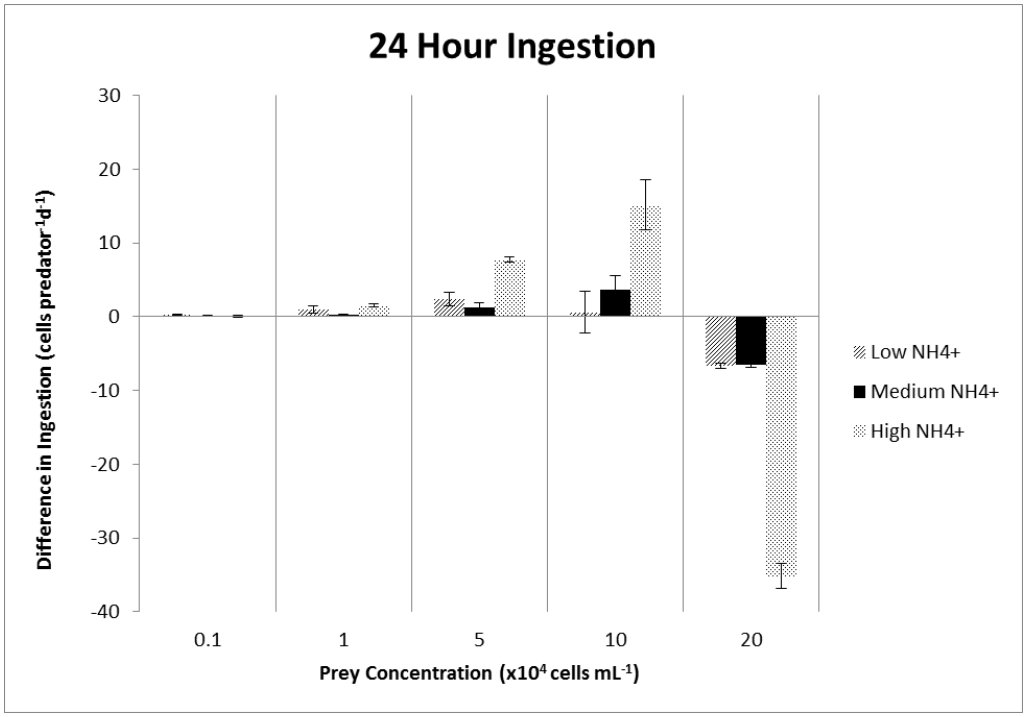

Figure 1. Ingestion rates of *Oxyrrhis marina* on *Isochrysis galbana* at 24 hours. Values shown are the mean difference in ingestion rates between *O. marina* exposed to the ammonium treatments and *O. marina* in the no-ammonium control treatment +/- 1 SE.

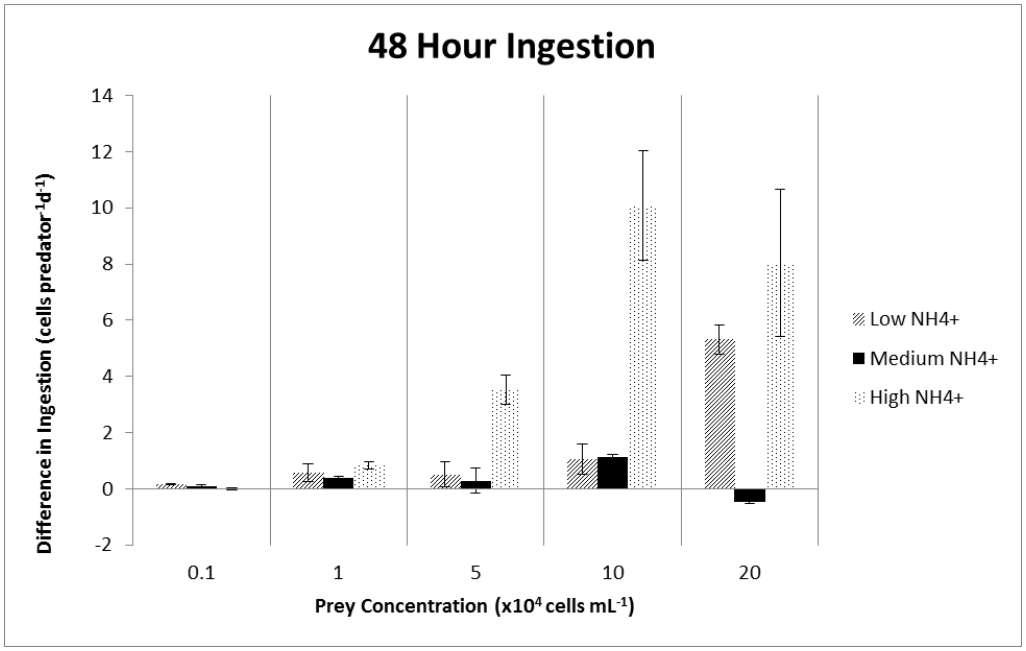

Figure 2. Ingestion rates of *Oxyrrhis marina* on *Isochrysis galbana* at 48 hours. Values shown are the mean difference in ingestion rates between *O. marina* exposed to the ammonium treatments and *O. marina* in the no-ammonium control treatment +/- 1 SE.

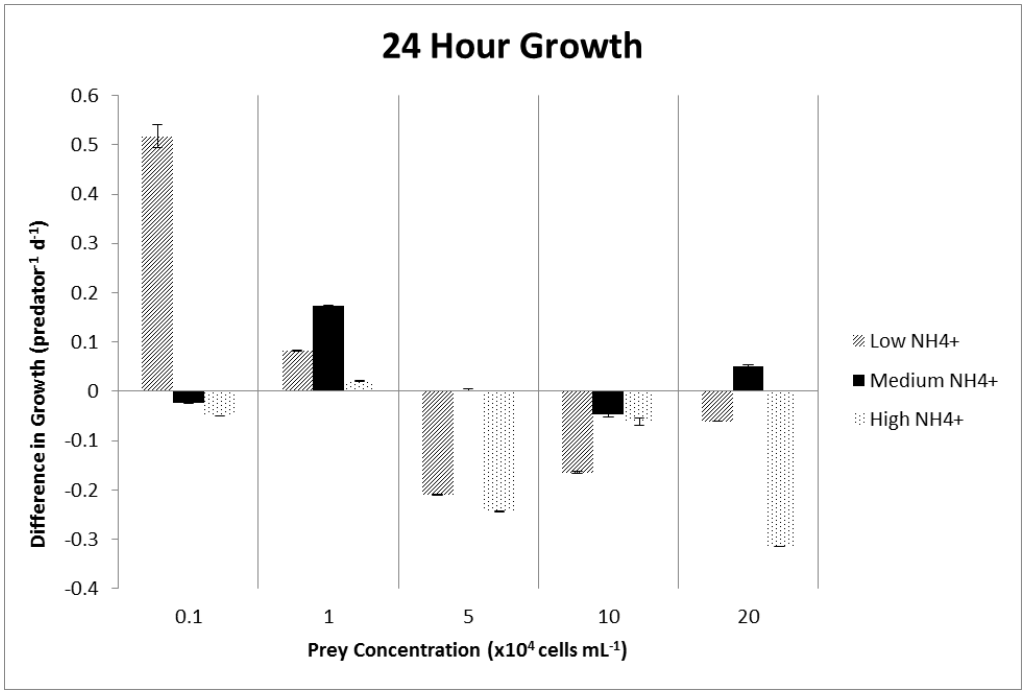

Figure 3: Growth rates of *Oxyrrhis marina* on *Isochrysis galbana* at 24 hours. Values shown are the mean difference in growth rates between *O. marina* exposed to the ammonium treatments and *O. marina* in the no-ammonium control treatment +/- 1 SE.

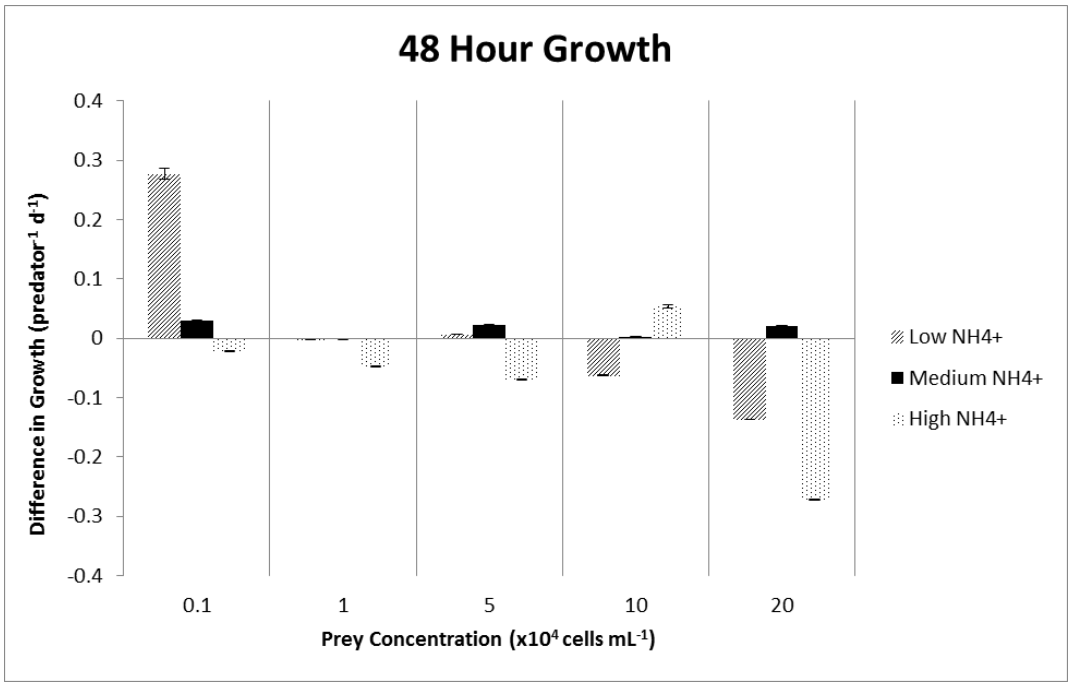

Figure 4. Growth rates of *Oxyrrhis marina* on *Isochrysis galbana* at 48 hours. Values shown are the mean difference in growth rates between *O. marina* exposed to the ammonium treatments and *O. marina* in the no-ammonium control treatment +/- 1 SE.

in volume as opposed to using it to reproduce. In order to confirm this idea, carbon biomass should be measured throughout the course of future experiments. An increase in biomass when population growth rates are still low would confirm that *O. marina* are utilizing the energy they acquire to expand in volume instead of in number.

Implications for ecosystem

When applied to a larger ecosystem scale, our results suggest potential changes in behavior of heterotrophic protists when subjected to monospecific copepod swarms. The initial increase in ammonium that comes about as such swarms aggregate in the ocean likely would alter the grazing efficiency and growth of protists, specifically those feeding on dense phytoplankton layers. The subsequent trophic cascade would release predation pressure on phytoplankton, allowing for an increase in phytoplankton abundance and the potential formation of a phytoplankton bloom.

Though it is important to apply our results to the ecosystem level, we understand the shortcomings of laboratory-derived experiments. Changes in mesozooplankton metabolic activity based on temperature, mesozooplankton species composition, and their complex life cycles are factors that influence copepod excretion rates and should be considered before extrapolation (Checkley et al., 1992; Durbin & Durbin, 1981; Hamner & Carleton, 1979).

Conclusion

Our results show that the ammonium excreted by copepods has an instantaneous negative effect on *Oxyrrhis marina* ingestion of and growth on *Isochrysis galbana* at dense monospecific copepod swarm abundances.

Acknowledgments. This research was supported by a Summer Undergraduate Research Fellowship in Oceanography (SURFO) National Science Foundation REU grant #OCE-1460819. We thank the University of Rhode Island Graduate School of Oceanography for their guidance in this research.

References

Barber, Richard T. 2007. “Picoplankton Do Some Heavy Lifting” *Science* 315: 777–78.

Boakes, D.E., E.A. Codling, G.J. Thorn, and M. Steinke. 2010. Analysis and modeling of swimming behaviour in *Oxyrrhis marina*. *Journal of Plankton Research* 33*:* 641–649.

Calbet, Albert, Stamatina Isari, Rodrigo Andrea Martinez, Enric Saiz, Susana Garrido, Janna Peters, Rosa Maria Borrat, and Miquel Alcaraz. 2013. Adaptations to feast and famine in different strains of the marine heterotrophic dinoflagellates *Gyrodinium dominans* and *Oxyrrhis marina*. *Mar Ecol Prog Ser*. 483:67-84.

Calbet, Albert, and Michael R. Landry. 2004. “Phytoplankton Growth, Microzooplankton Grazing, and Carbon Cycling in Marine Systems” *Limnology and Oceanography* 49 (1): 51–57.

Carman, K.R. 1994. Stimulation of marine free-living and epibiotic bacterial activity by copepod excretions. *FEMS Microbiology Ecology* 14(3): 255-261.

Checkley, David M., Michael J. Dagg, and Shin-ichi Uye. 1992. Feeding, Excretion and Egg Production by Individuals and Populations of the Marine, Planktonic Copepods, *Acartia* spp. and *Centropages furcatus*. *Journal of Plankton Research* 14 (1): 71–96.

Deason, EE. 1980. Grazing of *Acartia hudsonica* (*A. clausi*) on *Skeletonema costatum* in Narragansett Bay (USA): influence of food concentration and temperature. *Mar Biol* 60:101-113.

Durbin, A. G., and E. G. Durbin. 1981. Standing Stock and Estimated Production Rates of Phytoplankton and Zooplankton in

Narragansett Bay, Rhode Island. *Estuaries* 4 (1): 24–41.

Fenchel, T. 1987. *Ecology of Protozoa: The Biology of Free-living Phagotrophic Prolists.* Science Technical Publishers, Madison, WI.

Frangoulis, C., E.D. Christou and J. H. Hecq. 2005. Comparison of marine copepod outfluxes: Nature, rate, fate and role in the carbon and nitrogen cycles. *Advances in Marine Biology* 47:254-309.

Frost, B. W. 1972. Effects of size and concentration of food particles on the feeding behavior of the marine planktonic copepod *Calanus pacificus*. *Limnol. Oceanogr.*, 17:805-815.

Gardner, Wayne S. and Gustav A. Paffenhofer. 1982. Nitrogen regeneration by the subtropical marine copepod *Eucalanus pileatus*. *Journal of Plankton Research* 4 (3):725-734.

Guillard, R. R. 1975. Culture of phytoplankton for feeding marine invertebrates. *Culture of marine invertebrate animals* p. 29-60.

Hamner, W. M., and J. H. Carleton. 1979. "Copepod Swarms: Attributes and Role in Coral Reef Ecosystems" *Journal of Limnology and Oceanography* 24 (1): 1–14.

Heinbokel, J. F. 1978. Studies on the functional role of tintinnids in the Southern California Bight. II. Grazing rates of field populations. *Mar. Biol.*, 47:191-197.

Martel, Claire M. 2006. Prey Location, Recognition and Ingestion by the Phagotrophic Marine Dinoflagellate *Oxyrrhis marina*. *Journal of Experimental Marine Biology and Ecology* 335: 210–20.

Martel, Claire M. 2010. "Regenerated Extracellular NH4+ Affects the Motile Chemosensory Responses of Batch-Cultures *Oxyrrhis marina*" *Brazilian Journal of Microbiology* 41: 321–28.

Meunier, C.L, M. Boersma,K.H. Wiltshire, A.M. Malzahn. 2015. Zooplankton eat what they need: copepod selective feeding and potential consequences for marine systems. *Oikos* 125(1):50-58.

Montagnes, DJS and EJ Lessard. 1999. Population dynamics of marine planktonic ciliate *Strombidinopsis multiauris*: its potential to control phytoplankton blooms. *Aquat Microb Ecol* 20:167–181.

Roberts, Emily C., Catherine Legrand, Michael Steinke, and Emma C. Wootton. 2011. "Mechanisms Underlying Chemical Interactions between Predatory Planktonic Protists and Their Prey" *Journal of Plankton Research* 0 (0): 1–9.

Roberts, Emily C., Emma C. Wootton, Keith Davidson, Hae Jin Jeong, Chris D. Lowe, and David J. S. Montagnes. 2010. Feeding in the Dinoflagellate *Oxyrrhis marina*: Linking Behaviour with Mechanisms. *Journal of Plankton Research* 00 (0): 1–12.

Verity, P.G. 1985. Ammonia excretion rates of oceanic copepods and implications for estimates of primary production in the Sargasso Sea. *Biological Oceanography* 3(3): 249-283.

Wolfe, G.V. 2000. The chemical defense ecology of marine unicellular plankton: constraints, mechanisms, and impacts *Biol Bull 2000 198:225-244.*

Worden, Alexandra Z., Michael J. Follows, Stephen J. Giovanni, Susanne Wilken, Amy E. Zimmerman, and Patrick J. Keeling. 2015. Rethinking the Marine Carbon Cycle: Factoring in the Multifarious Lifestyles of Microbes. *Environmental Science* 347 (6223): 735–45.

Key Point:

- Ammonium excreted by copepods in swarm abundances negatively affects *O. marina* ingestion and growth

Key Index Words:

Oxyrrhis marina; chemosensory; ammonium; copepod excretion.